GROWTH, CHACTERIZATION AND THERMODYNAMIC MODELING OF
ABSORBER AND TRANSPARENT CONDUCTING OXIDES FOR COPPER
INDIUM DISELENIDE BASED THIN FILM SOLAR CELLS

By

LEI L. KERR

A DISSERTATION PRESENTED TO THE GRADUATE SCHOOL
OF THE UNIVERSITY OF FLORIDA IN PARTIAL FULFILLMENT
OF THE REQUIREMENTS FOR THE DEGREE OF
DOCTOR OF PHILOSOPHY

UNIVERSITY OF FLORIDA

2004

This dissertation is dedicated to my beloved husband, Mike Kerr, my parents, Youqun Li and Yin Chen, and my sister, Yi Li and my brother, Le Li.

TABLE OF CONTENTS

LIST OF TABLES

LIST OF FIGURES

GROWTH, CHARACTERIZATION AND THERMODYNAMIC MODELING OF
ABSORBER AND TRANSPARENT CONDUCTING OXIDES FOR COPPER
INDIUM DISELENIDE BASED THIN FILM SOLAR CELLS

By

Lei L. Kerr

May, 2004

Chair: Dr. Tim Anderson
Major Department: Chemical Engineering

The absorber and transparent conducting oxides (TCO) layers are the most

important in the CIS-based solar cell structure. This dissertation focuses on selected

process development and fundamental issues in these two layers.

In hope of identification of low temperature route to CIS, the Cu-In-Se phase

diagram was estimated using a sub-lattice model. The predicted Cu-In-Se phase diagram

suggested a low temperature (~ 210 °C) liquid+α-CuInSe$_2$ two phase region. An

alternative route to CuInSe$_2$ formation that uses this low melting liquid to obtain grain

growth was demonstrated using RTP on the stacked precursor structure Cu-Se/In-

Se/Mo/glass. The influence of various ambient compositions on phase transformations

after rapid thermal processing was determined. A 5.08% efficiency device with V_{oc}=

0.296 V, J_{sc} = 34.65 mA/cm^2 and fill factor = 49.54% was produced by using the

absorber that is obtained by RTP on the CuSe/InSe/Mo/Glass precursor under Se control

in a PVD system. The correlation between the defects in the absorber to the device

performance was analyzed by Deep-Level Transient Spectroscopy (DLTS). A midgap defect level attributed to Cu_{In} was identified and is believed to contribute to the low V_{oc} and fill factor.

For solar cell applications, it is desirable for the TCOs to have both high electrical conductivity and transparency. These two properties vary oppositely with F content. A method for estimating the solubility of F in all the binary oxides was developed and applied to fluorine-doped tin oxide (FTO) as a function of temperature and of the partial pressure of dopant precursor.

Sputter deposition and characterization of ZnO thin films for application as a transparent conducting electrode have been studied. The effects of processing conditions on film properties, evolution of structural and electrical properties, and the influence of ion damage on the thin film properties were investigated. A base pressure $2{\sim}3{\times}10^{-7}$ Torr, $5{\sim}6$ mTorr gas pressure and $200{\sim}300$ W were found to be the appropriate conditions for R.F. diode sputtering of ZnO:Al films. The lowest resistivity obtained was $2.7{\times}10^{-3}$ $\Omega{\cdot}cm$ with a transmittance above 85% and bandgap E_g about 3.35 eV at RF power 250 W, 5 mTorr Ar pressure, and $3{\times}10^{-7}$ Torr base pressure.

CHAPTER 1
INTRODUCTION

1.1 Device Physics – How does a Solar Cell Work

Solar cells can absorb electromagnetic waves and convert the absorbed photon energy into electrical energy. It mainly consists of a diode. Figure 1-1 shows a simple p-n junction of a solar cell. When the energy of the incident photon is larger than the band gap, the photon can be absorbed by the semiconductor to create an electron-hole pair. The electrons and holes are then driven by the electric field in the diode to produce a photocurrent (light-generated current). Contreras *et al.* [1] observed that photovoltaic action (electric field) in a solar cell comes from (1) built-in electrostatic field as in the case of a p-n junction, (2) from effective force fields due to variations in semiconductor properties (3) from variations in excess carrier distributions (Dember effect).

The basic phenomena occurring in a p/n homojunction solar cell [2-3] are described next (1) The metal contact to the p-type semiconductor introduces a contact resistance which is determined by the work functions of the metals used for contacts, the electron affinity and carrier density of the contacted semiconductor, and the possible effects of interface states at the metal/semiconductor junction; (2) The light in the bulk p-type region is absorbed to generate electron/hole pairs. Most of the pairs are generated inside the space charge region and separated by the junction electrical filed. The few pairs that generated outside space charge region will diffuse into space charge region and then be separated by the junction electrical field. Since it is a p type semiconductor, $\Delta p \ll p_0$ and the device performance is determined by the minority carrier (electron) behavior in the p-

type material. The minority electrons are partially lost by recombination and the action of holes is drift; (3) The bulk of the n-type region contributes mainly to a series resistance. (4) The contact of the p-type to n-type semiconductor will not only introduce a contact resistance but also introduce surface recombination loss of minority carriers.

The generation rate for electron/hole pairs in the bulk region is determined by the illumination flux and the optical absorption constant of the semiconductor. The diffusion transport process is controlled by the mobility of the photogenerated minority electrons in the p-type region. The recombination loss can be described in terms of a lifetime for bulk recombination, as well as by a surface recombination velocity for recombination of carriers generated near the interface of the device.

The optimal bandgap E_g for absorber is around 1.4~1.5 eV. This is an optimum value obtained by compromising two opposite effects induced by bandgap [2], that is, increasing E_g will decrease reversed bias saturated current and in turn increase the voltage obtainable from the cell. However, increasing E_g will also decrease the photocurrent because less solar spectrum is absorbed. Fig. 1-2 shows a typical solar spectrum. The absorption coefficient for the absorber is desired to be as high as possible, and this will require less film thickness.

1.2 Solar Cell Structure

Thin film polycrystalline compound semiconductors are of considerable interest because of their potential lower manufacturability cost as compared to traditional crystalline silicon (200 μm thickness due to its indirect bandgap 1.1 eV) or polycrystalline silicon materials. The advantages of thin film technologies are: lower consumption of direct and indirect bandgap materials; independence from shortages of

silicon supplies; fewer processing steps and more suitable for automation; monolithic circuit design and no assembly of individual solar cells into final products [4]. There are three materials of contemporary interest for thin film polycrystalline solar cells; copper indium gallium diselenide, $Cu(In_xGa_{1-x})Se_2$ (CIGS), cadmium telluride (CdTe), and a-Si.

The configuration of solar cell can be divided into superstrate and substrate structure solar cell depending on the layer deposition sequence. Usually, the layer requiring high process temperature will be deposited earlier than that requiring low temperature. The practical meaning of the substrate solar cell is that the TCO is deposited after all of the layers have been deposited. The superstrate solar cell is that the TCO is deposited to the glass substrate before the absorber layer and serves as the top electrode.

1.2.1 Substrate Solar Cell – CIGS Solar Cell

CIGS material based solar cell is a typical substrate solar cell structure as shown in Figure 1-3. It consists of substrate, back contact, absorber, buffer layer, window layer and antireflection coating. An inverted layer is proposed to exist at the front surface of CIGS absorber [5], thus producing the electrical potential in a positive different than the metallurgical one.

Substrate

Soda-lime glass (SLG), Mo foils, Ni foils, stainless steel and polymer all can serve as the base substrate for solar cells. For terrestrial applications, SLG has yielded the best results from a device performance point of view [1]. The reasons could be its better thermal expansion coefficient match with CIGS absorber and the positive effect of sodium. The out diffused Na ions is believed to increase the electrical conductivity and to reduce the grain boundary energy barrier by forming either Na_{In} defects or removing

midgap states [6-7] (reduce recombination). However, Na_2Se is believed to cause a poor adhesion of CIS to Mo back contact [3]. The most significant problem with SLG is its inability to withstand high processing temperatures (> 550 °C).

In terms of lightweight flexible substrate for space application, Mo foil is the best choice. The ITN energy system Inc. works on the solar cells on polymer substrate.

Back Contact

Molybdenum (Mo) is currently used as a back contact for CIS on SLG substrates and is deposited by sputtering. The deposition condition affects the film adhesion and sheet resistivity greatly. A layer of $MoSe_2$ is believed to exist between CIGS and Mo. It has a bandgap energy of 1.4 eV and creates a back surface field to enhance the carrier collection. It can also improve the adhesion of CIGS film to Mo contact and form good ohmic contacts [3].

It is also noted that there has been research conducted on using SnO_2 as the back contact for CIS [7].

Absorber

High absorption coefficient and direct bandgap makes $CuInSe_2$ an attractive candidate for thin film polycrystalline photovoltaic material. As mentioned earlier, the electric force field is needed to separate and drive electrons and holes to form a photocurrent. Variations in semiconductor properties can induce an effective force field by tailoring the bandgap with the absorber, which can be achieved by compositional variations. The compositional variations will eventually change the conduction band minimum (CBM) or the valence band maximum (VBM) or both.

In the mixed-cation Cu(In,Ga)Se$_2$ thin-film absorber materials, the bandgap variation mostly occurs in the CBM by adding Ga into CuInSe$_2$. Gabor *et al.* [8] did detailed analysis of this graded solar cell structure. According to their work, the quasielectric field of graded band gap structures provides an additional drift force that aids in the collection of carriers generated outside the depletion region and prevents their recombination at the back interface, while most ungraded solar cell structures depend on diffusion to collect carriers generated outside the depletion region and only these carriers with longer diffusion length can be collected outside the depletion region. The incorporation of gallium in CuInSe$_2$ has also led to the better adhesion of the film to the Mo back contact. The bandgap of the resultant film was found to be between 1.0 and 1.6 eV (the bandgap of CuGaSe$_2$), and it can be tuned to better match the solar spectrum. The bandgap is linearly related to the amount of gallium in the film.

Another way to modify the bandgap of CuInSe$_2$ to better suit the solar spectrum is adding S to anion site. CuInS$_2$ has a bandgap of about 1.55 eV that closely match the visible part of the solar spectrum, and it has high absorption coefficient (10^5 cm^{-1}) and a lower toxicity.

Buffer Layer

CdS with bandgap energy of 2.4 eV is considered a good n-type heterojunction partner to CIS. It is usually prepared by chemical bath deposition (CBD) at a temperature as low as 65°C. A new O$_2$-alloyed CdS layer whose bandgap varies with the O$_2$ content has been developed at the National Renewable Energy Lab (NREL) [9]. CdS will convert the absorber surface region from p-type to n-type by Cd ions substitution on Cu sites to provide excess electrons [3]. It also smoothes CIGS surface and lower the surface

recombination velocity. Furthermore, it protects the CIGS surface from ion bombardment in the subsequent sputtering deposition of the window layer.

The use of the wider band gap heterojunction partner will enhance both the open-circuit voltage and photo-current of the device and achieve higher conversion efficiency. Adding Zn to CdS will increase the bandgap of CdS by substituting Zn onto the Cd lattice. Especially in $CuGaSe_2$ based solar cell, the use of $Zn_xCd_{1-x}S$ instead of CdS can lead to an increase in photocurrent by providing a match in the electron affinities of the two materials. It is also a potential window layer material for the fabrication of p-n junctions without lattice mismatch for CIGS solar cells.

Due to the toxicity of Cd, alternative buffer layers such as ZnS, $Zn(O,S,OH)_x$, ZnO, ZnSe, $In_x(OH,S,)_y$, In_2S_3, $In(OH)_3$, SnO_2, $Sn(S,O)_2$, ZnSe and ZrO_2 are under investigation.

Inverted Layer

It is proposed that an inverted layer (n-type) is created after the buffer layer deposition. It has a bandgap of 1.3 eV. It is suggested that the composition of this inverted layer is a n-type ordered vacancy compound (OVC) such as $CuIn_3Se_5$ [10]. The buried homojunction is thus formed.

Window Layer

ZnO:Al is the current material used as a window layer for CIGS material based solar cells. It has an electrical resistivity as low as 2×10^{-4} $\Omega\cdot cm$ with carrier concentration 10^{18} cm^{-3} and over 85% optical transmittance in the visible spectrum. The undoped ZnO is used as an intrinsic buffer layer and enhance the uniformity of electrical properties. CIGS is a substrate solar cell that typically uses soda lime glass as the substrate. The

sodium can rapidly diffuse into the TCO at high temperature and decrease its conductivity. Thus a low deposition temperature window layer is required for CIGS solar cells. Both ZnO:Al and ZnO are commonly deposited by RF sputtering deposition where normal room temperature deposition is used. Therefore, ZnO:Al is very much preferred in the $CuIn_xGa_{1-x}Se_2$ based substrate structure solar cell where the low temperature deposition for TCO is required.

<u>Metallization</u>

Approximately 3 μm of Al and 500 Å of Ni bilayer are deposited by electron beam evaporation as the front contact for CIS. The Ni layer is added to prevent the reaction between Al and ZnO. Also, Al is a soft material and Ni layer can prevent the probe from penetrating into ZnO layer while taking the electrical measurements.

CIGS based solar cell has achieved 12.8% large area module (3625.9 cm^2) and 19.2% in the lab scale cell by the NREL.

1.2.2 Superstrate Solar Cell – CdTe and a-Si Solar Cell

CdTe and a-Si are superstrate cells as shown schematically in Figures 1-4 [11] and 1-5 [12]. CdTe has a direct optical gap energy of 1.45 eV which makes itself an attractive material for thin film solar cells. Currently, the world record has been built by NREL with a cell efficiency of 15.5% prepared by close spaced vapor transport. The challenges in the CdTe technology are (1) the currently used contacts for CdTe are not stable and are sensitive to moisture and air. (2) Cd is very toxic. CdTe cell uses SnO_2:F as a back contact and Cu paste as the front contact.

Amorphous silicon is the most developed thin film technology for solar cells. The cell structure has a sequence of p-i-n layers. It is a single junction, and its junction degrades about 30% over time which is a significant problem for a-Si technology.

The small scale laboratory devices to date for CdTe and a-Si cells are 16.5% and 13% (stabilized), and the commercial modules are 11% and 7%, respectively.

1.3 Statement of Work

The CuInSe$_2$ material based solar cell has shown continuous improvement in cell efficiency and stability compared to other thin film candidates as shown in Figure 1-6 due to its remarkable film properties [13] as reviewed in Chapter 2. However, CdTe solar cell has experienced more rapid commercialization than α-CuInSe$_2$ due to its simpler deposition. Hence, it is important to reduce the manufacturing cost of α-CuInSe$_2$ through the development of straight forward alternate means of depositing the device-quality CIS and its alloy films. In this work, low-cost approaches to low temperature deposition of absorber are explored. In particular the use of by rapid thermal processing on novel binary bilayer CIS precursor is investigated. This work will be presented in Chapter 3. The correlation between deposition conditions and film properties was investigated, and the phase diagram was used to help analyze the reaction pathways. Devices were fabricated and their performance characterized by current-voltage (I-V) measurements.

CIS has a large homogeneity range, and such a deviation from stoichiometry in compound semiconductors is often attributed to antisite defects, vacancies, and defect clusters in the material. These defects have considerable control in the chemistry of CIS and introduce degrees of freedom to the CIS properties. Deep Level Transient Spectroscopy (DLTS) and Capacitance-Voltage (C-V) measurements are employed to

study deep-level electron and hole traps in CIGS solar cells fabricated at three different locations (EPV, NREL, and UF). The activation energy and trap density as well as suggested defect origins are given. The detailed experimental procedure as well as results are given in Chapter 4.

To understand the processing mechanisms, reaction pathway and defect chemistry that are involved in the complexity of CIS, an equilibrium defect model of the Cu-In-Se system at 500°C, which is the temperature of technical importance for the fabrication of CIS thin films, is developed to understand the defect chemistry of Cu-In-Se system. This is described in Chapter 5.

Chapter 6 gives a material property review on transparent conductive oxides (TCO) for photovoltaic application. Unfortunately, the TCO properties have not been improved significantly for many years. For solar cell applications it is desirable for the TCO to have both high electrical conductivity and high transparency. These two properties, however, vary oppositely with dopant content. It is believed that different dopant-host schemes will be required. Thus a method to estimate dopant solubility will be useful to suggest material candidates . A thermodynamic modeling is developed to study the F doping solubility in SnO_2 as described in Chapter 7.

ZnO has several advantages for use as a TCO $CuInSe_2$ material based photovoltaic devices as compared to other oxides, RF sputtering has proven to be a good technique for the deposition of ZnO. This study focuses on determination of the most suitable deposition conditions to obtain ZnO:Al thin films with a low resistivity and high transmittance and to obtain thin uniform films. The results of the study are presented in Chapter 8.

In a word, this dissertation will focus on experimental and theoretical aspects of physical and chemical properties of the window layer (Metal Oxides) and absorber (CIS) for CIS substrate solar cell. The organization of the dissertation is as follows:

Chapters 2 to 5 focus on the absorber layer. Chapter 2 is the literature review of the absorber. Chapter 3 describes the rapid thermal processing of CIS precursors, while Chapter 4 presents the defect study in absorber b DLTS. Chapter 5 presents the thermodynamic model of the Cu-In-Se system. Chapters 6 to 8 are dedicated to work on the window layer material. Chapter 6 reviews the literature of all the TCO materials. Chapter 7 gives the results on F doping in SnO_2, while chapter 8 presents results on the sputter deposition of ZnO:Al. Finally, chapter 9 describes the conclusions and recommendations for future work.
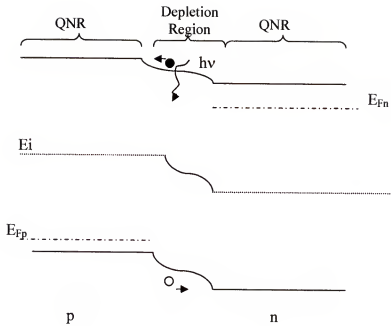
Figure 1-1. A homojunction of a solar cell [2]. QNR: Quasi-neutral region; Ei: Intrinsic Fermi level; EFp: Fermi level of p-type material; EFn: Fermi level of n-type material.
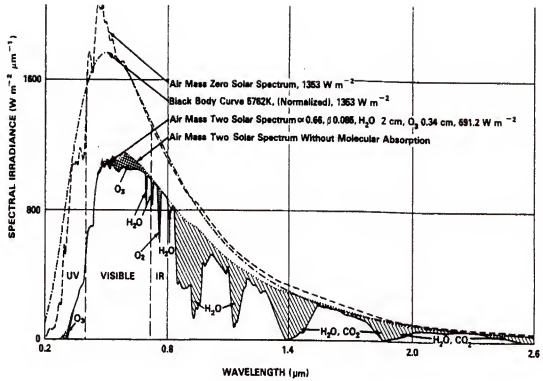
Figure 1-2. Solar spectrum [2].
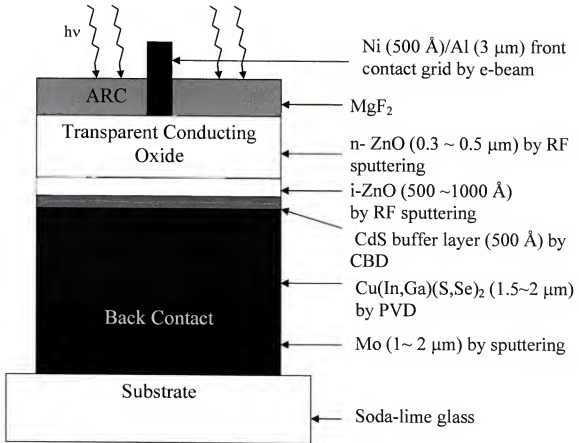
Figure 1-3. Typical CIGS substrate solar cell structure.
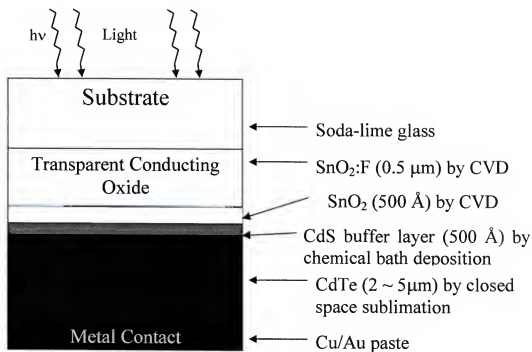
Figure 1-4. Typical CdTe superstrate solar cell structure [11].
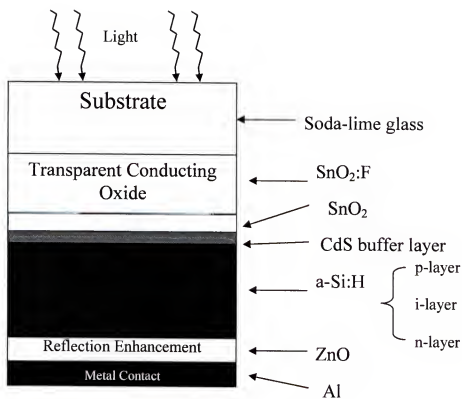
Figure 1-5. Typical amorphous silicon superstrate solar cell structure [12].
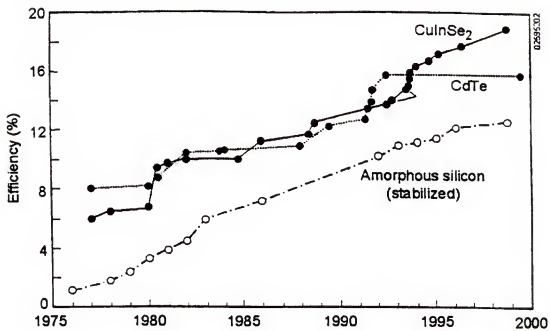
Figure 1-6. Comparison of laboratory cell efficiencies trend for thin film cells over the period 1975-2000 [13].

CHAPTER 2
LITERATURE REVIEW OF CIS MATERIAL

Chalcopyrite $CuInSe_2$ has a large absorption coefficient of $\alpha \sim 10^5$ cm^{-1} near the direct bandgap of $E_g = 1.04$ eV, which makes $CuInSe_2$ and its alloy a good candidate for thin film solar cell technology. The properties of this chalcopyrite semiconductor are strongly dependent on the defects in the crystal, and such a material has several degrees of freedom that can make the process potentially inexpensive and reproducible, though more difficult to understand.

2.1 Literature Review of CIS or CIGS Deposition Processes

Physical vapor deposition (PVD) and selenization of the deposited metals are the two principal methods in preparing CIS absorber layer for high-efficiency devices. PVD needs precise control of the flux of each element and requires a high temperature substrate and source. The selenization method of metal precursors essentially has two steps. The first step is to deposit selenium free precursor by vacuum or non-vacuum process. Researchers use either a Cu/In/Cu or In/Cu/In arrangement. Then it goes to the second step, selenization of the precursor. However, researchers realize that the problem associated with selenization of this selenium free precursor is the poor adhesion of the film to substrate. This is due to a three-fold volume expansion caused by the incorporation of selenium to the copper indium alloys. Also, indium loss due to its high vapor pressure is another problem of this process. So, selenium is added to the precursor as shown in Figure 2-1. Thus the first step is no longer a selenium free precursor. This precursor sequence is called a "stacked elemental layer structure". However, after

17

selenization of this stacked elemental layer, researchers have encountered problems of selenium dewetting (the amorphous Se layer that cause a laterally inhomogeneous nucleation and poor adhesion between CIS and Mo back contact) and the formation of high melting temperature second phase like Cu_2Se and In_2Se_3. The whole process involves a number of reactions and complex interdiffusion of intermediate phases, which will affect the controllability of the film quality.

To solve the problem, H_2Se is used. This is the commercialized selenization process that is employed by Shell Solar, the world's largest CIS module producer, as shown in Figure 2-2 [14]. H_2Se, however, is very toxic and unfriendly to the environment, and the selenization rate is slow. Selenization is usually performed at substrate temperature above 600 ˚C. The film composition inhomogeneity is the main drawback of this selenization method. Other methods, such as electrodeposition, sputtering, spray deposition, direct evaporation, and screen printing, are considered as less successful [15] due to their complex growth process.

To compromise the problems associated with the PVD and selenization methods, several processes related to direct PVD have been invented such as the most successful NREL three stage process [16]. A solar cell 19.2 % total area efficiency based on $Cu(In,Ga)Se_2$ thin film material is reported by NREL via its three stage process shown in Figure 2-3 [16]. In the first stage, the precursor $(In,Ga)_2Se_3$ layer is formed by the co-evaporation of In, Ga and Se from elemental sources at a substrate temperature about 260 ˚C. In the second stage, the Cu and Se are co-evaporated to bring the overall composition to near Cu-rich regime (Cu/(In+Ga) ~ 0.97 – 1.08) at 560 ˚C. Between the second stage and the third stage, the substrate is under the Se flux while ramping up the

temperature. During the third stage, In, Ga and Se are added with the amount of one ninth of the first stage to bring the overall composition back to Cu-poor at the same substrate temperature as the second stage. Then, the film is cooled to 350 ˚C under Se flux for 20 min.

2.2 Literature Review of Defect Chemistry of α, β_H, β_R, and γ-CIS Compounds

Defect can be divided into *dynamic defects* (phonons, electrons, and holes) and stationary defects. The *stationary defects* consist of point defects (e.g. vacancies, interstitials, antisite defects, and foreign impurities), defect complexes, line defects (e.g. dislocations), and surface defects (e.g. grain boundaries) [17]. Line defects and surface defects are also called structural defects. The large off-stoichiometry of $CuInSe_2$ is due to the high concentration of native point defects.

2.2.1 Defect Identification in the Cu-In-Se System

The electrical and optical properties of this ternary chalcopyrite compound are greatly affected by these intrinsic defects. The possible type of defects can be large so it is important to identify the dominant defects to simplify the modeling and its relation to understanding the defect which affects in material properties and the influence of process conditions.

Point Defects

Zahn *et al.* [18] used X-ray powder diffraction to directly characterize an In-rich α-$CuInSe_2$ sample with the results suggesting there are up to 8 at.% V_{Cu}, 5 at.% In_{Cu}, and 5 at.% V_{In}. The Cu_{In} and In_{Cu} antisite defects were believed to be in highly favorable in the near stoichiometric sample with composition Cu 25.08 mol%, In 25.55 mol% and Se 49.37 mole% by studying electron diffraction pattern of TEM, and a change of composition to Cu 26 mol%, In 21 mol% and Se 53 mol% will introduce vacancies on

the Cu or In lattice sites [19]. Both Dagan *et al.* [20] and Nadazddy [21] suggested that Cu vacancies are responsible for the electric field-induced Cu ion migration. Defect identification carried by Niki *et al.* [22] indicates that V_{Se} is another native defect in CuInSe$_2$.

V_{Cu} and V_{In} defects are identified by positron lifetime spectroscopy [24-25]. The positron annihilation spectroscopy is a method which allows one to study vacancy-like defects in solids. Positrons can be trapped in the open volume of the vacancy defects which increases their lifetime. Since the trapping rate is sensitive to the charge states of a vacancy in semiconductor, lifetime can yield valuable information on the type of vacancies. The slow positron beam characterization of intrinsic defects in MBE grown CuInSe$_2$ films showed that the divacancy defect V_{CuSe} is in the very In-rich sample and Monovacancy defect V_{Cu} exists in slightly In-rich sample [23].

Another in-depth study on the defect chemistry of CuInSe$_2$ by experimental measurement and theoretical calculation of positron lifetime spectroscopy was carried out by Polity *et al.* [24]. A series of peaks and bends observed in extrinsic photo-response spectra of CIS [26] are responsible for the photo-activation of point defect levels in CIS. According to their analysis, the V_{In} is hardly probable due to its large In atom weight and covalent size in the CIS crystal lattice. Point Defects such as $V_{Cu}(Cu_{In})$ and In_{Cu} should be generated simultaneously.

Schroeder [27] believes that both the electrically active defects and their neutral defects are responsible for the Cu/In ratio deviation from stoichiometry. The amount of antisite defects Cu_{Se} and Se_{Cu} are small due to their extremely high formation energy [28].

Charged defects are created when the neutral defects donate or accept an electron. The most characteristic point defects in the CIS crystals are the donor V_{Se} and the compensating acceptor V_{Cu}, and also the anitsite defects such as In_{Cu} and Cu_{In} [26]. Furthermore, the donor should be in its charge state V_{Se}^{+2} in all crystals with the deviation from ideal stoichiometry [27]. The acceptor and donor concentrations are below 10^{21} cm^3. The electrically active defects are In_{Cu}^{2+}, V_{Cu}^-, V_{Se}^{+2} [27].

Based on the review above, V_{Cu}, In_{Cu}, Cu_{In}, and V_{Se} are considered the four main neutral point atomic defects in α-CuInSe$_2$ crystal, and In_{Cu}^{2+}, V_{Cu}^-, V_{Se}^{+2} are the most abundant charged atomic defects.

Defect Complexes and β_H (Cu$_2$In$_4$Se$_7$), β_R(Cu$_1$In$_3$Se$_5$), and γ(Cu$_1$In$_5$Se$_8$) - CIS Compounds

Defect complexes are aggregates of point defects which can form during crystal growth and processing or after a crystal has been irradiated with energetic particles or X-rays [29]. The attractions between these point defects are sufficiently strong (e.g. one-tenth of an eV upwards) that pairs or larger clusters form and remain together for times long enough for their specific properties. For example, an In on Cu site defect binds a neighboring vacancy to it sufficiently strong that its lifetime as a pair is not only very many lattice vibrational periods but also many jumps of the vacancy around the impurity from one neighboring to another [30]. Defect complexes often play a significant role in determining the characteristics and performance of devices by affecting carrier lifetimes, degradation, breakdown, etc. Most defect complexes generally introduce strong perturbing potentials. As a result, they induce highly localized states, some of which may lie deep in the band gap [29].

The neutral defect complex $(In_{Cu}^{2+} + 2V_{Cu}^-)^0$ is believed to be the majority defect pair in Indium-rich CIS compounds (β_H, β_R, γ-CIS) [31-32]. Hall-effect and PL measurements on CIS single crystal show that V_{Cu} and V_{Se} are the dominate defects in CIS sample, and after annealing in In, the In_{Cu} defect is formed by the reaction: [33]

$$V_{Cu} + In \rightarrow In_{Cu}$$
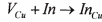
The defects $V_{Cu}^0, V_{Cu}^{-1}, (V_{Cu}^{-1} + In_{Cu}^{+2})^{+1}, (2V_{Cu}^{-1} + In_{Cu}^{+2})^0$ and Cu_{In}^0 are the dominant lattice defects in CIS suggested by Stanbery's equilibrium defect concentration calculation [28]. The defect distribution of CuInSe$_2$ as a function of the stoichiometry is simulated by a numerical method. The results indicate that defects V_{Se}, V_{Cu}, Cu_{In} and $(2V_{Cu}^{-1} + In_{Cu}^{+2})^0$ are the dominate defects in CIS [24].

Zhang [31-32] has conducted first principle calculations on CIS defect physics and chemistry. His calculation results show that β_H, β_R, and γ-CIS compounds are formed by repeating periodically m units of $(2V_{Cu}^{-1} + In_{Cu}^{+2})^0$ for every n unit of α-CIS (CuInSe$_2$).
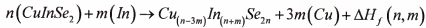
$$n(CuInSe_2) + m(In) \rightarrow Cu_{(n-3m)}In_{(n+m)}Se_{2n} + 3m(Cu) + \Delta H_f(n,m)$$

where (In) and (Cu) denotes In and Cu in their respective equilibrium chemical reservoirs. The energy $\Delta H_f(n,m)$ is close to zero [31] and for β_R-CIS (Cu$_1$In$_3$Se$_5$), n =5 m=1, for γ-CIS(Cu$_1$In$_5$Se$_8$), n=4 n=1, for β_H -CIS(Cu$_2$In$_4$Se$_7$), n=7 m=1

Based on the review above, the complex defect, $(2V_{Cu}^{-1} + In_{Cu}^{+2})^0$ is the cause of existence of β_H, β_R, γ-CIS.

A summary of the dominant defects in CIS are listed in Table 2-1.

2.2.2 Defect Transition Energies

A theoretical study on the defect physics of α-CuInSe$_2$ has been conducted by

Zhang *et al.* [31-32] using first principle calculations. The calculation results are

compared to experimental results in Figure 2-4 [34]. The experimental techniques that

have been successfully used to identify the defect transition energy level in CuInSe$_2$ are

electrical measurement, photoluminescence, deep level transient spectroscopy (DLTS),

optical absorption and photoacoustic spectroscopy. The summary of these experimental

results are shown in Table 2-2 [35]. The transition energies of all the possible defects

that are identified in the previous section are listed in Table 2-3. As can see in this table,

the most shallow donor transition will be $V_{Se}^0 \rightarrow V_{Se}^{-2}$ and the most shallow acceptor

is $V_{Cu}^{-1} \rightarrow V_{Cu}^0$.

2.2.3 Gibbs Energy Data of Defects in α-CuInSe$_2$

Enthalpy

Three research groups [31,36-37] have done the detailed formation energy

(enthalpy) calculations for each defect in CuInSe$_2$. Zhang *et al.* [31] calculated

formation enthalpies in CuInSe$_2$ for cation defects and defect complexes. According to

their study, the formation energy $\Delta H_f \left(j, q = 0 \right)$ of a neutral ($q = 0$) defect type j in

CuInSe$_2$ depends on the chemical potential μ_i of each element in the defect.

$$\Delta H_f \left(j, q = 0 \right) = E(j, q = 0) - E(CuInSe_2) + n_{Cu}\mu_{Cu}^j + n_{In}\mu_{In}^j + n_{Se}\mu_{Se}^j$$

where $E(j, q=0)$ is the total energy of a supercell containing a neutral defect of type j,

$E(CuInSe_2)$ is the total energy for the same supercell in the absence of the defect. The n's

are the numbers of Cu, In and Se atoms that are transferred from the defect-free supercell

to the reservoirs in forming the defect cell. The ionization energy is very small compared to the formation energy of each defect.

There is a large discrepancy in the calculation results of formation energy (enthalpy) for V_{Cu} between Zhang's [31] and that of other authors [36-37]. The reason for his much lower value is that he considered the electronic potential and the chemical potential of the atomic species into consideration, and found the very stable defect pair $(2V_{Cu}^{-1} + In_{Cu}^{+2})^0$. So, upon forming a V_{Cu}, it is consumed to quickly for the defect complex $(2V_{Cu}^{-1} + In_{Cu}^{+2})^0$ and overall formation energy is lowered by the presence of In_{Cu} defect. Klais et al. [12] observed that V_{Cu} concentration is greatly affected by the formation energy value change in their numerical simulation, while the concentration for Cu_{In} is constant upon the variation of its formation energy [24]. This indicates that the adopted formation energy value for V_{Cu} must be carefully considered for the thermodynamic model. In this work, the result from Neumann [36] and Moller [37] for a complete isolated point defect is used in the model for the formation energy of V_{Cu} in α-CIS phase, and the formation energy value of V_{Cu} with the existence of In_{Cu} from Zhang et al. [31] is incorporated into the defect complex $(2V_{Cu}^{-1} + In_{Cu}^{+2})^0$, which is an important defect in $β_H$, $β_R$, and γ-CIS. The formation energy of the defect complex $(2V_{Cu}^{-1} + In_{Cu}^{+2})^0$ can range from -0.05 eV to 5.67 eV depending on the composition [31, 32].

Entropy

S. B. Stanbery [28] calculated the lattice entropy for the CIS phases by employing a cluster-based approach based on a 16-site cluster of four normally occupied tetrahedral. The species in his calculation are clusters of primitive chalcopyrite unit cells within

which lattice point defects or their associates are embedded. He calculated the configuration of excess entropies by using a mixing model incorporating Hagemark's nearest-neighbor site exclusion correction.

A summary of calculation results of enthalpy, entropy, and Gibbs energy of each defects in CuInSe$_2$ is listed in the Table 2-4.

2.3 Gibbs Energy Data of Pure Compounds α-CIS (CuInSe$_2$), β$_R$-CIS (Cu$_1$In$_3$Se$_5$), γ-CIS(Cu$_1$In$_5$Se$_8$), and β$_H$-CIS(Cu$_2$In$_4$Se$_7$)

The knowledge of phase diagram and thermochemistry of CIS along with its constituent binaries will provide helpful information on the processing conditions and development of new thin film and bulk production methods. For the thermodynamic assessment of phase diagram, the phase stability and Gibbs energy of compounds are essential. The most complete and recent study on the phase equilibria of Cu-In-Se was conducted by Gödecke *et al.* [38] using DTA, XRD, TEM and SEM measurements. Figure 2-5 shows the experimental isothermal section of the Cu-In-Se phase diagram at 500°C over the entire composition triangle. The isothermal section at 500°C is of major technical importance for the fabrication of thin films for photovoltaic devices because these films are often deposited at a temperature around 500°C. Four ternary CIS compounds CuInSe$_2$, Cu$_2$In$_4$Se$_7$, CuIn$_3$Se$_5$ and CuIn$_5$Se$_8$ exist in this isothermal section. The following compares the Gibbs energy data obtained by three different methods.

2.3.1 Evaluation Method I- Data from Literature

The formation enthalpy and entropy data of these four CIS compounds have been estimated by different authors and the values are summarized in the Table 2-5 by Ider [39]. The Gibbs energy of these four CIS compound can be estimated by using the approximate equality (neglects ΔC_p),

$$\Delta G_{f,T}^0 = \Delta H_{f,298}^0 - T\Delta S_{f,298}^0 \tag{2.1}$$

2.3.2 Evaluation Method II – Data from Reaction (2.2)

Gibbs energy data of β_R-CIS ($Cu_1In_3Se_5$), γ-CIS($Cu_1In_5Se_8$), and β_H-CIS($Cu_2In_4Se_7$) can also be estimated based on the idea that ordered defect compounds (ODC) are formed by repeating periodically m units of ($2V_{Cu} + In_{Cu}$) for every n unit of α-CIS ($CuInSe_2$) [4,5],
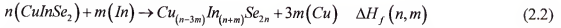
$$n\left(CuInSe_2\right) + m\left(In\right) \rightarrow Cu_{(n-3m)}In_{(n+m)}Se_{2n} + 3m\left(Cu\right) \quad \Delta H_f\left(n,m\right) \tag{2.2}$$

where (In) and (Cu) denotes In and Cu in their respective equilibrium chemical reservoirs. The energy $\Delta H_f(n,m)$ is assumed to be zero[31] and the values for n and m are:

n=2.5 m=0.5 for β_R-CIS ($Cu_1In_3Se_5$);

n=4 m=1 for γ-CIS($Cu_1In_5Se_8$);

n=3.5 m=0.5 for β_H –CIS ($Cu_2In_4Se_7$).

Therefore, the Gibbs energy data of β_R-CIS ($Cu_1In_3Se_5$), γ-CIS($Cu_1In_5Se_8$), and β_H-CIS($Cu_2In_4Se_7$) can be obtained from the following equations:

$$°G(\beta_R \text{ -CIS } (Cu_1In_3Se_5)) = 0.5 \times \Delta H_{f,2V_{Cu}+In_{Cu}}^0 + 2.5 \times °G(\alpha\text{-CIS } (CuInSe_2)) \tag{2.3 a}$$

$$°G(\gamma\text{-CIS}(Cu_1In_5Se_8)) = \Delta H_{f,2V_{Cu}+In_{Cu}}^0 + 4°G(\alpha\text{-CIS } (CuInSe_2)) \tag{2.3 b}$$

$$°G(\beta_H \text{-CIS}(Cu_2In_4Se_7)) = 0.5 \times \Delta H_{f,2V_{Cu}+In_{Cu}}^0 + 3.5 \times °G(\alpha\text{-CIS } (CuInSe_2)) \tag{2.3 c}$$

Where $\Delta H_{f,2V_{Cu}+In_{Cu}}^0$ is the formation energy for defect complex $(2V_{Cu} + In_{Cu})$, the entropy of $\Delta H_{f,2V_{Cu}+In_{Cu}}^0$ is negligible compared to enthalpy at the temperature of interest (773 K) according to the calculation results by Stanbery [26].

2.3.3 Evaluation Method III – Data from Pseudobinary Section In$_2$Se$_3$-Cu$_2$Se

From the isothermal diagram in Figure 2-5, it is clear that all the CIS compounds are in the tie line connecting compound γ-In$_2$Se$_3$ and β-Cu$_2$Se. Therefore, we can also estimate the CIS Gibbs energy relative to Gibbs energy γ-In$_2$Se$_3$ and β-Cu$_2$Se by the following simple relations:

$$\Delta G^0_{f,\alpha-CuInSe_2} = \frac{1}{2}\Delta G^0_{f,\gamma-In_2Se_3} + \frac{1}{2}\Delta G^0_{f,\beta-Cu_2Se} \qquad (2.4\text{ a})$$

$$\Delta G^0_{f,\beta_R-CuIn_3Se_5} = \frac{3}{2}\Delta G^0_{f,\gamma-In_2Se_3} + \frac{1}{2}\Delta G^0_{f,\beta-Cu_2Se} \qquad (2.4\text{ b})$$

$$\Delta G^0_{f,\gamma-CuIn_5Se_8} = \frac{5}{2}\Delta G^0_{f,\gamma-In_2Se_3} + \frac{1}{2}\Delta G^0_{f,\beta-Cu_2Se} \qquad (2.4\text{ c})$$

$$\Delta G^0_{f,\beta_H-Cu_2In_4Se_7} = 2\Delta G^0_{f,\gamma-In_2Se_3} + \Delta G^0_{f,\beta-Cu_2Se} \qquad (2.4\text{ d})$$

The Gibbs energies of α-CIS (CuInSe$_2$), β_R-CIS (Cu$_1$In$_3$Se$_5$), γ-CIS (Cu$_1$In$_5$Se$_8$), and β_H-CIS(Cu$_2$In$_4$Se$_7$) using the above different estimation methods are compared in Table 2-6.

Stacked Elemental Layer
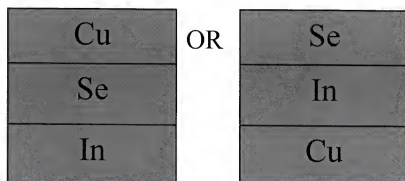
Figure 2-1. Schematic of the selenization of stacked elemental layer sequence for the absorber precursors.
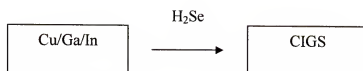
Figure 2-2. Shell Solar commercial selenization process [14] using H_2Se to selenize a metal stack precursors.
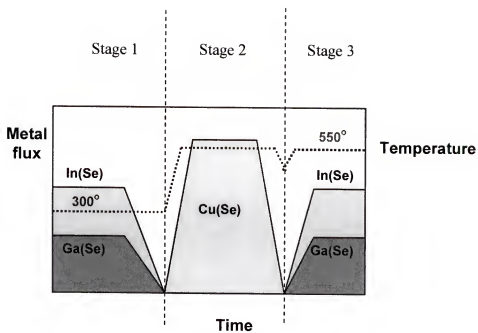
Figure 2-3. Schematic of the NREL three stage process [16].
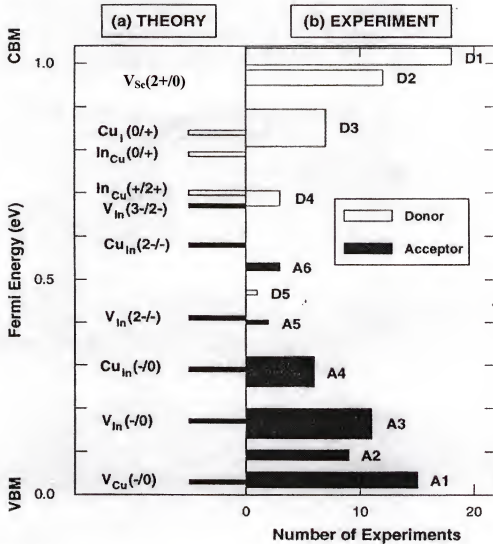
Figure 2-4. Comparison between calculated and experimental transition energy level diagram for common point defects in CIS [34].
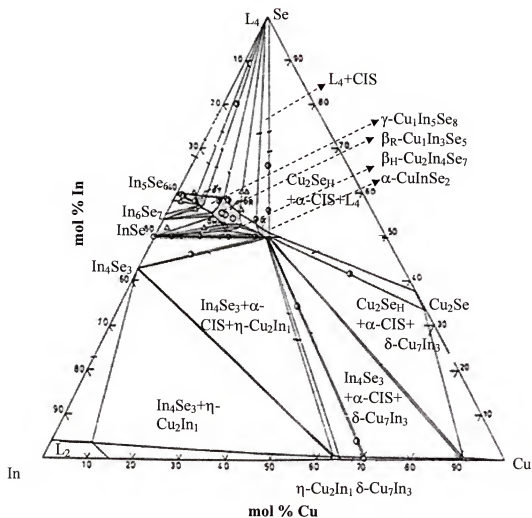
Figure 2-5. Isothermal composition phase diagram of the Cu-In-Se system at 500˚C [38].

Table 2-1. Predominate defect identification in CuInSe$_2$

Reference	Defect type determined	Calculation or Experimental Method
[18-21]	V_{Cu}^0	X-ray powder diffraction, Selected electron diffraction of TEM sample
[24],[27]	V_{Cu}^{-1}	Positron lifetime spectroscopy, Implication from Hall and composition measurement
[26]	In_{Cu}^0	Extrinsic Photoresponse
[24],[27]	In_{Cu}^{+2}	Positron lifetime spectroscopy, Implication from Hall and composition measurement
[18],[26]	Cu_{In}^0	X-ray powder , extrinsic photo-response
[26]	No V_{In}^0	Extrinsic photo-response
[23]	V_{In}^0	Positron lifetime spectroscopy
[22]	V_{Se}^0	Positron lifetime spectroscopy
[27]	V_{Se}^{+2}	Implication from Hall and composition measurement
[28]	$(Cu_{In}^{-1} + In_{Cu}^{+1})^0$	Theoretical calculation
[28], 31],[32]	$(2V_{Cu}^{-1} + In_{Cu}^{+2})^0$	Theoretical calculation

Table 2-2. Experimental defect transition energy levels in CIS [35].

Method	E_{D1}	E_{D2}	E_{D3}	E_{A1}	E_{A2}	E_{A3}	E_{A5}
Elect. (meV)				20-28			
Elect.				35	100		400
Opt. abs.			232	38		154	
PL				40			
PL					85		
PL	35	72			100	150	
PL		55		30	85	130	
PL		70		40	80		
PL		60		40	80		
PL	43			17		162	
DLTS				16-39	87-92	166-191	

Type	E_{A3}	E_{A4}	E_{A6}	*p*-type
p	200		540	
p		280,320		Deep levels by
?		250	520	DLTS
?	120-190	260-280		
p	186	250	520	
p		220-280		
p	166-191	276		

D: donors, A: acceptors, Elect.: electrical measurement,
Opt. abs.: optical absorption, PL: photoluminescence

Note: The symbol E_{A1}, E_{A2}, etc. uses the same notation as that in Figure 2-4.

Table 2-3. Summary of calculated and experimental defect transition energies in CIS.

Defect type	$\varepsilon_a(\,^{q}\!/_{q'})$ (eV)	Reference	Calculation or Experimental Method
$V_{Cu}^{-1} \rightarrow V_{Cu}^{0}$	E_v+0.03	[31]	First principle calculation
	E_v+0.045	[33]	Photoluminescence
	E_v+0.075	[40]	Photoluminescence
	E_v+0.093	[41]	Photoacoustic and photoluminescence technique (PPT)
	E_v+0.04	[42]	Cathodolumninescence
$In_{Cu}^{+1} \rightarrow In_{Cu}^{0}$	E_c-0.25	[31]	First principle calculation
$In_{Cu}^{+2} \rightarrow In_{Cu}^{0}$	E_c-0.34	[31]	First principle calculation
$Cu_{In}^{-1} \rightarrow Cu_{In}^{0}$	E_v+0.29	[31]	First principle calculation
	E_v+0.26	[21]	Deep level transient spectroscopy (DLTS)
$Cu_{In}^{-2} \rightarrow Cu_{In}^{0}$	E_v+0.58	[31]	First principle calculation
	E_v+0.49	[21]	Deep level transient Spectroscopy (DLTS)
$V_{In}^{-1} \rightarrow V_{In}^{0}$	E_v+0.17	[31]	First principle calculation
$V_{In}^{-2} \rightarrow V_{In}^{0}$	E_v+0.41	[31]	First principle calculation
$V_{In}^{-3} \rightarrow V_{In}^{0}$	E_v+0.67	[31]	First principle calculation
$V_{Se}^{0} \rightarrow V_{Se}^{-2}$	E_c-0.06	[33]	Photoluminescence
	E_c-0.01	[40]	Photoluminescence
	E_c-0.06	[42]	Cathodoluminescence

Table 2-4. Enthalpy, entropy and Gibbs energy of the main defects in α-CuInSe$_2$ relative to defect-free CuInSe$_2$.

Defect type	ΔH_f			ΔS_f	$\Delta G_f = \Delta H_f - T\Delta S_f$
	[32] kJ/mol	[36] kJ/mol	[38] kJ/mol	[28] J/mol·K	at 773 K kJ/mol
V_{Cu}^0	57.8	308.2	250.4	0	57.8
In_{Cu}^0	321.7	154.1	134.8	0	32.2
Cu_{In}^0	148.3	183.0	125.2	0	148.3
V_{Se}^0	288.9	250.4	269.7	20.6607	273.0
$(2V_{Cu}^{-1} + In_{Cu}^{+2})^0$	140.6			0	140.6

Table 2-5. Experimental enthalpy, entropy and Gibbs energy of α, β_R, β_H, and γ-CIS
compounds [39].

Solid Phase	$-\Delta H^{o}_{f,298}$ (kJ/mol)	Method	S^{o}_{298} (J/mol K)	Method
α-CuInSe$_2$	267.4	Mass Spectrometry	157.7	Pulsed Calorimetry
	260.2	Calculated		
	280.0	Calculated	158.2	Calculated
	204.0	Calculated		
	189.8	Calculated		
	202.9	EMF		
	204.4	Calculated		
β_H-Cu$_2$In$_4$Se$_7$	754.2	Calculated	520.0	Adiabatic Calorimetry
			513.0	Calculated
β_R-CuIn$_3$Se$_5$	472.9	Calculated	354.8	Calculated
	266.9	Optimized		
γ-CuIn$_5$Se$_8$	664.6	Calculated	551.5	Calculated

Table 2-6. Comparison of Gibbs energy data of α, β_R,β_H,γ-CIS at 773 K estimated by different methods.

Solid Phase	$G^o_{f,773}$(HSER) (kJ/mol)	Method	Reference
α-CuInSe$_2$	-355.3	Estimation from In$_2$Se$_3$-Cu$_2$Se	
	-342.5	Using Eqn. (2.1) and data in Table 2-5	[39]
β_H-Cu$_2$In$_4$Se$_7$	-1183.9	Using Eqn. (2.2) and data in Table 2-4	This work
	-1211.3	Estimation from In$_2$Se$_3$-Cu$_2$Se	
	-1206.7	Using Eqn. (2.1) and data in Table 2-5	[39]
β_R-CuIn$_3$Se$_5$	-840.7	Using Eqn. (2.2) and data in Table 2-4	This work
	-856.1	Estimation from In$_2$Se$_3$-Cu$_2$Se	
	-897.0	Using Eqn. (2.1) and data in Table 2-5	[39]
γ-CuIn$_5$Se$_8$	-1354.4	Using Eqn. (2.2) and data in Table 2-4	This work
	-1356.8	Estimation from In$_2$Se$_3$-Cu$_2$Se	
	-1272.4	Using Eqn. (2.1) and data in Table 2-5	[39]

CHAPTER 3
FORMATION OF α-CuInSe₂ BY RAPID THERMAL PROCESSING ON STACKED BINARY COMPOUND BILAYER

As discussed in Chapter 2, the two principal CIS absorber formation methods, PVD and selenization, both require high-temperature substrates and sources. The former needs precise control of the flux of each element. The temperature for the process is over 550 °C for the formation of CIS such as that used in the NREL three stage process. The latter involves a number of reactions and the complex interdiffusion of intermediate phases affecting the controllability of the film quality. Care must be taken to prevent the formation of high melting temperature phases, such as $Cu_{2-x}Se$ and In_2Se_3, which will hinder the formation of CIS. Researchers use H_2Se instead of selenium for selenization to solve the selenium dewetting problem and to avoid the formation of high melting temperature secondary phase. However, H_2Se is highly toxic, and the selenization rate is slow.

The purpose of this work is to demonstrate a low temperature route for the formation of CIS by rapid thermal processing (RTP) of binary bilayer precursors.

3.1 Background

The ultimate goals of the research and development efforts are to create low cost, reproducible process with good process control. To accomplish these goals, fundamentally sound decisions must be made regarding the basic process and equipment to be employed, and then the entire process must be understood and characterized in terms of device behavior as a function of processing conditions. Among all the

techniques, RTP is promising. Rapid implies high throughput as well as potentially lower thermal budget and safer process. The rapid heating feature can also give better control of the process kinetics. Most of all, a steeper temperature profile lowers substrate temperature. Lower thermal budget also give larger flexibility on the substrate selection.

The Cu-In-Se phase diagram suggests that alternative precursor structures can be used for the selenization method for the CIS absorber formation. A scheme of the proposed precursor structure is shown in Figure 3-1. It consists of a slightly Se-rich In-Se or Cu-Se binary layer deposited at a low temperature on a Mo-glass substrate, followed by the deposition of a Se-rich Cu-Se or InSe binary layer, respectively. The stacked metal-Se bilayer precursor structure (Cu-Se/In-Se/Mo/glass) was rapidly deposited at 200°C in a custom designed Migration Enhanced Epitaxy (MEE) system [43] that accommodated 8 2" by 2" substrates, and subsequently annealed using RTP.

This structure was suggested by an examination of the Cu-In-Se phase diagram for conditions that show α-CuInSe$_2$ in equilibrium with a liquid phase at low temperature. Precursor layer compositions were then selected on the likelihood of forming the liquid phase while avoiding high melting temperature compounds. Fig. 2-5 illustrates the isothermal composition diagram of Cu-In-Se system at 500 °C [38]. The α-CuInSe$_2$ phase is seen to lie on the tie line connecting the In$_2$Se$_3$ and Cu$_2$Se phases, and it shows a solid solution range of several atomic percent. A low-temperature single phase Se-rich liquid solution is located near the Se corner of the phase diagram. The triangle connecting the α-CuInSe$_2$ phase boundary to the Se corner represents the α-CuInSe$_2$ plus Se-rich liquid two-phase region and is the target for the overall film composition. Phase diagram calculations suggest that the Se-rich liquid phase can exist at a temperature as low as

211 °C [44]. They also suggest that the synthesized CIS will be Se-rich and excess Se can easily volatilize during annealing. Starting from binary metal-Se layers in contact promises to avoid certain reactions that yield high melting temperature compounds and to increase grain size through liquid phase assisted growth. The rapid thermal processing mitigates undesirable solid to solid transformations predicted at low temperatures.

Why do we choose Cu:Se and In:Se layers with composition of ~ 1:1? The compounds CuSe and InSe have much lower melting temperature than Cu_2Se and In_2Se_3 [44], and the liquid phase can be easily achieved by rapid thermal processing because the rapid heating can allow us to avoid the solid and solid transformation. So, the slightly Se-rich CuSe and InSe composition are the best pair for the formation of α-CIS. With the precursor structure of CuSe/InSe/Mo/Glass, the top CuSe can prevent the In and Se loss from the bottom InSe. The vice versa structure (InSe on top of CuSe) will provide more efficient use of liquid phase which is formed by CuSe phase and thus achieve large grain growth.

3.2 Experimental Apparatus

The system used for absorber layer growth on binary compound-based precursor is a 4100 HEATPULSE Rapid Thermal Processing system supplied by AG Associates [44]. The RTP system is located in a clean room at the Surge Area at the University of Florida. The system is a single-wafer, cassette-to-cassette rapid thermal processor, capable of processing in inert or corrosive ambient. Currently, only N_2 is being used in the system. The HEATPULSE 4100 system components include: Heating Chamber, Quartz Isolation Tube, System Controller, Robot, Gas Control Electronics, ULPA Filtration System, Cooling Water Manifold, and Temperature Measurement Instruments. The oven isolates

the wafer to be processed on a quartz wafer tray inside a quartz tube located inside the actual heating chamber. The quartz isolation tube has a small opening in the rear for the introduction of gas used in wafer processing. This is the purge inlet fitting. Gas is exhausted through a hole in the door flange. The 208V, 1200W tungsten halogen lamps are arranged in a bank of 10 above and 11 below the isolation tube. The lamps are connected at each end to the triac plate mounted directly above the oven. The tungsten halogen lamps are controlled by triacs. The triacs are protected by an over-temperature sensor.

The RTP system is controlled by software that is menu-driven. The computing and user-interface functions of the RTP system consist of a computer and a touch screen. The wafer-handling system is comprised of the robot, robot controller, and connections for communications signals and vacuum. The robot provides automated loading and unloading of samples. Software modifications had been made to slow the speed of the robot movements.

The gas box is mounted on the left side of the system, and it can be connected to the house exhaust system by the exhaust hood mounted on the top of the gas cabinet. The ULPA filter unit is located above the wafer handling area, and it provides a local clean environment for loading and unloading samples. The entire unit can be removed if filter replacement or other servicing is required. The cooling system contains oven chamber cooling, pyrometer cooling, tube cooling, and electronic assembly cooling. The heating chamber cooling system is connected to house chilled water at 65°F. The pyrometer cooling is provided by the internal closed loop chiller at about 15°C. The wafer temperature is monitored by either an optical pyrometer or a type K thermocouple. The

pyrometer or thermocouple sensing offers precise closed-loop temperature control. Currently, the wafer temperature is monitored by an optical pyrometer. The front view of the HEATPULSE 4100 RTP system is shown in Figure 3-2.

The HEATPULSE 4100 RTP system offers a great deal of flexibility in designing time/temperature profiles. Variable ramp rate, time, and temperature for each step in a cycle, and multi-step cycles that incorporate more than one steady state period can be programmed in the RTP system. The ramp rate can be as high as 250°C/sec. The programmable range for the steady state process time is 1~600 sec.

The short processing time and high ramp rate characteristics of this RTP can dramatically reduce volatilization losses during the reaction and provides liquid-phase assisted growth of the absorber layer. By carefully designing and choosing binary pairs for the precursor, the RTP can also help to avoid the high melting temperature phase formation. To understand the processing parameter effects on the reaction and crystallization kinetics, various temperature profiles were used by varying for example the temperature ramp rate, maximum temperature and soak time, and etc. Therefore, our objective is to utilize the processing advantages of RTP for the manufacture of CIS and CIGS solar cells while tailoring the precursor structure using the research PMEE reactor.

3.3 Film Characterization

The instruments used to study the film properties include XRD and SEM for structural characterization; EDS, AES, EPMA and ICP for composition analysis; I-V and QE for device performance measurements; and Deep Level Transient Spectroscopy for trap level and trap density study the results using this latter method will be presented in Chapter 4.

3.3.1 Crystal Structure Determination by X-ray Diffraction (XRD)

XRD is the most widely used technique for individual crystalline phase identification and its relative amount determination. An atomic plane (hkl) is spaced d_{hkl} apart in distance from one another. (hkl) are the Miller indices for an atomic plane. The XRD instrument used in this study is Philipe 3720. It uses X-ray wavelength of 1.54 Å Cu Kα source. When X-rays are scattered by the atomic plane in a crystal and the diffraction angle $2\theta_{hkl}$ satisfies the Bragg's law $\lambda=2d_{hkl}\sin\theta_{hkl}$, a diffraction peak can be observed. θ_{hkl} is the angle between the atomic planes and the incident (or diffracted) X-ray beam. The measured d-spacing in the diffraction pattern is compared with known standards in the JCPDS powder diffraction file to identify the present phases. If there are several phases in the films, the proportion of each phase can be determined from integrated intensities in the diffraction pattern.

3.3.2 Topographical Information – Scanning Electron Microscopy (SEM)

The SEM is a commonly used instrument for image analysis. A source electron beam is focused into a fine probe and rastered over the surface of the sample. With appropriate detectors, secondary electron and backscattered images can be obtained to provide the surface topographical information.

3.3.3 Local Composition Analysis - Energy Dispersive Spectroscopy (EDS)

When an ionized atom returns to its ground sate, it can release a characteristic X-ray. The concentrations of all the elements in the sample can be given by the analysis of the histogram of counts versus X-ray energy. EDS is always attached to electron column instruments like the SEM.

3.3.4 Composition Depth Profile - Auger Electron Spectroscope (AES)

The electron bombardment on the surface will produce an inner shell vacancy for the atom. Once the inner shell vacancy is created in an atom, the atom may then return toward its ground state via emission of a characteristic X-ray or through a radiationless Auger transition. The number of Auger electrons from a particular element emitted from a volume of material is proportional to the number of atoms of the element in the volume. Therefore, the relative ratio of elemental concentration can be determined from the energy distribution output of the detector. The Auger Spectroscope is combined with ion-beam sputtering to remove materials from the surface and to continue to monitor the composition and the chemistry of the remaining surface. By this means, the depth concentration profile is obtained.

3.3.5 Local Composition Analysis - Electron Probe X-ray Microanalysis (EPMA)

The physical basis of the EPMA is essentially the same as that of the EDS analysis. The only difference is the detector. The EDS uses the photoelectric absorption of the X-ray in a semiconductor crystal (silicon or germanium), with proportional conversion of the X-ray energy into charge through inelastic scattering of the photoelectron. The quantity of the charge is measured by a sophisticated electronic circuit linked with a computer-based multichannel analyzer to collect data. The EMPA detector is a focusing device and is based on the phenomenon of Bragg diffraction of X rays incident on a crystal. It has different crystals to detect a wide energy range. Therefore, The EPMA has higher peak-to-background ratio than EDS and can detect lower concentrations.

3.3.6 Overall Composition Analysis- Inductively Coupled Plasma (ICP)

In ICP, ions are generated in an inductively coupled plasma and subsequently analyzed in a mass spectrometer. The CIS film is dissolved by nitric acid prior to the analysis and is introduced to the plasma as a liquid.

3.3.7 I-V Measurements

A solar cell mainly consists of a diode, whose forward bias dark current-voltage relationship (i.e., I-V curve under no light illumination) can be expressed as

$$I = I_0 \left\{ \exp \left[q(V - IR_s) / AkT \right] - 1 \right\} \tag{3.1}$$

where I_0 is the reverse saturation current and is proportional to absorber bandgap by $\exp(-E_g / nkT)$, R_s is the sheet resistance, n is any integral number larger than 1 and A is the diode factor.

Under illumination,

$$I = I_0 \left\{ \exp \left[q(V - IR_s) / AkT \right] - 1 \right\} - I_L \tag{3.2}$$

where I_L is the light generated current. The optimal bandgap for the output of maximum efficiency is 1.4~1.5 eV. Increasing bandgap E_g will decrease I_0 and in turn increase the voltage obtainable from the cell. However, increasing E_g will also decrease the I_L because less solar spectrum is absorbed.

There are several important parameters other than light-generated current involved in a solar cell. Short-circuit current (I_{SC}) is the output current of the solar cell when the external circuit is shorted, i.e., zero load resistance. Open-circuit voltage (V_{OC}) is the output voltage of the solar cell when the external circuit is open, i.e., infinite load

resistance. The V_{oc} is also referred to as photovoltaic voltage. I_m and V_m are the current

and voltage for maximum power. The solar efficiency of the cell is defined as follows:

$$\eta = I_m V_m / P_{incident} \qquad (3.3)$$

$I_m V_m$ is related to V_{oc} and I_{sc} by the fill factor ff:

$$ff = I_m V_m / I_{sc} V_{oc} \qquad (3.4)$$

3.4 Experimental Results and Discussions

3.4.1 Susceptor Design

The design of the susceptor went through three stages due to problems encountered

at each stage as shown in Figure 3-3. Susceptor I (Figure 3-3 (a)) is designed to solve the

cracking problem when using a silicon wafer as the susceptor as evidenced by the optical

microscopy of CIS absorber plan view shown in Figure 3-4. Unfortunately, In and Se

losses occurred while using susceptor I according to Auger (Figure 3-7) and XRD (Figure

3-5) analysis. Thus, Suceptor II (Figure 3-3 (b)) was designed to solve this problem.

However, non-uniform heating occurred with the increased sample size. Therefore,

Susceptor III (Figure 3-3 (c)) has been designed to successfully solve this problem.

Susceptor I

The SLG sample with sample size 0.5" by 0.5" was initially placed on the top of a

piece of graphite wafer. After processing films with this design, the bottom of the

sodium-lime glass was observed to have exceeded the glass transition temperature. The

test samples were all cracked and adhered to the silicon wafer. Optical micrographs of the

samples were taken before and after the RTP and are shown in Figures 3-4. Therefore, a

4-inch diameter graphite plate as shown in Figure 3-4 was substituted for the silicon

wafer to increase the heat conductivity of the sample tray. Several RTP experiments were

conducted using graphite wafer. The plane view optical micrograph shown in Figure 3-4 (c) shows that the cracking and sticking are avoided by using the graphite tray.

Three samples with precursor structure CuSe/InSe/Mo/sodium-lime glass were processed. Samples were placed on a 0.5 mm thick piece of 4-inch diameter graphite with a N_2 purge flow originating from the back of the oven. The RTP annealing recipes for the 3 samples are summarized in Table 3-1.

Table 3-1 RTP conditions for processing CuSe/InSe/Mo/SLG sample

Sample	Soak time	Temperature	Ramp rate
1-1	70 s	550 °C	20 °C/s
1-2	70 s	750 °C	20 °C/s
1-3	140 s	550 °C	20 °C/s

The processed films were characterized by the XRD, Auger, and optical microscopy. From the XRD data shown in Figure 3-5, it can be seen that after RTP, the α-CuSe phase disappeared and the α-CuInSe$_2$ and Cu$_{2-x}$Se phases formed. The relative intensity of the peak around $2\theta = 26.560$ decreased when the soak time increased from 70 s (sample 1-1) to 140 s (sample1-3). This is attributed to the longer soak time increasing the In and Se losses and thus increasing the extent of formation of the Cu$_{2-x}$Se phase. It is likely that the In$_2$Se species is responsible since it has a high vapor pressure. There is little difference in the XRD spectra when the temperature is increased from 550 °C (sample 1-1) to 750 °C (sample 1-2) for the same soak time.

From the Auger data shown in Figure 3-7, In and Se loss is observed after RTP and as the temperature increases from 550 ℃ to 750 ℃, there are more loss of these two elements.

From the plane-view optical micrographs, as illustrated in Figures 3-6 (a)-(c), it can be seen that when the set temperature is at 750 °C (sample 1-2), the surface morphology of the processed film is much rougher than the one processed at 550 °C.

The above preliminary experimental results indicated that a high RTP temperature should be avoided and the loss of In and Se needs to be reduced. Therefore, a new sample holder was designed using a piece of flat quartz as a cover. This design is termed susceptor II.

Susceptor II and Influence of RTP Parameters Effect Study

A set of RTP experiments was performed on precursor samples (0.5" by 0.5") with CuSe/InSe/Mo/Glass structure to determine the effects of the RTP processing variables (temperature, soak time, delay times, sample size, and preheat intensity) on the composition change and phase transition of the film using susceptor design II as shown in Figure 3-3 (b). In this design, a quartz lid is used to cover the sample to minimize volatilization losses. A typical RTP cycle is shown in Figure 3-8.

Preheat Intensity Effect

Two kinds of preheat intensity were employed, 0% and 25%, for the same process condition 600 ℃, 60 s, 60 ℃/s Delay I 60 s, and Delay II time 200 s. The XRD and ICP results are shown in Figure 3-9. There is no significant change in film properties when increasing the preheat intensity to 25% except a slight increase in peak intensity at 26.5°. This increase is due to the increase extent of formation of $Cu_{2-x}Se$ because even though

$Cu_{2-x}Se$ peak overlaps with the CIS peak, $Cu_{2-x}Se$ usually has another peak at the shoulder of 112 peak position and the FWHM value for $Cu_{2-x}Se$ is less than that of CIS due to its higher crystallinity. The maximum preheat intensity for this RTP is 30%. Therefore, lower preheat intensity is preferred.

Steady State Temperature

For both soak times (Figure 3-10 and 11), when increasing the temperature there is more Se loss. The FWHM of the decreases of the 112 peak due to increase formation of $Cu_{2-x}Se$. Therefore, a lower soak temperature is preferred.

Ramp Rate (Figure 3-12)

When decreasing the ramp rate, the XRD pattern shows similar peak position, peak intensity and FWHM at 26.5°. There is a large decrease in Cu/In ratio when increasing the ramp rate while the Se composition remains the same. This means that a higher ramp rate will favor the formation of CIS and thus have more indium in the film. Therefore, a higher ramp rate is preferred.

Soak Time

At both a high temperature (Figure 3-13) and a low temperature (Figure 3-14), when decreasing the soak time, the FWHM decreases by 30%. This means that less CIS phase is formed in the film processed at a shorter soak time. There is no significant difference in composition when varying the soak time. Therefore, a longer soak time is preferred at both a high and a low temperature to form the CIS phase.

In conclusion, the film cracking and elemental loss issues were largely resolved by using a graphite sample tray and quartz cover even though slight loss of In and Se is still observed. From the XRD patterns measured for the films before and after the RTP, it can

be seen that both the α-CuInSe$_2$ and Cu$_{2-x}$Se phases are synthesized by the RTP from the binary bilayer precursors and the α-CuInSe$_2$ phase exhibited a chalcopyrite structure as indicated by the presence of the 101, 103, 211 and 105 reflections [45], [46]. The α-CuSe phase, which is the dominant phase in the precursor film, disappeared and reacted to form CuInSe$_2$ or Cu$_{2-x}$Se phases upon RTP. The narrow peaks indicate large crystal sizes. This suggests that the Cu-rich secondary phase is the competing phase in the binary bilayer process. However, it modifies the film morphology and results in large grain growth. From the XRD and ICP results, a higher ramp rate and a longer soak time have a significant positive influence on the α-CIS phase formation. A higher temperature will produce more loss in Se. Therefore, the starting RTP conditions for the following experiments on the precursor structure CuSe/InSe/Mo/Glass are: higher ramp rate, longer soak time, 0% preheat intensity, and lower steady temperature (around 500 °C).

Susceptor III

The RTP experiments were performed on new precursor series (growth run 230) with the structure CuSe/InSe/Mo/glass. For this sample set, the sample size was increased to 1" by 1" to allow cells to be fabricated. Experiments performed in the sample susceptor II (Figure 3-3 (b)) produced large lateral temperature gradients during RTP because of the relatively small size of the quartz cover. XRD spectra of the three different locations (see Figure 3-15) were taken, and the phase constitution of the three regions is shown in Figure 3-16. It can be seen that the Cu-Se secondary phase peak (2θ=21.3°) decreases in the center region as compared to the edge, consistent with a higher center temperature. The reaction in the center is thus more complete than at the edge. To improve heating uniformity, a new sample holder was designed (Figure 3-3

(c)). In this design, a recess is milled in a piece of graphite stock that holds the sample. A second recess is milled at a larger diameter to accommodate a flat quartz cover. This design used for the RTP experiments was made to minimize Se loss and to achieve a uniform temperature.

3.4.2 Phase Transition Study on CuSe/InSe/Mo/Glass Precursors

A phase transition study was conducted on the precursor structure CuSe/InSe/Mo/Glass using susceptor III to find a suitable reaction pathway for the formation of α-CIS.

Experimental

The stacked metal-Se bilayer precursor structure (Cu-Se/In-Se/Mo/glass) was rapidly deposited at 200°C in a custom-designed Migration Enhanced Epitaxy (MEE) system [43] that accommodated 8 2" by 2" substrates. A single precursor film was then annealed in a series of 4 steps in the RTP system. Each anneal step exposed the sample to a different ambient by coating the glass cover with either InSe or Se. The RTP experiments were performed on 1" by 1" samples from the same growth run. The whole investigation consists of five steps as follows:

Step I. Anneal using a clear quart cover

Initial experiments were conducted using a simple quartz cover with the gas ambient established by volatilization of the sample. The RTP conditions of a set-point temperature 480 °C, soak time 60 s, and ramp rate 60 °C/s were first tested. The XRD results, however, indicated incomplete formation of α-CuInSe$_2$, with intermediate phases (predominantly InSe, In$_6$Se$_7$, Cu$_{2-x}$Se and CuSe$_2$) remaining (see Fig. 3-17). Suspecting reaction limited processing, the set point temperature was raised to 600°C and the soak

time increased to 120 s. The XRD results shown in Fig. 3-18, however, do not show a significant change in the annealed film constitution. The overall composition of the annealed sample (temperature 480°C, soak time 60 s, and ramp rate 60 °C/s) was determined by the ICP analysis to be Cu 29.4%, In 23.6%, and Se 47.0 %. This composition is located in the three-phase region (liquid + $Cu_{2-x}Se$ + α-$CuInSe_2$) according to the isothermal section of the phase diagram shown in Fig. 2-5. These results suggest that Se volatilization occurred during processing. To maintain the Se concentration during annealing, Se was added to the system by depositing a thin layer of either InSe or Se on the bottom of the quartz cover.

Step II.   Anneal using a quartz cover with an InSe film

To modify the gas ambient, an1 μm film of InSe was deposited onto the quartz cover. The sample annealed in step I at RTP conditions 480 °C, 60 °C /s, and 60 s was again processed under the same conditions but with the InSe coated cover in place. As shown in the XRD pattern in Fig. 3-19, $Cu_{2-x}Se$ was still present.

Step III.   Anneal using a quartz cover with a Se film

To increase the Se overpressure, a thin layer of elemental Se was next deposited on the cover and the same sample was once more processed under identical RTP conditions (480 °C, 60 °C /s, 60 s). The XRD analysis showed an increase in the peak intensity at 2θ of 26.5˚ attributed to α-$CuInSe_2$, suggesting that InSe reacts with $Cu_{2-x}Se$ in the presence of Se (see Fig. 3-20). In addition small amounts of Se-rich $CuSe_2$ and In_6Se_7 were also apparent.

Step IV.   Anneal with a clear quartz cover

To reduce or eliminate the Se-rich $CuSe_2$ and In_6Se_7 phases, the same film was again annealed at the same conditions, but with no deposit on the underside of the cover plate. The results shown in Fig. 3-21 indicate that the final film is a single-phase α-$CuInSe_2$.

Discussion and Conclusion

XRD analysis of the precursor film (see Fig. 3-22) reveals only α-CuSe in the starting Cu-Se layer and no apparent crystalline phase in the In-Se layer. After the step I annealing, crystallization of InSe is evident, while secondary $Cu_{2-x}Se$ is formed, presumably in the top layer as a result of Se loss. The compound α-CuSe will decompose to $Cu_{2-x}Se$ with loss of Se at 377 ˚C [46] according to:

$$\alpha - CuSe(s) \rightarrow \tfrac{1}{2}\beta - Cu_{2-x}Se(s) + \tfrac{1}{4}Se_2 \qquad (3.5)$$
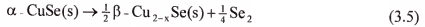
The constitution did not change significantly when the same sample was again annealed using an InSe coated slide. Apparently, there was insufficient mass transfer between layers to allow measurable reaction according to:

$$\beta - Cu_{2-x}Se(s) + InSe(s) \rightarrow \alpha - CuInSe_2(s) \qquad (3.6)$$
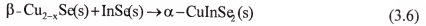
Although no significant reaction of β-$Cu_{2-x}Se(s)$ with InSe(s) occurred in steps I to III, the formation of α-$CuInSe_2$ proceeded rapidly in step IV. When a Se ambient is present during anneal, the following overall reaction occurs:

$$\beta - Cu_{2-x}Se(s) + 2InSe(s) + \tfrac{1}{2}Se_2(g) \rightarrow 2\alpha - CuInSe_2(s) \qquad (3.7)$$
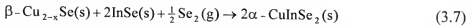
This reaction occurs rapidly with an activation energy of 25 kJ/mol as determined by a study of the selenization of Cu-In bilayers [47]. The apparent role of Se is to retain the CuSe phase by the reaction:

$$\beta - Cu_{2-x}Se(s) + Se_2(g) \rightarrow CuSe(s) \tag{3.8}$$
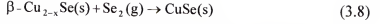
The SEM micrographs (see Fig. 3-23) support the above observations and the proposed reaction mechanism. The micrograph of the precursor structure (see Fig. 3-25(a)) clearly delineates the Cu-Se/In-Se/Mo layered structure. After the first anneal (step I), the three-layers are still evident, but the microstructure has changed (see Fig. 3-25(b)). According to the EDS analysis, the layer next to Mo layer is InSe, and the surface layer is β-$Cu_{2-x}Se$ while α-$CuInSe_2$ is formed between these two layers. Fig. 3-25(c) shows the final film structure after step IV. As desired, a single-phase α-$CuInSe_2$ is now present with a grain size on the order of a few microns.

Based on the above experimental observation, we conclude that Se control is an essential requirement for the RTP process of binary bilayer precursor, and a higher substrate temperature will be suggested to support the formation of a Se-rich liquid Cu_xSe phase in Cu-Se film to assist the growth.

$$\beta - Cu_{2-x}Se(s) \xrightarrow{\ Se\ } CuSe(s) \xrightarrow{\ High\ T\ } Cu_xSe(Liquid) \tag{3.9}$$
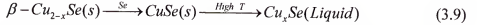
The liquid Cu_xSe can help the diffusion of In atom and thus the following reaction will happen:

$$Cu_xSe(Liquid) + InSe \rightarrow \alpha\text{-}CuInSe_2 \tag{3.10}$$
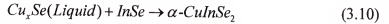
3.4.3 RTP Experiments on CuSe/InSe/Mo/Glass Precursors in PVD system

As discussed in the previous section, a Se ambient is needed for the formation of CIS, and a higher temperature is suggested to help the diffusion of In assisted by the formation of liquid Cu_xSe phase. Therefore, the following three runs were performed under Se over pressure of 5 Å/s control by RTP on CuSe/InSe/Mo/Glass binary bilayers in the PVD system at NREL:

Run 1. 500 °C, 2.5 minutes

Run 2. 550 °C, 4.5 minutes

Run 3. 550 °C, 10 minutes

A safety limit on the PVD system restricted the ramp rate to 3 °C/s for all three experiments. This ramp rate is about 10 times faster than the regular ramp rate used in the normal PVD process.   As discussed in the background section, a faster ramp rate enhances the reaction of these two layers by forming a liquid phase and results in a lower substrate temperature and shorter processing time. A conventional RTA system can have a ramp rate up to 120 °C/s. Therefore, a conventional RTA system should allow the formation of CIS at lower process temperature and shorter processing time compared to the PVD system.

As seen from the XRD pattern in Figure 3-22, only the CuSe phase is present in the precursor (before RTP). The bottom InSe phase does not show any peaks because it is in the amorphous state. The SEM cross section of the precursor (Figure 3-24b) shows the separate InSe and CuSe layer of thickness about 1 μm each. The plane view of the precursor (Figure 3-24a) shows the hexagonal CuSe grains. The shoulder near (112) peak in the XRD pattern (Figure 3-25) of the film after Run 1 indicates the formation of the high temperature $Cu_{2-x}Se$ phase. The bright dots in the plane view micrograph indicated by an arrow in the figure 3-26a points out the $Cu_{2-x}Se$ phase. The cross-sectional micrograph (Figure 3-26b) shows the small grain site in the bottom portion of the layer because of incomplete nucleation of CIS. It is believed that these small grains are not well nucleated CIS grains and that the bottom InSe is completely consumed as evidenced by absence of InSe secondary phase by XRD (usually InSe will crystallize

upon heating). This also suggests that In diffusion in CuSe is slower than Cu diffusion into InSe. This is because the In atom is larger than the Cu atom, and InSe is amorphous which makes the Cu diffusion much easier.

EPMA is a useful technique to determine the existence of any Cu rich secondary phases because it probes the upper layer composition, and Cu-rich secondary phases tend to segregate near the surface [47]. The EPMA composition for this film after Run 1 is Cu: 27.9 at.%, In 24.1 at.%, Se 48.0 at.% yielding a Cu/In ratio of 1.16. This result is consistent with the existence of a Cu-rich secondary phase. Therefore, the temperature was increased to 550 °C and the soak time increased to 4.5 min in Run 2 to enhance In diffusion and thus formation of CIS in the top CuSe layer. The XRD pattern (Figure 3-27) shows the single CIS phase and the disappearance of $Cu_{2-x}Se$ on the surface as suggested by the SEM plane view micrograph (disappearance of small surface grains in Figure 3-28(a)). The grain size in the bottom layer enlarged (Figure 3-28(b)). The composition as determined by EPMA for film after run 2 is Cu 23.5 at.%, In 26.5 at.% and Se 50.0 at.% with Cu/In ratio of 0.887 and this ratio lies in single phase CIS region. This suggests that the top layer is also fully converted to the CIS phase. To promote CIS grain growth in the bottom layer, a longer soak time, 10 min was tried (Run 3). From the SEM picture cross-section micrograph shown in Figure 3-29(b), a relatively homogenous grain size is evidence throughout the film, and the plane view SEM micrograph shows highly textured CIS grains as in Figure 3-29(a) and this is the highly oriented CIS 112 peak.

I-V Measurements

The next step was to fabricate cells from the absorbers synthesized in Runs 1-3. The I-V measurement for the first device is shown in Figure 3-30 (without Se overpressure after Run 1). The device is shorted apparently due to the presence of the conducting $Cu_{2-x}Se$ phase. For Run 2 with XRD and SEM suggesting single phase CIS with two different grain size layers, the efficiency is 2.78 %. Further increase of grain size (Run 3) produced an increased efficiency of 5.08 %. The J_{sc} for this 5 % cell is 34.65 mA/cm^2, which is a good value for CIS. Fill factor and V_{oc}, however, are very low. A high sheet resistance contributes to the low fill factor. This can be improved by adjusting the Cu:In:Se composition ratio and thus the doping level, especially Cu to In ratio and by creating a composition gradient to achieve the bandgap grading with the incorporation of Ga. The V_{oc} is largely affected by the mid gap defects in the space charge region. To detect the defect level in this 5 % cell, a Deep Level Transient Spectroscopy (DLTS) measurements were performed on this 5 % cell and the results are presented in Chapter 4.

3.4.4 RTP Experiments on InSe/CuSe/Mo/Glass Precursors

A preliminary study of samples with the In-Se binary layer on the top of the Cu-Se layer (precursor structure InSe/CuSe/Mo/glass) was undertaken. Samples with this structure, when processed at 450 to 600 °C, showed a rough surface morphology after the RTP as shown in Figure 3-31 (a). This is believed to be a result of poor adhesion of the bottom layer to Mo layer. Therefore, a seed thin layer of InSe was first deposited on the Mo/Glass substrate to give structure InSe (1 μm)/CuSe (1 μm)/InSe(500 Å)/Mo/Glass. This structure greatly improves the surface morphology as seen in the optical micrograph

as shown in Figure 3-31(b). The structure and process conditions however need to be optimized to make device quality films.

3.5 Conclusions

An alternative low temperature route to $CuInSe_2$ formation was demonstrated using RTP on the stacked precursor structure Cu-Se/In-Se/Mo/glass. The influence of various ambient compositions on phase transformations after RTP was determined. A short time annealing of 60 s at 480 °C in a Se ambient generated by volatilization of a thin Se layer on the sample cover, followed by a second anneal using a clear cover, was able to produce single-phase α-$CuInSe_2$ with relatively large grain size. The high melting temperature secondary phase $Cu_{2-x}Se(s)$ does not react with InSe without Se overpressure. Based on these results, a 5.08% device with V_{oc}= 0.296 V, J_{sc} = 34.65 mA/cm^2 and fill factor = 49.54% was fabricated using the absorber that is obtained by RTP on the CuSe/InSe/Mo/Glass precursor under Se control in a PVD system. It is worth noting that this 5.08% cell was achieved without full optimization of the process. Therefore, the RTP on binary bilayer process is promising.
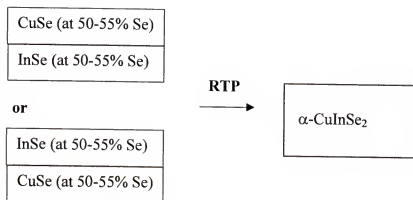
Figure 3-1. Novel precursor structure consisting of stacked metal-Se layers.

(a)
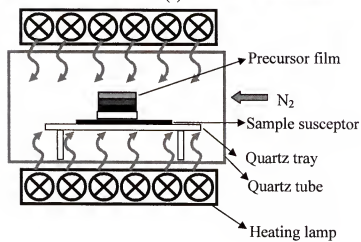
(b)

Figure 3-2. AG Associates Heatpulse 4100 RTP system (a) front
view, (b) schematic of the oven.

Sample
graphite
0.5 mm thick
4" Diameter

(a)

Quartz lid
2" Diameter
Sample
graphite
0.5 mm thick
4" Diameter
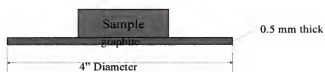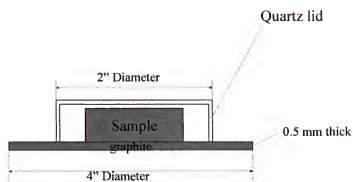
(b)
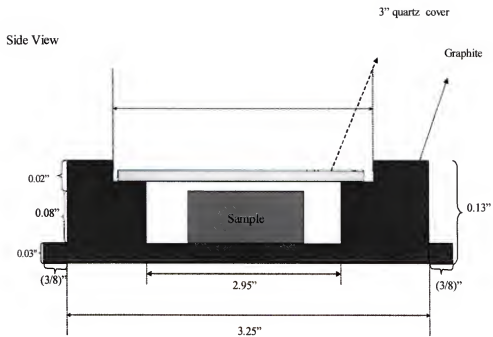
(c)

Figure 3-3. Susceptors design schematic (a) I, (b)II, and (c) III.
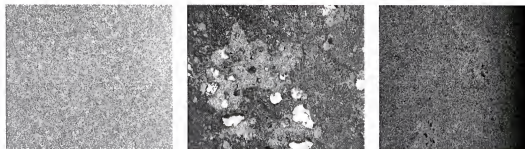
(a) Trial sample before RTP.

(b) Trial sample after RTP by using silicon wafer as the susceptor.

(c) Trial sample after RTP by using graphite wafer as the susceptor.

Figure 3-4. Comparison of film optical micrograph when using Si or graphite as the susceptor at magnification 10x.
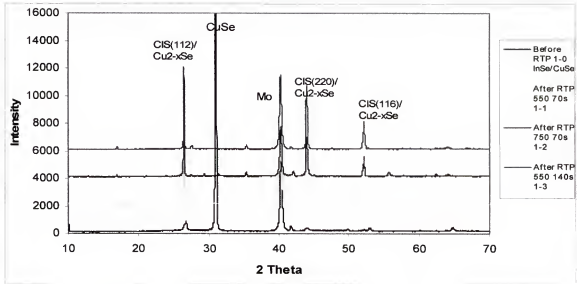
Figure 3-5. XRD pattern comparison for the films at different RTP conditions (Susceptor I).
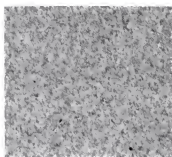
(a) Plane-view optical micro-graph of sample 1-0 before RTP
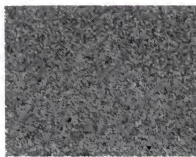
(b) Plane-view optical micro-graph picture of sample 1-1

(c) Plane-view optical micro-graph picture of sample 1-2

Figure 3-6. Optical micrographs of 1-0, 1-1 and 1-3 samples at magnification 10x.
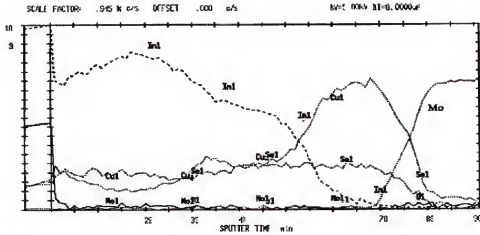
Figure 3-7 (a). Auger depth profile of sample 1-0 before RTP [44].
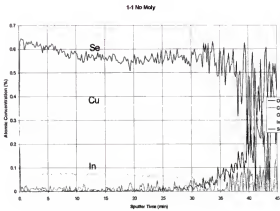
Figure 3-7 (b). Auger depth profile of sample 1-1.
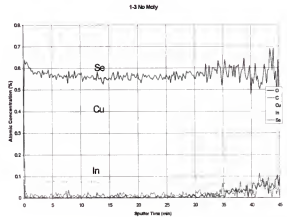
Figure 3-7 (c). Auger depth profile of sample 1-3.

Figure 3-7 Auger profile (a) of sample 1-0 before RTP (b) of sample 1-1. (c) sample 1-3
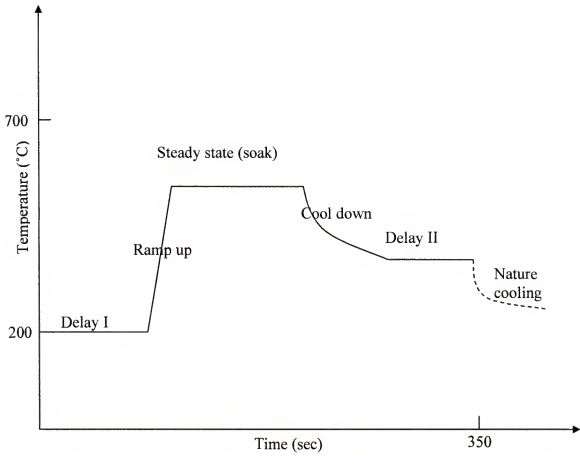
Figure 3-8. Typical Cycle time for Rapid Thermal Processing
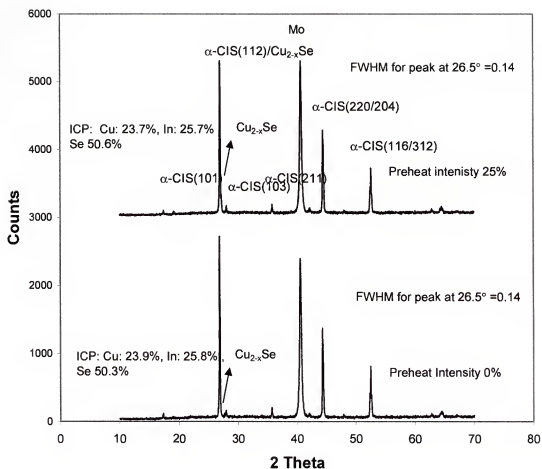
Figure 3-9. The influence of preheat intensity on the phase formation (XRD pattern) and film composition (ICP).
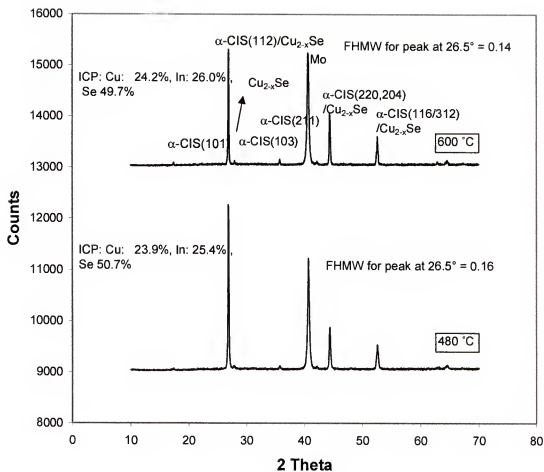
Figure 3-10. The effect of soak temperature at shorter soak time (XRD pattern and film composition by ICP).
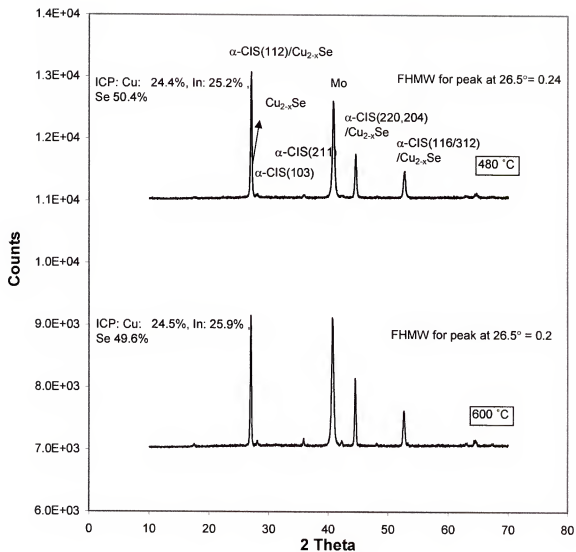
Figure 3-11. The effect of soak temperature at longer soak time (XRD pattern and film composition by ICP).
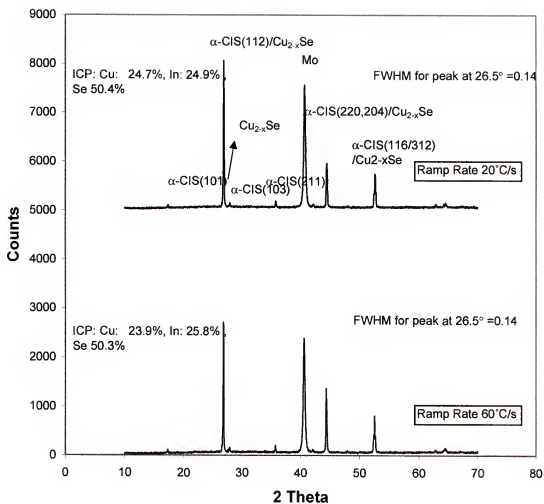
Figure 3-12. The effect of ramp rate (XRD pattern and film composition by ICP).
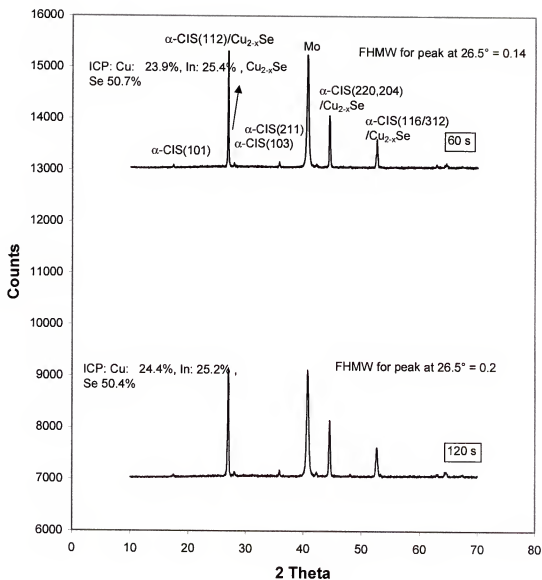
Figure 3-13. The influence of soak time at higher steady state temperature on phase formation
(XRD pattern) and film composition (ICP).
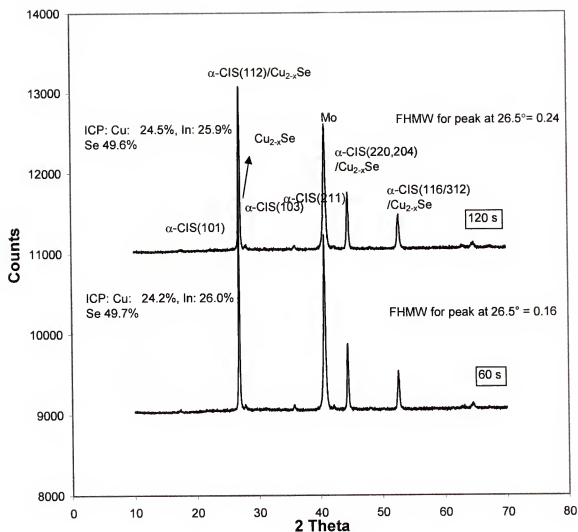
Figure 3-14. The influence of soak time at lower steady state temperature on phase formation (XRD pattern) and film composition (ICP).
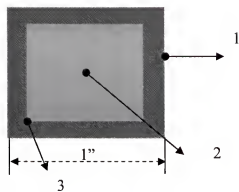
Figure 3-15. Non-uniformly heated surface.
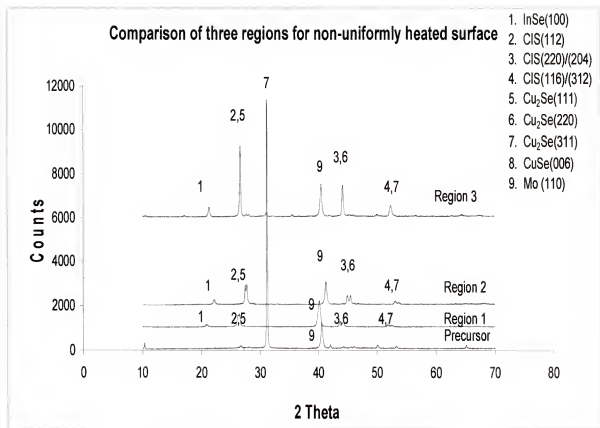
Figure 3-16. XRD pattern of different regions of non-uniform heated surface (see Fig. 3-16).

(a)
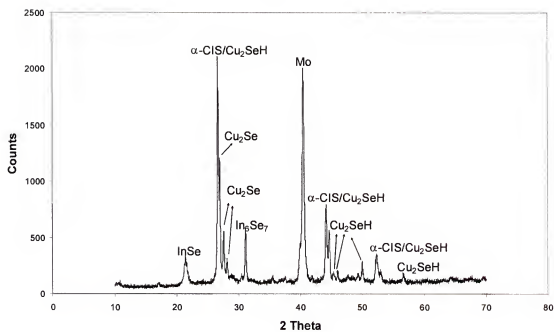
(b)

Figure 3-17. Film after step I: 480°C, 60s, 60°C/s (a) structure (b) XRD pattern.

(a)

(b)
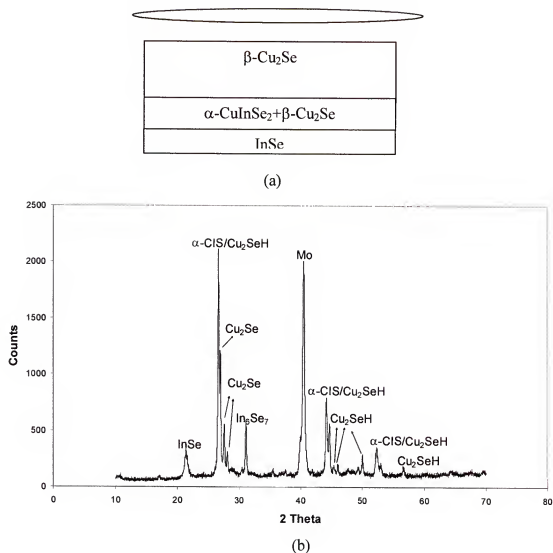
Figure 3-18. Film using higher temperature for step **I:** 550˚C, 120s, 60˚C/s (a) structure (b) XRD pattern.

(a)

(b)
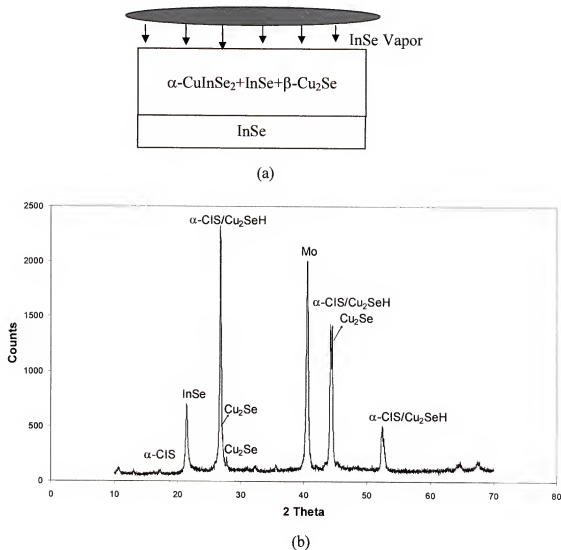
Figure 3-19. Film after step **II:** 480˚C 60s, 60˚C/s with InSe lid (a) structure (b) XRD pattern.
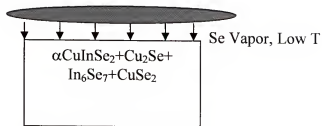
(a)
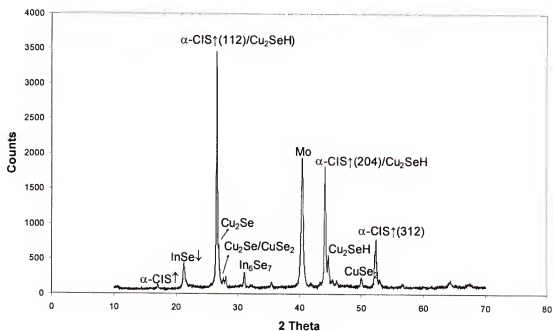
(b)

Figure 3-20. Film after step III: 480˚C 60s, 60˚C/s with Se lid (a) proposed structure (b) XRD Pattern.

α-CuInSe$_2$ + very small amount
InSe
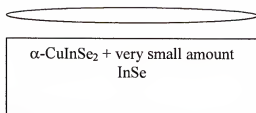
(a)
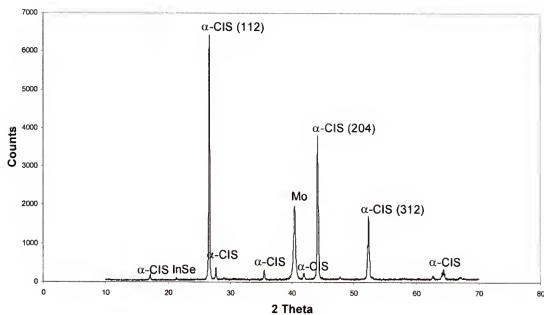
(b)

Figure 3-21. Film after step IV: 550°C 70s 60°C/s with clear lid (a) structure (b) XRD pattern.

(a)

Composition from ICP:
Cu 24.28% In 26.43% Se 49.28%
Cu/In ~ 0.92

(b)
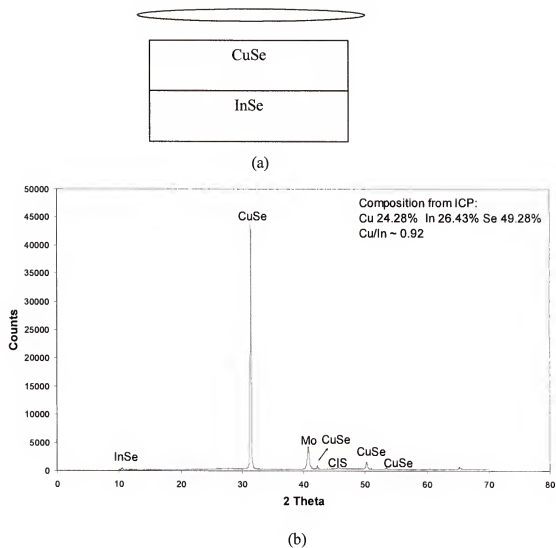
Figure 3-22. Precursor (a) structure (b) XRD pattern and composition data.
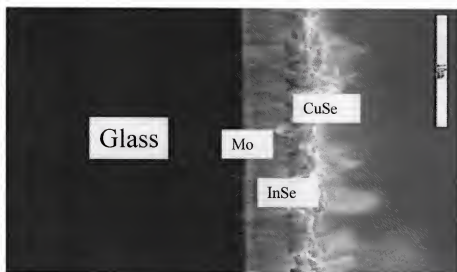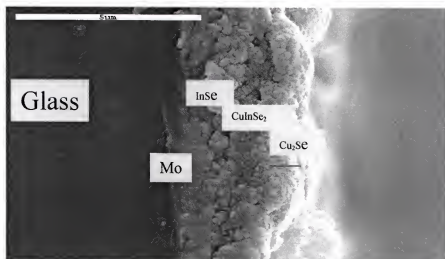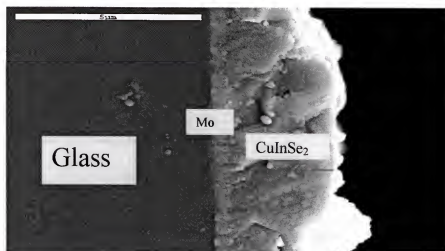
Figure 3-23. SEM cross-sectional micrograph of (a) precursor, (b) after step I, and (c) after step IV.
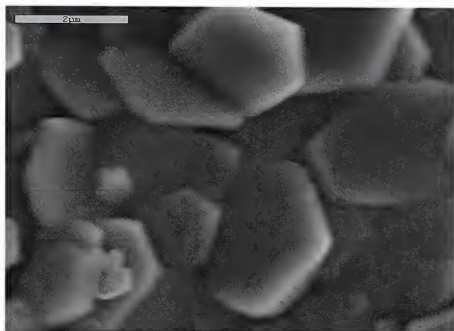
(a)
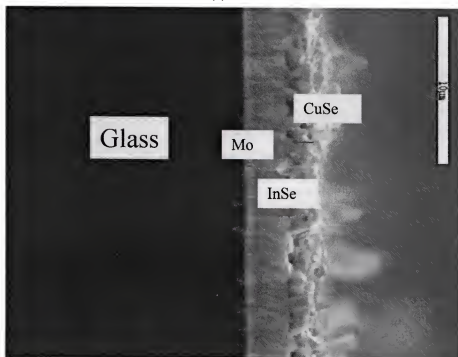
(b)

Figure 3-24. SEM micrograph of the precursor (a) plane view (b) cross-section.
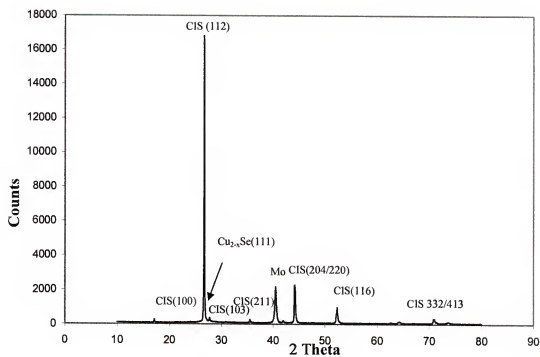
Figure 3-25. XRD pattern after RTP at 500 ºC for 2.5 min (Run 1).

(a)
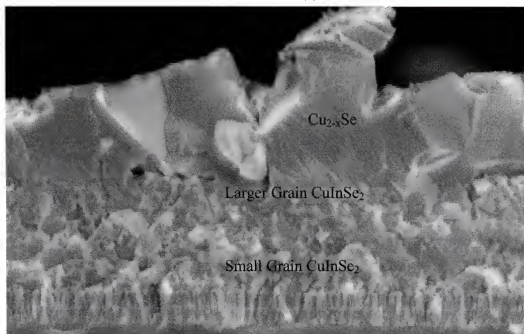
(b)

Figure 3-26. SEM micrograph of film after RTP at 500 ºC for 2.5 min (Run 1) (a) plane view (b) cross-section.
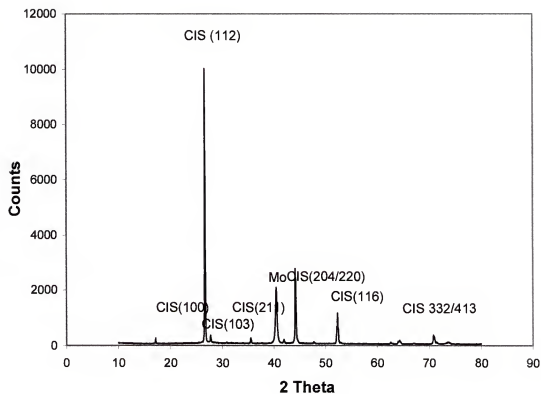
Figure 3-27. XRD pattern after RTP at 550 ºC for 4.5 min (Run 2).
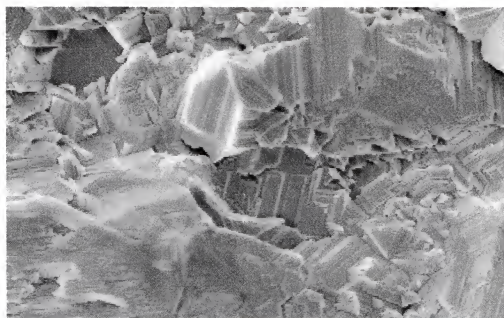
550 C, 4.5 min   **1μm 30000X**

(a)
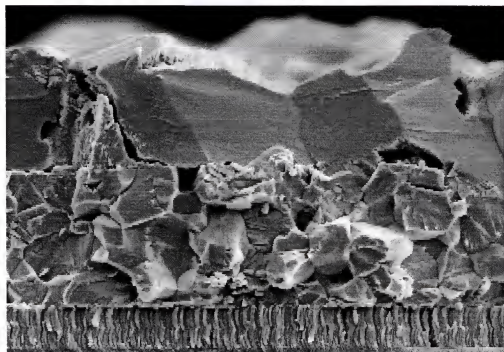
550 C, 4.5 min   **1μm 30000X**

(b)

Figure 3-28. SEM micrograph of film after RTP at 550 ºC for 4.5 min (Run 2) (a) plane view (b) cross-section.
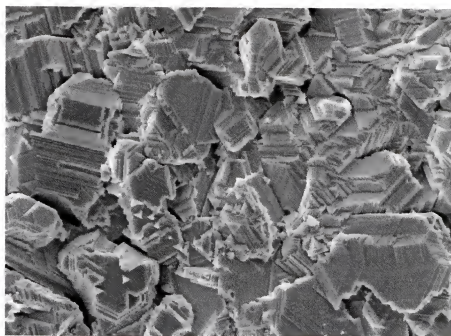
550 C, 10 mins   **1µm 30000X**

(a)
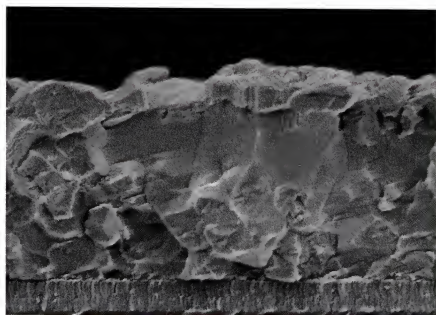
550 C, 10 mins   **1µm 25000X**

(b)

Figure 3-29. SEM micrograph of film after RTP at 550 °C for 10 min (Run 3) (a) plane view (b) cross- section.

I-V Curve	V_{oc} (V)	J_{sc} (mA/cm^2)	I_{sc} (mA)	FF (%)	Eff (%)
	0.025	-0.48	-0.21	23.42	0.000
	0.024	-4.34	-1.86	24.25	0.025
	0.262	-30.36	-13.05	35.09	2.79
	0.296	-34.69	-14.9	49.54	5.08
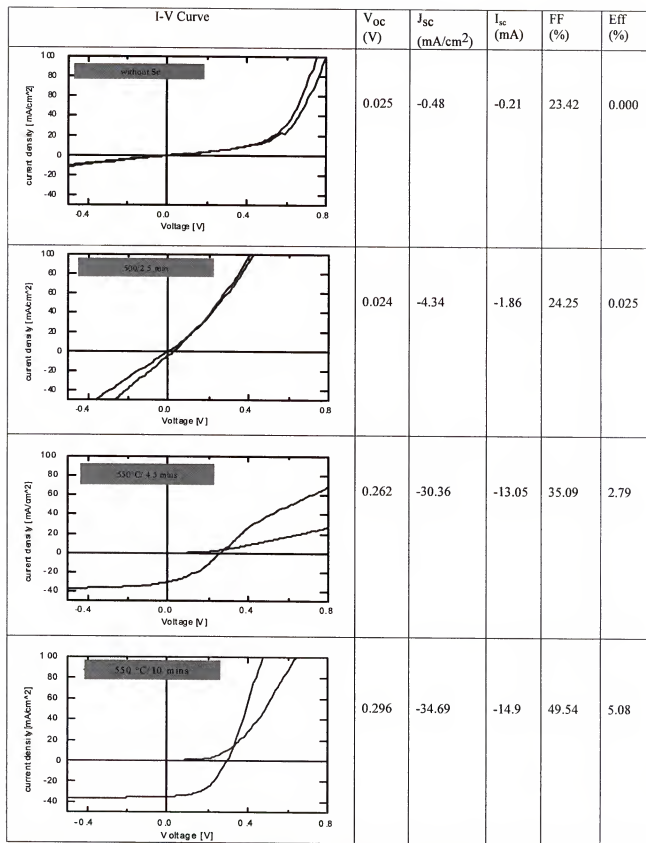
Figure 3-30. I-V curves for the cells fabricated after without Se control and Runs 1-3 with Se control.
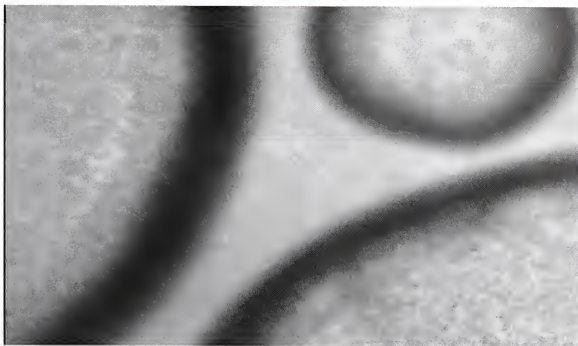
(a)
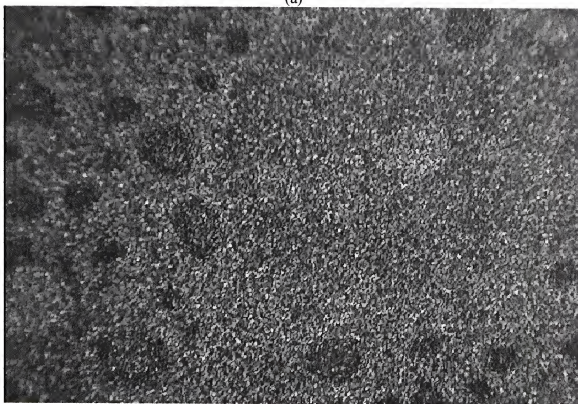
(b)

Figure 3-31. Optical plane view micrograph absorber film after RTP process on inverted structure precursor (a) InSe/CuSe/Mo/Glass (b) InSe/CuSe/InSe/Mo/Glass at magnification 10x.

CHAPTER 4
INVESTIGATION OF DEEP-LEVEL DEFECTS IN CU(IN,GA)SE$_2$ SOLAR CELLS BY DEEP-LEVEL TRANSIENT SPECTROSCOPY

It is well known that CuInGaSe$_2$ (CIGS) has a large homogeneity range, and such deviation from stoichiometry in compound semiconductors is often attributed to antisite defects, vacancies, interstitials, and defect clusters in the material. It is important to understand these properties to further improve the cell efficiency and reduce the cost of solar energy. Deep level defects play an important role in determining the recombination and trapping mechanisms (and hence the minority carrier lifetimes) in a semiconductor. Deep level transient spectroscopy (DLTS) is a high frequency transient capacitance technique and is the most sensitive technique for defect detection. Zhang [31, 32] has calculated the transition energy for a large number of defects in CIS, and the results are summarized in Figure 2-4. However, there are some discrepancies between his calculation and experimental observations. According to the PL measurement by Schoon [33], In_{Cu} should be a shallower donor than Cu_i and has transition energy about 0.2 eV below conduction band. In Zhang's calculation, the anion site defect is neglected. However, many other researches believe that V_{Se} is the shallowest donor level [33] with energy level of transition E_c- 0.06 eV and results in a significant lattice relaxation during the ionization process. Knowledge of the defect energies as well as their densities are important inputs to developing meaningful device models. DLTS is a standard diagnostic technique for determining the trap properties such as trap energy level, capture cross section, and trap concentration.

4.1 DLTS Principles and Experimental Procedures

Deep level defects play an important role in determining the recombination and trapping mechanisms (and hence the minority carrier lifetimes) in a semiconductor. The deep level transient spectroscopy (DLTS) is a high frequency transient capacitance technique and is the most sensitive technique for defect detection [17]. For a n^+-p (CdS-CIGS) junction diode, the space charge region extends mainly into the p-region, and the local charges are due to negatively charged ionized acceptors. If a forward bias is applied, the electrons will be injected into region. Once the minority electrons are trapped in a defect level, the net negative charges in the SCR will increase. This in turn will reduce the width of SCR, and causes a positive capacitance change. Thus, the DLTS signal will have a positive peak. If holes are injected into the SCR and captured by the majority carrier traps, the DLTS signal will have a negative sign. Figure 4-1 shows the deep level filling sequence.

A boxcar integrator [48] uses a fast sampling technique to obtain an average of the repeated signal transients on some set time which we will call t_1. The double boxcar has the capacity to sample the signal at times, which are termed t_1 and t_2. An analog circuit is used to integrate or average the value of ΔC over the two fixed times which are called windows. Figure 4-2 shows how the rate window works in the analysis of DLTS data. The left side of the figure 4-2 indicates the response of the transient signal, it can be written as

$$\Delta C(t) = \Delta C(0)\exp(-e_n t) \qquad (4.1)$$

If we define time constant $\tau = 1/e_n$, the above equation can be written as

$$\Delta C(t) = \Delta C(0)\exp(-t/\tau) \qquad (4.2)$$

The right side is the resulting DLTS output signal for this fixed rate window. It is

$$\Delta C(t_2) - \Delta C(t_1) = S(\tau) = \Delta C(0)[e^{-t_2/\tau} - e^{-t_1/\tau}] \qquad (4.3)$$

To have the maximum of $S(\tau)$, we need to have $\dfrac{dS(\tau)}{d\tau} = 0$, and this occurs at

$$\tau = \frac{t_1 - t_2}{\ln(t_1/t_2)} \qquad (4.4)$$

Thus, the emission rate corresponding to the maximum of a trap peak observed in a DLTS thermal scan is a precisely defined quantity. If we have a series of temperature measurements using different t_1 and t_2, one can calculate the activation energy using an Arrhenius plot.

DLTS is used to measure the transient capacitance change of a junction device after deep-level traps in the space charge region have been filled with either the majority or minority carrier charges, and the trap density and energy levels of these deep level traps can be extracted from DLTS measurements. By scanning the transient capacitance over a range of temperature, the emission rate as a function of temperature can be obtained. The activation energy for an electron trap and capture cross section can be estimated from an Arrhenius plot:

$$e_n = \frac{1}{\tau} = \sigma_n v_{th} N_c \exp(-\frac{E_a}{kT}) \qquad (4.5)$$

where e_n is the electron emission rate, σ_n is the capture cross section, N_c is the electron effective density of states and v_{th} is the electron thermal velocity. The electron trap density, N_T, can be calculated by

$$N_T = \frac{2\Delta C}{C_0} N_a \qquad (4.6)$$

Equation (4.6) is valid for $N_T < N_a$. ΔC is the height of capacitance change due to the emission of charge carriers from the trap level, which is proportional to the probed trap concentration. Carrier concentration, N_a, is determined by the C-V measurements, which give the average carrier concentration in the CIGS absorber layer. C_0 is the zero bias capacitance that is obtained from the C-T data at the corresponding DLTS peak temperature.

4.2 Results and Discussions

DLTS studies were conducted on three types of thin-film photovoltaic cells:

(i)   CIS cells (denoted "UF CIS cells" in the suite for easy reference) developed by the University of Florida using a bilayer precursor process.

(ii)   CIGS cells (denoted "EPV CIGS cells") developed by Energy Photovoltaics Inc. using a physical-vapor deposition process.

(iii)   CIGS cells (denoted "NREL CIS cell") developed by the National Renewable Energy Laboratory using a three-stage precursor process.

Details of the analysis results are discussed in detail below.

4.2.1 UF Samples from Binary Bilayer Rapid Thermal Process

As presented in Chapter 3, the I-V curve for the 5% cell showed a V_{oc}= 0.296 V and fill factor = 49.54%. The J_{sc} for this cell is 34.65 mA/cm^2, which is a very good value for CIS cells. The low fill factor is largely due to the high sheet resistance. This can be improved by adjusting the Cu:In:Se composition ratio, especially Cu to In ratio and and by creating a composition gradient to achieve the bandgap grading with the incorporation of Ga. The V_{oc} is largely affected by the mid gap defects in the space charge region. To detect the defect level in this 5% cell, a Deep Level Transient Spectroscopy (DLTS) measurement was performed on this 5% cell.

Figure 4-3 shows the C-V measurements on the 5% UF cell at different temperatures. The carrier concentration is on order of 10^{15} cm^{-3}. The C-V data was measured on the same cell as that used in the DLTS measurement.

Figure 4-4 shows the measured capacitance versus temperature for the 5% UF cell, which yields the value for C_0 at the corresponding temperature of the DLTS peak. The DLTS spectra measured for this 5% sample with a reverse bias voltage, V_R =-0.5 V, a trap-filling pulse of 0.4 V, and a saturation pulse width of 10 ms are shown in Figure 4-5. The sample is maintained at reverse bias. The 5% sample shows a deep majority carrier trap (negative signal) at a temperature around 290 K. The activation energy calculated from the Arrhenius plot as shown in Figure 4-6 is 0.54 eV above valence band, which may be attributed to the Cu on In interstitial (E_{A6}) according to the diagram shown in Figure 2-4. The average carrier concentration at 290 K from the C-V measurements is 2×10^{15} cm^{-3}. Combing the C-T and C-V scans, N_T is determined to be 4.6×10^{12} cm^{-3}.

To detect possible minority traps, the sample was cooled down to 77 K to freeze out all the minority traps. The sample was then heated with a pulse amplitude equal to 0.7 V at the same reverse set-off voltage of -0.5 V and a saturation pulse width of 10 ms to observe the capacitance change due to the minority carrier emission. As expected, a minority carrier trap peak was observed at a lower temperature ~200 K as shown in Figure 4-7. This minority carrier trap is in addition to the majority trap that was observed. The activation energy is 0.52 eV below the conduction band as shown in Figure 4-8. A possible physical origin of this electron trap is the actually the same as the majority trap, which is Cu on In interstitial [31-32]. The trap density is estimated to be 1.3×10^{12} cm^{-3}.

Optical DLTS was also performed on this 5% sample. In optical DLTS, a laser with wavelength of 532 nm is applied with a reverse bias of 0.5 V. Only minority traps were observed in the optical DLTS spectra as shown in Figure 4-9. The activation energy calculated for E_1 is 0.16 eV shown in Figure 4-10. This trap is attributed to In on Cu site defect In_{Cu}. The activation energy for the E_2 defect at 300 K could not be estimated since the peak shift did not follow the trend; the shorter the rate window, the higher the temperature at which the peak appears. Likely, this is because the capture cross-section is a thermally activated process, and it is related to temperature by [17]

$$\sigma = \sigma_0 e^{-\Delta E/kT} \tag{4.7}$$

4.2.2 EPV CIGS Sample

The EPV samples are produced by the co-deposition in a physical vapor deposition (PVD) system. The DLTS spectra measured from the EPV sample with a reverse bias voltage, $V_R = -0.1$ V, a trap-filling pulse of 0.3 V, and a saturation pulse width of 10 ms is shown in Figure 4-11. The EPV sample showed a deep majority carrier trap (negative signal) at a temperature around 270 K. The DLTS peak shifts to higher temperatures with shorter rate windows. Since the CIGS film is p-type material, the majority carrier trap is referred to as a hole trap, and the minority carrier trap as an electron trap. The activation energy calculated from the Arrhenius plot is 0.94 eV as shown in Figure 4-12, which may be attributed to the Se vacancy V_{Se} according to the diagram shown in Figure 2-4.

Figure 4-13 shows the C-V data measured on the same EPV cell as that used in the DLTS measurement. The average carrier concentration at 270 K from the C-V

measurements is 3×10^{15} cm^{-3}. From the C-T scan (Figure 4-14), C_0 in Eqn. (4.6) was found to be 3.01 pf, and N_T was determined to be 6.5×10^{13} cm^{-3}.

4.2.3 NREL CIGS Sample from Three Stage Process

The absorber from NREL was deposited by three stage process [16] in a PVD system. A solar cell 19.2% total area efficiency based on Cu(In,Ga)Se$_2$ thin film material has been produced via their three stage process. In the first stage, the precursor (In,Ga)$_2$Se$_3$ layer is formed by the coevaporation of In, Ga and Se elemental source at substrate temperature about 260˚C. In the second stage, the Cu and Se are coevaporated to bring the overall composition to near Cu-rich regime (Cu/(In+Ga) ~ 0.97 − 1.08) at 560˚C. Between the second stage and third stage, the substrate is under the Se flux while ramping up the temperature. During the third stage, In, Ga and Se are added with the amount one ninth of the first stage to bring the overall composition back to Cu-poor at the same substrate temperature as the second stage. Then, the film is cooled down to 350 ˚C by Se flux for 20 min. This process requires very precise control of the source fluxes.

A pulse amplitude equal to 0.4 V was applied to the NREL CIGS sample at a reverse set-off voltage of -0.5 V. A minority carrier trap peak was observed at a lower temperature of around 100 K as shown in Figure 4-15. The activation energy is 0.067 eV below the conduction band as shown in Figure 4-16. A possible physical origin of this electron trap is the Se vacancy (V_{Se}) [33]. The trap density is estimated to be 4.2×10^{13} cm^{-3}. The DLTS scan at higher temperature showed another possible positive peak, however, the activation energy for this trap could not be resolved by heating the sample above 300 K.

Therefore, it is noted that the minority traps are likely the dominant traps in the NREL sample. To detect other possible minority traps, a small forward bias (0.1 V) was applied and the sample cooled to 77 K to freeze the minority carriers. The sample was then heated with $V_R = -0.5$ V, trap-filling pulse amplitude of 0.7 V, and a saturation pulse width of 10 ms to observe the capacitance change due to the minority carrier emission. Figure 4-17 shows three minority carrier traps with the addition of a small peak around 250 K, which was not apparent in the DLTS spectra of the 0.4 V pulse amplitude. The Arrhenius plot in Figure 4-18 showed that the activation energy for the trap at 80 K is 0.14 eV. The trap density is estimated to be 2.54×10^{13} cm^{-3}. The electron trap observed at 80 K is possibly related to a vacancy on a Se site, which might be the same trap level as the one observed with the 0.4 V pulse amplitude as shown in Figure 4-15. The activation energy at 335 K could not be estimated since the peak shift does not follow the trend; the shorter the rate window, the higher the temperature at which the peak appears.

4.3 Conclusions

The DLTS and C-V measurements have been performed on UF CIS sample and compared with the DLTS measurements on EPV and NREL CIGS samples. The defect activation energy and density were determined from these measurements. Table 4-1 summarizes the DLTS data on 5% cell by RTP on bilayer precursor. In the UF CIS sample, a middle gap majority trap is detected and three other minority traps are also detected. The middle majority trap seems to be the dominant defect in the cell. This confirms the observation of the low V_{oc} in I-V curve. Therefore, to improve the cell efficiency, the junction quality must be improved by reducing the middle gap defect. Adding Ga or S to create the bandgap gradient and adjusting the Cu:In:Se composition

ratio will be the reasonable methods. The EPV sample showed a majority carrier (hole) trap with activation energy and trap density determined. The NREL CIGS sample showed three minority carrier traps. Possible defect origins were suggested from this DLTS study. The results for samples from both locations are listed in Table 4-2. From the analysis in Tables 4-1 and 2, it is concluded that V_{Se} and In_{Cu} are two main donor levels, and V_{Cu} is the shallowest acceptor level, and Cu_{In} is the main middle level recombination center which are consistent with the information from literature [31-33, 37]. The free energy associated with the formation of some defect structures is so small that little increase in thermodynamic potential results and hence there is insufficient driving force to ensure their elimination under many synthesis conditions. The formation energy of these defects in CIS according to several authors calculations are in the order of $V_{Cu} < In_{Cu} < Cu_{In} \approx In_{Cu} < V_{Se}$ [31-32, 37]. However, the defect distribution depends significantly on the stoichiometry.

(a)

t = 0
V = -5 Volts

(b)

t = 10 ms
V = 0 Volts
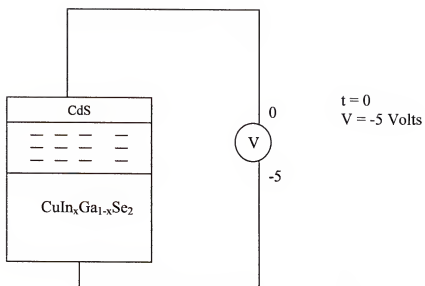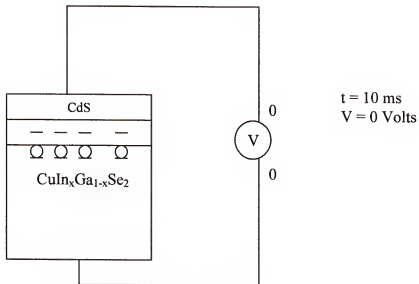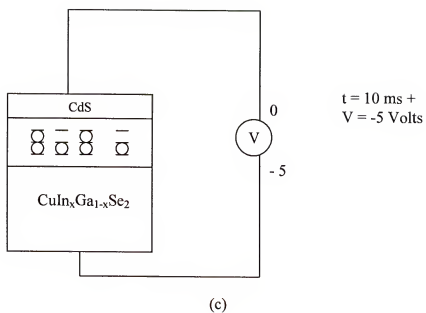
Figure 4-1. DLTS majority trap filling sequence for CdS/CIGS junction (a) under reverse bias without pulse (b) pulse injection (c) after pulse injection.
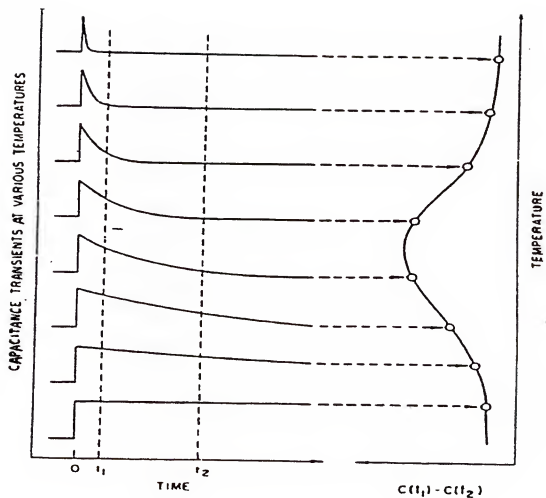
Figure 4-2. Example of how the double boxcar averager is used to define the rate window [48].
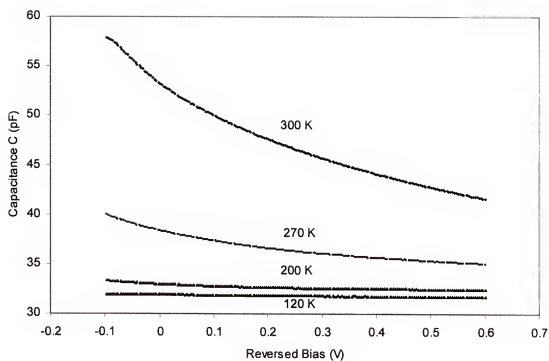
Figure 4-3. Capacitance–Voltage measurement for UF CIS cell.
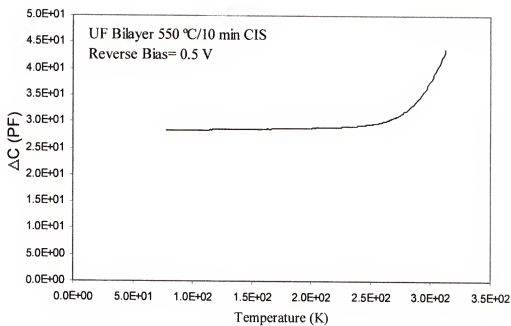
Figure 4-4. Capacitance-temperature measurement of the 5% cell.
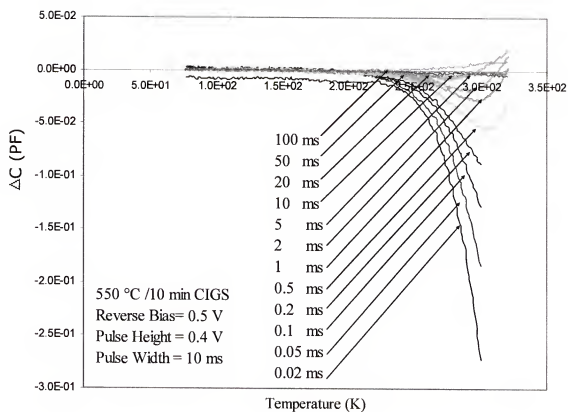
Figure 4-5. DLTS scan for UF 5% cell at a reverse bias of –0.5 V, a pulse height of 0.4 V, and pulse width of 10 ms.
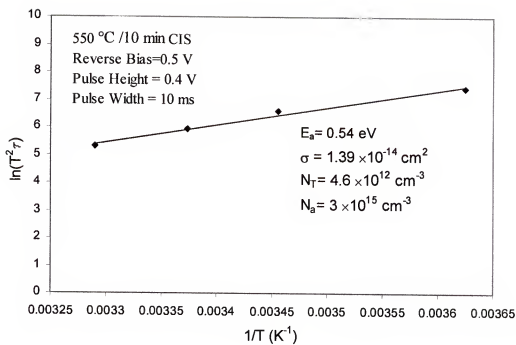
Figure 4-6. The Arrhenius plot of emission rate e_n/T^2 vs. 1/T.
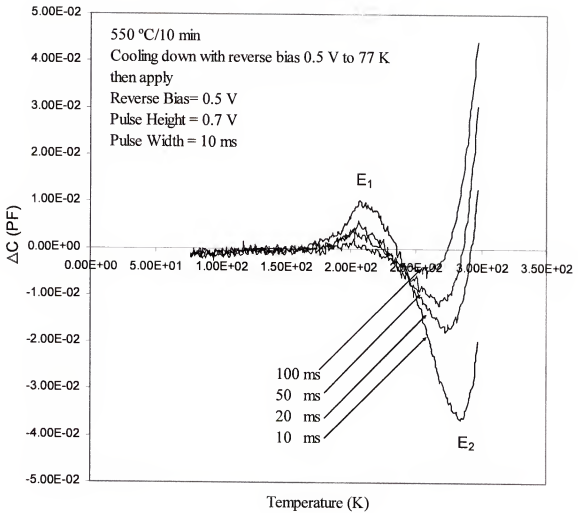
Figure 4-7. DLTS scan for UF 5% cell at a reverse bias of –0.5 V, a pulse height of 0.7 V, and pulse width of 10 ms.
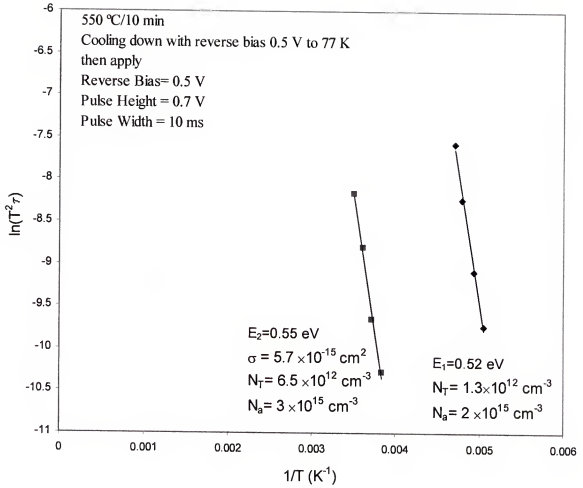
Figure 4-8. The Arrhenius plot of emission rate e_n/T^2 vs. $1/T$ for DLTS scan at reverse bias 0.5V, pulse height 0.7 V and pulse width 10 ms.
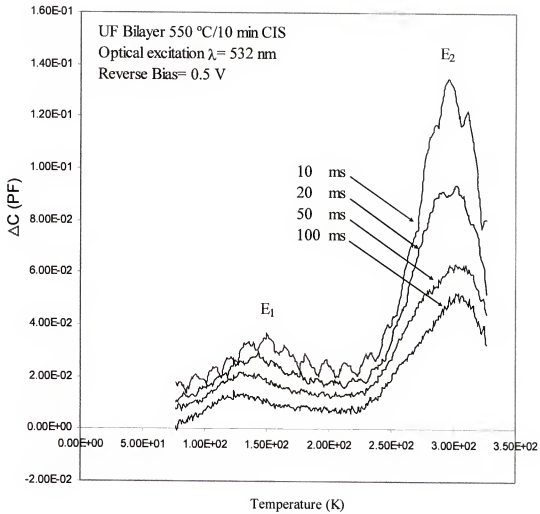
Figure 4-9. Optical DLTS scan for UF 5% cell at a reverse bias of –0.5 V, λ=532 nm, and pulse width of 10 ms.
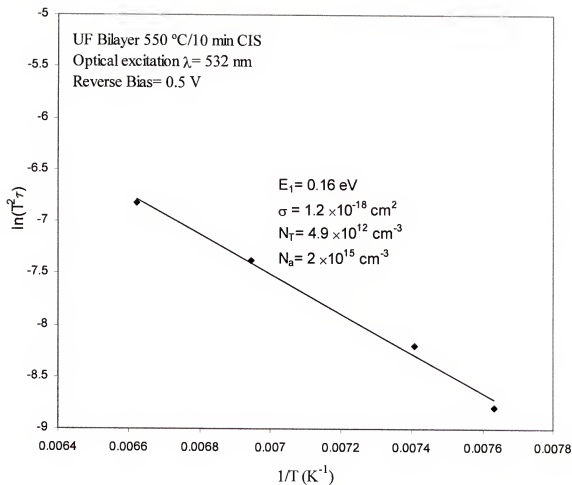
Figure 4-10. The Arrhenius plot of emission rate en/T2 vs. 1/T for DLTS scan at reverse bias 0.5V, pulse height 0.7 V and pulse width 10 ms.
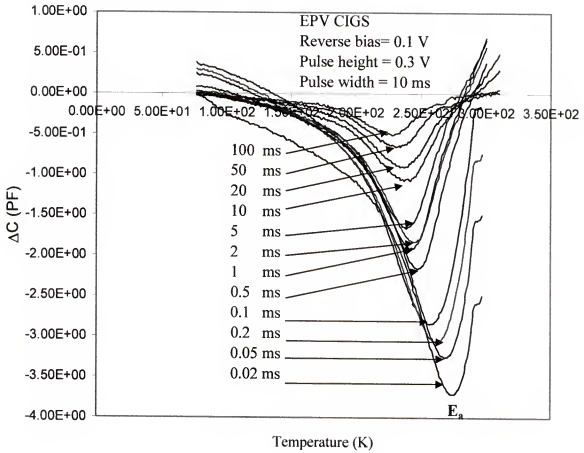
Figure 4-11. DLTS scan for EPV cell at a reverse bias of –0.1 V, a pulse height of 0.3 V, and pulse width of 10 ms.
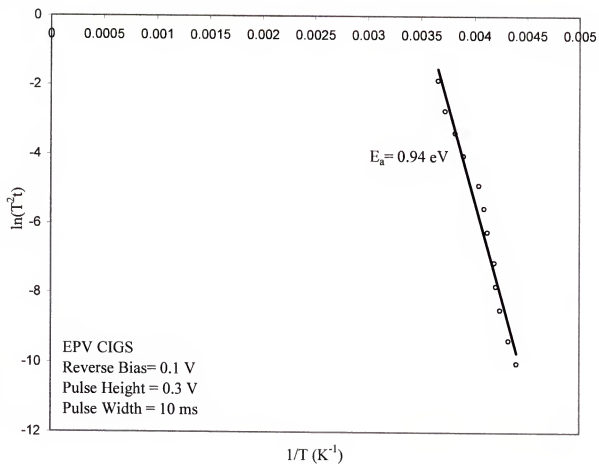
Figure 4-12. The Arrhenius plot of emission rate e_n/T^2 vs. 1/T.

(a)

(b)

(c)

(d)
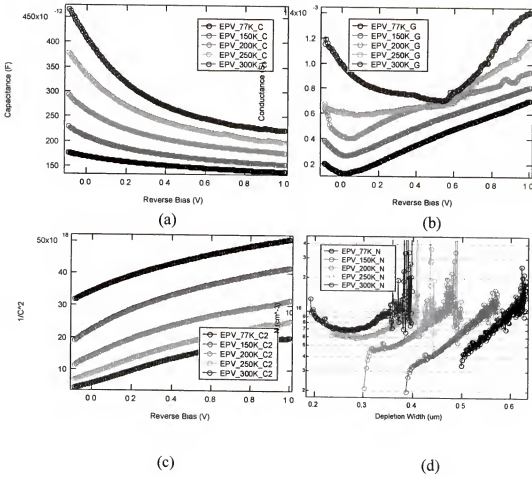
Figure 4-13. C-V data of EPV sample at different temperatures. (a) C-V (b) conductance-voltage (c) $1/C^2$-V (d) carrier concentration-depletion width.
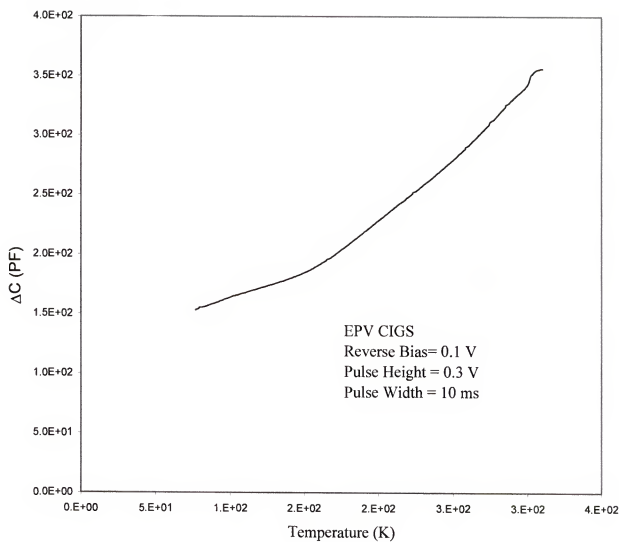
Figure 4-14. The C-T scan for EPV cell at a reversed bias -0.1V.
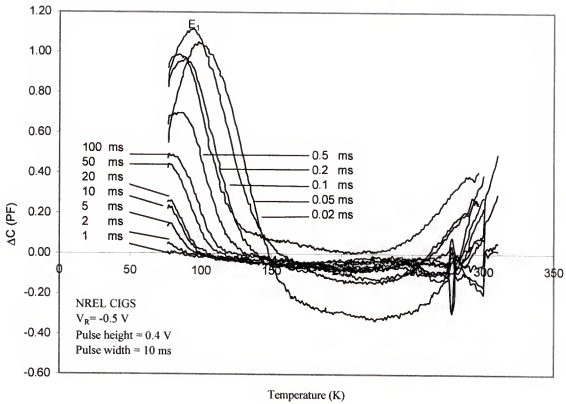
Figure 4-15. DLTS data for NREL sample measured at a reverse bias -0.5 V, pulse amplitude
0.4 V, and pulse width 10 ms.
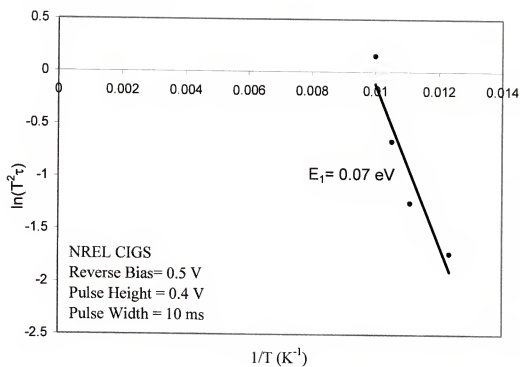
Figure 4-16. Arrhenius plot of the emission rate e_n/T^2 vs. 1/T.
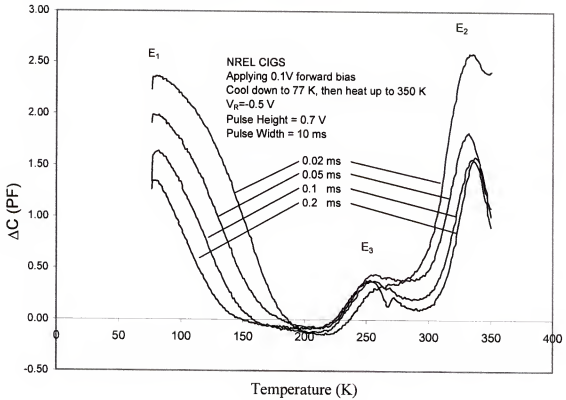
Figure 4-17. DLTS scan for the NREL sample under forward bias (0.1 V) injection, and heat up with reverse bias of -0.5V, pulse height of 0.7V, and pulse width of 10 ms.
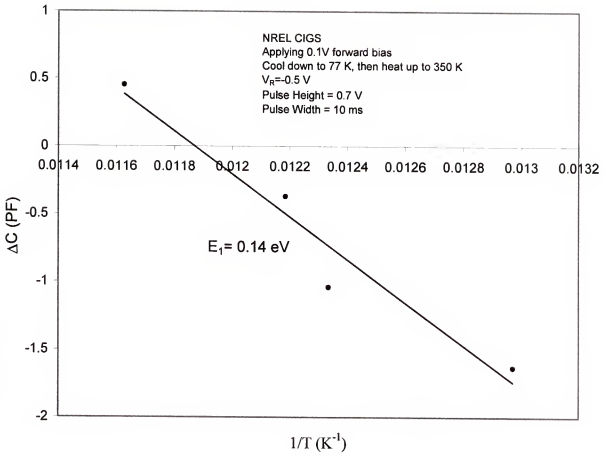
Figure 4-18. Arrhenius plot of emission rate e_n/T^2 vs. $1/T$ for the electron trap E_1.

Table 4-1. Summary of DLTS Data on UF CIS sample

	$V_R = -0.5V$ $V_H = 0.4 V$ $W = 10$ ms	Cool to 77 K with reverse bias - 0.5 V, then apply $V_R = -0.5V$ $V_H = 0.7 V$ $W = 10$ ms		Optical DLTS $V_R = -0.5V$ $\lambda = 532$ nm	
Approximate Peak Temperature (K)	290	290	200	150	300
DLTS peak Sign	-	-	+	+	+
Trap Carrier Type	Majority	Majority	Minority	Minority	Minority
Trap Activation Energy E_a (eV)	$E_V +0.54$	$E_V +0.55$	$E_c -0.52$	$E_c - 0.16$	$E_c - 0.5$ (?)
Trap Density (cm^{-3})	4.6×10^{12}	6.5×10^{12}	1.3×10^{12}	4.9×10^{12}	3.5×10^{13}
Possible Defect I.D.	Cu_{In}	Cu_{In}	V_{Cu}	In_{Cu}	Cu_{In}
Capture Cross Section σ (cm^2)	1.39×10^{-14}	5.7×10^{-15}		1.2×10^{-18}	

Table 4-2. Summary of DLTS and C-V data for the EPV and NREL samples.

	EPV CIGS	NREL CIGS		
Approximate Peak Temperature	270 K	100K	250 K	335 K
Activation Energy (eV)	$E_v+0.94$	$E_c-0.067$		
DLTS peak	-	+	+	+
Trap Carrier Type	Majority	Minority	Minority	Minority
N_a (cm^{-3})	3×10^{15}	2.25×10^{15}		
N_T (cm^{-3})	6.5×10^{13}	4.2×10^{13}		
Possible defect I.D.	V_{Se}	V_{Se}		
Capture Cross Section σ (cm^2)		6×10^{-18}		

CHAPTER 5

THERMODYANAMIC MODELING OF ISOTHERMAL SECTION 500°C OF THE CU-IN-SE SYSTEM USING DEFECT MODEL

This study aims at establishing a defect model to understand the defect chemistry of the Cu-In-Se system and build a database to calculate the defect and carrier concentrations.

The organization of this chapter is as follows: In the phase equilibria section (5.1), the experimental information on the phase equilibria is summarized and selected as the input data for the computerized optimization of the thermodynamic model parameters. In section (5.2) the thermodynamic models and the pertinent parameters are described. In the results and discussion section (5.3) the optimized parameters are presented.

5.1 Experimental Phase Equilibria Data in the Cu-In-Se System

The most complete and recent study on the phase equilibria of Cu-In-Se are conducted by Gödecke *et al.* [38] using DTA, XRD, TEM and SEM measurements. Figure 2-5 shows the experimental isothermal section of the Cu-In-Se phase diagram at 500 °C over the entire composition triangle. The isothermal section at 500 °C is of major technical importance for the fabrication of thin films for photovoltaic devices because these films are often deposited at temperatures around 500 °C. A summary of all the phase observed equilibria is listed in Table 5-1. There are sixteen phases participating in the equilibria. Of which, nine are solutions: α-CIS (CuInSe$_2$), β_R-CIS (Cu$_1$In$_3$Se$_5$), γ-CIS(Cu$_1$In$_5$Se$_8$), β_H-CIS(Cu$_2$In$_4$Se$_7$), α_{Cu}, η (Cu$_2$In$_1$), δ (Cu$_7$Se$_3$), β-Cu$_2$Se, and Ionic_liquid. The other phase are the line compounds In$_5$Se$_7$, In$_9$Se$_{11}$, In$_6$Se$_7$, γ- In$_2$Se$_3$,

β-In$_2$Se$_3$, InSe and In$_4$Se$_3$. According to their results, in the Se-rich corner and in the In-rich corner, the isothermal section at 500 °C features small regions of liquid phase (L$_4$ and L$_2$, respectively). The α-CIS phase establishes equilibria with eight solid phases and two liquid phases (L$_4$ and L$_2$). Among the solid phases, α$_{Cu}$, η (Cu$_2$In$_1$), and δ (Cu$_7$Se$_3$) originate from the In-Cu boundary system, β-Cu$_2$Se from the Cu-Se boundary system and InSe and In$_4$Se$_3$ from In-Se boundary system. The remaining two phases in equilibrium with α-CIS (CuInSe$_2$) are β$_R$-CIS (Cu$_1$In$_3$Se$_5$) and β$_H$-CIS(Cu$_2$In$_4$Se$_7$).

5.2 Thermodynamic Modeling of Defect-free Cu-In-Se System at 773 K

To stabilize the phase equilibria in the Cu-In-Se system with many phase interactions, it is important to determine the parameters when the CIS compounds are defect free, and assessment of this complicated Cu-In-Se ternary system begins from this point.

5.2.1 Gibbs Energy Data of Defect-free α-CIS (CuInSe$_2$) β$_R$-CIS (Cu$_1$In$_3$Se$_5$), γ-CIS(Cu$_1$In$_5$Se$_8$), and β$_H$-CIS(Cu$_2$In$_4$Se$_7$)

The sublattice model is chosen to describe the α-CIS phases. According to the sublattice model, the defect free Chalcopyrite CuInSe$_2$ (stoichiometry) consists of three sublattices and is presented as

$$(\mathbf{Cu})^I_1(\mathbf{In})^{II}_1(\mathbf{Se})^{III}_2$$
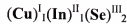
The superscripts, I, II and III identify the sublattices. Analogous to α-CIS, the β$_R$, γ, β$_H$-CIS can be expressed by the following sublattices:

$$(\mathbf{Cu})^I_1(\mathbf{In})^{II}_3(\mathbf{Se})^{III}_5 \text{ for } \beta_R\text{-CIS}$$

$$(\mathbf{Cu})^I_1(\mathbf{In})^{II}_5(\mathbf{Se})^{III}_8 \text{ for } \gamma\text{-CIS}$$

$$(\mathbf{Cu})^I_2(\mathbf{In})^{II}_4(\mathbf{Se})^{III}_7 \text{ for } \beta_H\text{-CIS}$$
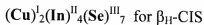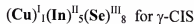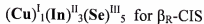
In Chapter 2, three methods are mentioned to evaluate the Gibbs energy of pure compound α-CIS (CuInSe$_2$) β$_R$-CIS (Cu$_1$In$_3$Se$_5$), γ-CIS(Cu$_1$In$_5$Se$_8$), and β$_H$-CIS(Cu$_2$In$_4$Se$_7$). The Gibbs energy data estimated by method **II** in Chapter 2 will be used as the compound Gibbs energy for the defect free α, β$_R$, γ, β$_H$-CIS so that we can express the Gibbs energy of β$_R$, γ, β$_H$-CIS in terms of α-CIS to reduce the number of parameters in the assessment when the defects are incorporated into the sublattices. This is because there is no experimental and calculated data available on the defect energy of β$_R$, γ, β$_H$-CIS. Method **II** will provide an approach to express the pure compound and defects of Gibbs energy of β$_R$, γ, β$_H$-CIS in terms of the pure compound and defects Gibbs energy of α-CIS. In method **II**, the Gibbs energy data for β$_R$-CIS (Cu$_1$In$_3$Se$_5$), γ-CIS(Cu$_1$In$_5$Se$_8$), and β$_H$-CIS(Cu$_2$In$_4$Se$_7$) are obtained by the following equations:

$$°G(β_R \text{ -CIS } (Cu_1In_3Se_5)) = 2.5× °G(α\text{-CIS } (CuInSe_2)+V_1 \qquad (5.1)$$

$$°G(γ\text{-CIS}(Cu_1In_5Se_8)) = 4°G(α\text{-CIS } (CuInSe_2))+ V_2 \qquad (5.2)$$

$$°G(β_H \text{ -CIS}(Cu_2In_4Se_7)) = 3.5× °G(α\text{-CIS } (CuInSe_2))+V_3 \qquad (5.3)$$

The parameters V_1, V_2, and V_3 needed to be estimated. The estimation of V_1, V_2, and V_3 follows the following procedure. First, the magnitude of V_1, V_2, and V_3 are given by $0.5× \Delta H^0_{f,2V_{Cu}+In_{Cu}}$ or $\Delta H^0_{f,2V_{Cu}+In_{Cu}}$ as an initial parameters since m= 0.5 or 1 for every ODC compound. Then, V_1, V_2, and V_3 are optimized by using the Thermo-Calc Parrot module.

5.2.2 Gibbs Energy of Other Phases

As mentioned previously, seven other line compounds and two small liquid phase region also exist in this isothermal 500 °C diagram, in addition to the four CIS compounds. Among the solid phases, α$_{Cu}$, η (Cu$_2$In$_1$), and δ (Cu$_7$Se$_3$) originate from the

In-Cu boundary system, β-Cu$_2$Se from the Cu-Se boundary system and InSe and In$_4$Se$_3$ from In-Se boundary system.

I. Fcc(Cu) Phase

A regular solution model is used to describe the Gibbs energy of the fcc(Cu) phase.

$$(\mathbf{Cu}, \text{Se}, \text{In})$$

Combining the previous Cu-Se and Cu-In binary assessment work [44, 50], the ternary interaction parameter $^{CuFcc}L^0_{Cu,In,Se}$ was added. This parameter needs to be optimized.

II. β-Cu$_2$Se Phase

The β-Cu$_2$Se phase is described by the sublattice model with two Cu sublattices and one Se sublattice represented by the formula:

$$(\mathbf{Cu}, \text{In}, \text{Va})_1 (\mathbf{Se}, \text{Va})_1 (\mathbf{Cu})_1$$
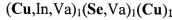
Again a ternary interaction parameter was added to the binary Cu-Se system [44] to model the In solubility, $^{\beta-Cu_2Se}L^0_{Cu,In,Va:Se:Cu}$.

III. The η(Cu$_2$In$_1$), and δ(Cu$_7$In$_3$) Phases

In the binary assessment work [50], both phases are described by a two sublattice model. To model the solubility, the two sublattice model was modified so that all the three elements will be involved.

$$(\text{Cu, In, Se})_2 (\text{Cu, In, Se})_1 \quad \text{for} \quad \eta(\text{Cu}_2\text{In}_1) \text{ phase}$$

$$(\text{Cu, In, Se})_7 (\text{Cu, In, Se})_3 \quad \text{for} \quad \delta(\text{Cu}_7\text{In}_3) \text{ phase}$$
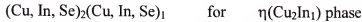
Again a ternary interaction parameter $^{\phi}L^0_{Cu,In,Se:*}$, $^{\phi}L^0_{*:Cu,In,Se}$ was included, where ϕ stands η(Cu$_2$In$_1$) or δ(Cu$_7$In$_3$) phases.

IV. Liquid Phase

The liquid phase is described by an ionic sublattice model with two sublattices, since the ionic two-sublattice model can describe short range ordering and is more straightforward to extend to higher order systems as compared to the chemical theories [55]. Based on the previous work on the modeling of the liquid phase in the Cu-Se, In-Se [44] and Cu-In [50] binary systems, the liquid phase is schematically described in this ternary system as

$$(Cu^{+1}, Cu^{+2}, In^{+3})p(Se^{-2}, Va^{-1}, Se)q$$
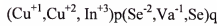
Therefore, three ternary interaction parameters were added to the ionic liquid to describe the Gibbs energy, $^{Ionic\_Liq}L^0_{Cu^{+1},Cu^{+2},In^{+3}:Se^{-2}}$ and $^{Ionic\_Liq}L^1_{Cu^{+1},Cu^{+2},In^{+3}:Se^{-2}}$.

5.2.3 Results and Discussion

The optimized parameters of the stable phases in this Cu-In-Se system with a defect free compound CIS are listed in Table 5-2. The calculated phase diagram over the entire composition range using the optimized parameters is shown in Figure 5-1.

5.3 Defect Model of Off-stoichiometry α-CuInSe₂

5.3.1 Modeling of Gibbs Energy

I.   α-CIS (CuInSe₂)

To model the homogeneity range, the defects have to be incorporated into three sublattices of the stoichiometric chalcopyrite compound α-CIS (CuInSe₂). As reviewed in Chapter 2, four main defects are incorporated into this sublattice model: V_{Cu}, V_{Se}, In_{Cu}, Cu_{In}. Since the model will also incorporate the calculation of free electrons and holes, which is discussed in detail in the next section, it is necessary to consider the donors and acceptors in this phase. In the extrinsic semiconductors, the shallow-level impurities are

used mainly for controlling the carrier concentration and the conductivity of the semiconductor, while the deep-level impurities are used to control the recombination and hence the minority carrier lifetime in a semiconductor [17]. From the review in Chapter 2, the Cu vacancy is a shallow level acceptor and the Se vacancy is a shallow-level donor. To simplify the model in this calculation, one acceptor $V_{Cu}{}^{-1}$ and one donor $V_{Se}{}^{+2}$ are considered. Thus, the sublattices for α-CIS phase can be written as

$$(\textbf{Cu}, \text{In}, \text{Va}, \text{Va}^{-1})^{I}{}_{1}(\textbf{In}, \text{Cu})^{II}{}_{1}(\textbf{Se}, \text{Va}, \text{Va}^{+2})^{III}{}_{2}(\textbf{Va})^{IV}(\textbf{Va})^{V}$$
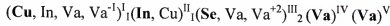
The superscripts, I, II and III identify the sublattices. The major constituents on the normal sublattices are highlighted. The IV and V sublattices are added for incorporation of electrons and holes. For now, just consider the first three sublattices, with the vacancy concentration on sublattices IV and V, $y_{Va}^{IV} = 1$ and $y_{Va}^{V} = 1$.

The Gibbs energy of such a phase α can also be expressed by equation:

$$G^{\alpha} = {}^{ref}G^{\alpha} + {}^{I.D}G^{\alpha} + {}^{ex}G^{\alpha} \tag{5.4}$$

where α stands for non-stoichiometric chalcopyrite α-CuInSe$_2$ phase and each term on the right is expressed as:

For the reference state

$$
\begin{aligned}
{}^{ref}G^{\alpha} = {} & y_{Cu}^{I} y_{In}^{II} y_{Se}^{III} y_{Va}^{IV} y_{Va}^{V}\, {}^{0}G_{Cu:In:Se:Va:Va}^{\alpha} + y_{In}^{I} y_{In}^{II} y_{Se}^{III} y_{Va}^{IV} y_{Va}^{V}\, {}^{0}G_{In:In:Se:Va:Va}^{\alpha} \\
& + y_{Va}^{I} y_{In}^{II} y_{Se}^{III} y_{Va}^{IV} y_{Va}^{V}\, {}^{0}G_{Va:In:Se:Va:Va}^{\alpha} + y_{Va^{-1}}^{I} y_{In}^{II} y_{Se}^{III} y_{Va}^{IV} y_{Va}^{V}\, {}^{0}G_{Va^{-1}:In:Se:Va:Va}^{\alpha} \\
& + y_{Cu}^{I} y_{Cu}^{II} y_{Se}^{III} y_{Va}^{IV} y_{Va}^{V}\, {}^{0}G_{Cu:Cu:Se:Va:Va}^{\alpha} + y_{In}^{I} y_{Cu}^{II} y_{Se}^{III} y_{Va}^{IV} y_{Va}^{V}\, {}^{0}G_{In:Cu:Se:Va:Va}^{\alpha} \\
& + y_{Va}^{I} y_{Cu}^{II} y_{Se}^{III} y_{Va}^{IV} y_{Va}^{V}\, {}^{0}G_{Va:Cu:Se:Va:Va}^{\alpha} + y_{Va^{-1}}^{I} y_{Cu}^{II} y_{Se}^{III} y_{Va}^{IV} y_{Va}^{V}\, {}^{0}G_{Va^{-1}:Cu:Se:Va:Va}^{\alpha} \\
& + y_{Cu}^{I} y_{In}^{II} y_{Va}^{III} y_{Va}^{IV} y_{Va}^{V}\, {}^{0}G_{Cu:In:Va:Va:Va}^{\alpha} + y_{In}^{I} y_{In}^{II} y_{Va}^{III} y_{Va}^{IV} y_{Va}^{V}\, {}^{0}G_{In:In:Va:Va:Va}^{\alpha} \\
& + y_{Va}^{I} y_{In}^{II} y_{Va}^{III} y_{Va}^{IV} y_{Va}^{V}\, {}^{0}G_{Va:In:Va:Va:Va}^{\alpha} + y_{Va^{-1}}^{I} y_{In}^{II} y_{Va}^{III} y_{Va}^{IV} y_{Va}^{V}\, {}^{0}G_{Va^{-1}:In:Va:Va:Va}^{\alpha} \\
& + y_{Cu}^{I} y_{Cu}^{II} y_{Va}^{III} y_{Va}^{IV} y_{Va}^{V}\, {}^{0}G_{Cu:Cu:Va:Va:Va}^{\alpha} + y_{In}^{I} y_{Cu}^{II} y_{Va}^{III} y_{Va}^{IV} y_{Va}^{V}\, {}^{0}G_{In:Cu:Va:Va:Va}^{\alpha} \\
& + y_{Va}^{I} y_{Cu}^{II} y_{Va}^{III} y_{Va}^{IV} y_{Va}^{V}\, {}^{0}G_{Va:Cu:Va:Va:Va}^{\alpha} + y_{Va^{-1}}^{I} y_{Cu}^{II} y_{Va}^{III} y_{Va}^{IV} y_{Va}^{V}\, {}^{0}G_{Va^{-1}:Cu:Va:Va:Va}^{\alpha} \\
& + y_{Cu}^{I} y_{In}^{II} y_{Va^{+2}}^{III} y_{Va}^{IV} y_{Va}^{V}\, {}^{0}G_{Cu:In:Va^{+2}:Va:Va}^{\alpha} + y_{In}^{I} y_{In}^{II} y_{Va^{+2}}^{III} y_{Va}^{IV} y_{Va}^{V}\, {}^{0}G_{In:In:Va^{+2}:Va:Va}^{\alpha} \\
& + y_{Va}^{I} y_{In}^{II} y_{Va^{+2}}^{III} y_{Va}^{IV} y_{Va}^{V}\, {}^{0}G_{Va:In:Va^{+2}:Va:Va}^{\alpha} + y_{Va^{-1}}^{I} y_{In}^{II} y_{Va^{+2}}^{III} y_{Va}^{IV} y_{Va}^{V}\, {}^{0}G_{Va^{-1}:In:Va^{+2}:Va:Va}^{\alpha} \\
& + y_{Cu}^{I} y_{Cu}^{II} y_{Va^{+2}}^{III} y_{Va}^{IV} y_{Va}^{V}\, {}^{0}G_{Cu:Cu:Va^{+2}:Va:Va}^{\alpha} + y_{In}^{I} y_{Cu}^{II} y_{Va^{+2}}^{III} y_{Va}^{IV} y_{Va}^{V}\, {}^{0}G_{In:Cu:Va^{+2}:Va:Va}^{\alpha} \\
& + y_{Va}^{I} y_{Cu}^{II} y_{Va^{+2}}^{III} y_{Va}^{IV} y_{Va}^{V}\, {}^{0}G_{Va:Cu:Va^{+2}:Va:Va}^{\alpha} + y_{Va^{-1}}^{I} y_{Cu}^{II} y_{Va^{+2}}^{III} y_{Va}^{IV} y_{Va}^{V}\, {}^{0}G_{Va^{-1}:Cu:Va^{+2}:Va:Va}^{\alpha}
\end{aligned}
$$

$$(5.5)$$

Including the ideal entropy of mixing

$$
\begin{aligned}
{}^{ID}G^{\alpha} = {} & + \mathrm{RT}(y_{Cu}^{I} \ln y_{Cu}^{I} + y_{In}^{I} \ln y_{In}^{I} + y_{Va}^{I} \ln y_{Va}^{I} + y_{Va^{-1}}^{I} \ln y_{Va^{-1}}^{I}) \\
& + \mathrm{RT}(y_{Cu}^{II} \ln y_{Cu}^{II} + y_{In}^{II} \ln y_{In}^{II}) \\
& + \mathrm{RT}(y_{Se}^{III} \ln y_{Se}^{III} + y_{Va}^{III} \ln y_{Va}^{III} + y_{Va^{+2}}^{III} \ln y_{Va^{+2}}^{III})
\end{aligned}
$$

$$(5.6)$$

and finding the excess Gibbs energy of mixing

$$EX_G{}^\alpha = y_{Cu}^I y_{In}^I \left[\begin{array}{l} y_{Cu}^{II} y_{Se}^{III}\left({}^0L^\alpha_{Cu,In:Cu:Se:Va:Va}\right) + y_{In}^{II} y_{Se}^{III}\left({}^0L^\alpha_{Cu,In:In:Se:Va:Va}\right) \\ + y_{Cu}^{II} y_{Va}^{III}\left({}^0L^\alpha_{Cu,In:Cu:Va:Va:Va}\right) + y_{In}^{II} y_{Va}^{III}\left({}^0L^\alpha_{Cu,In:In:Va:Va:Va}\right) \end{array} \right]$$

$$+ y_{Cu}^I y_{Va}^I \left[\begin{array}{l} y_{Cu}^{II} y_{Se}^{III}\left({}^0L^\alpha_{Cu,Va:Cu:Se:Va:Va}\right) + y_{In}^{II} y_{Se}^{III}\left({}^0L^\alpha_{Cu,Va:In:Se:Va:Va}\right) \\ + y_{Cu}^{II} y_{Va}^{III}\left({}^0L^\alpha_{Cu,Va:Cu:Va:Va:Va}\right) + y_{In}^{II} y_{Va}^{III}\left({}^0L^\alpha_{Cu,Va:In:Va:Va:Va}\right) \end{array} \right]$$

$$+ y_{Cu}^I y_{Va^{-1}}^I \left[\begin{array}{l} y_{Cu}^{II} y_{Se}^{III}\left({}^0L^\alpha_{Cu,Va^{-1}:Cu:Se:Va:Va}\right) + y_{In}^{II} y_{Se}^{III}\left({}^0L^\alpha_{Cu,Va^{-1}:In:Se:Va:Va}\right) \\ + y_{Cu}^{II} y_{Va}^{III}\left({}^0L^\alpha_{Cu,Va^{-1}:Cu:Va:Va:Va}\right) + y_{In}^{II} y_{Va}^{III}\left({}^0L^\alpha_{Cu,Va^{-1}:In:Va:Va:Va}\right) \end{array} \right]$$

$$+ y_{Cu}^I y_{In}^{II} \left[\begin{array}{l} y_{Cu}^{III} y_{Se}^{III}\left({}^0L^\alpha_{Cu:Cu,In:Se:Va:Va}\right) + y_{In}^{II} y_{Se}^{III}\left({}^0L^\alpha_{In:Cu,In:Se:Va:Va}\right) \\ + y_{Cu}^{II} y_{Va}^{III}\left({}^0L^\alpha_{Cu:Cu,In:Va:Va:Va}\right) + y_{In}^{II} y_{Va}^{III}\left({}^0L^\alpha_{In:Cu,In:Va:Va:Va}\right) \\ + y_{Va}^{II} y_{Se}^{III}\left({}^0L^\alpha_{Va:Cu,In:Se:Va:Va}\right) + y_{Va}^{II} y_{Va}^{III}\left({}^0L^\alpha_{Va:Cu,In:Va:Va:Va}\right) \end{array} \right]$$

$$+ y_{Va}^{III} y_{Se}^{III} \left[\begin{array}{l} y_{Cu}^I y_{Cu}^{II}\left({}^0L^\alpha_{Cu:Cu:Se,Va:Va:Va}\right) + y_{In}^I y_{Cu}^{II}\left({}^0L^\alpha_{In:Cu:Se,Va:Va:Va}\right) \\ + y_{Cu}^I y_{In}^{II}\left({}^0L^\alpha_{Cu:In:Se,Va:Va:Va}\right) + y_{In}^I y_{In}^{II}\left({}^0L^\alpha_{In:In:Se,Va:Va:Va}\right) \\ + y_{Va}^I y_{Cu}^{II}\left({}^0L^\alpha_{Va:Cu:Se,Va}\right) + y_{Va}^I y_{In}^{II}\left({}^0L^\alpha_{Va:In:Se,Va:Va:Va}\right) \end{array} \right]$$

$$+ y_{Va^{*2}}^{III} y_{Se}^{III} \left[\begin{array}{l} y_{Cu}^I y_{Cu}^{II}\left({}^0L^\alpha_{Cu:Cu:Se,Va^{*2}:Va:Va}\right) + y_{In}^I y_{Cu}^{II}\left({}^0L^\alpha_{In:Cu:Se,Va^{*2}:Va:Va}\right) \\ + y_{Cu}^I y_{In}^{II}\left({}^0L^\alpha_{Cu:In:Se,Va:Va:Va}\right) + y_{In}^I y_{In}^{II}\left({}^0L^\alpha_{In:In:Se,Va^{*2}}\right) \\ + y_{Va}^I y_{Cu}^{II}\left({}^0L^\alpha_{Va:Cu:Se,Va^{*2}:Va:Va}\right) + y_{Va}^I y_{In}^{II}\left({}^0L^\alpha_{Va:In:Se,Va^{*2}:Va:Va}\right) \end{array} \right]$$

(5.7)

where y_i^I, y_i^{II} and y_i^{III} are site fractions on the first three sublattices. $^\circ G$ is the Gibbs energy of a real or fictitious compound. They are called end-members and there are 24 of them as listed in the above equations. The ^0L parameters are the interaction parameter between the end members.

- The Gibbs energy of defect-free CuInSe$_2$, $^0G^\alpha_{Cu:In:Se:Va:Va}$, can be obtained from the previous section.

- The Gibbs energy of end-members, which have one defect,

$$(^0G^\alpha_{Cu:Cu:Se:Va:Va}, {}^0G^\alpha_{Va:In:Se:Va:Va}, {}^0G^\alpha_{In:In:Se:Va:Va}, {}^0G^\alpha_{Cu:In:Va:Va:Va}$$

$$, {}^0G^\alpha_{Va^{-1}:In:Se:Va:Va}, {}^0G^\alpha_{Cu:In:Va^{+2}:Va:Va}, \text{etc}) \text{ is obtained from defect formation}$$

energy and entropy calculation in the literature as listed in Table 2-4. The results listed in this table are based on the deviation from that of the same quantity of non-defective CIS.

- For the end-members which have two defects, a simple reciprocal relation [51] is used to obtain its Gibbs energy.

$$^0G^\alpha_{Va:Cu:Se:Va:Va} = {}^0G^\alpha_{Cu:Cu:Se:Va:Va} + {}^0G^\alpha_{Va:In:Se:Va:Va} - {}^0G^\alpha_{Cu:In:Se:Va:Va}$$

$$^0G^\alpha_{Va^{-1}:Cu:Se:Va:Va} = {}^0G^\alpha_{Cu:Cu:Se:Va:Va} + {}^0G^\alpha_{Va^{-1}:In:Se:Va:Va} - {}^0G^\alpha_{Cu:In:Se:Va:Va}$$

$$^0G^\alpha_{In:Cu:Se:Va:Va} = {}^0G^\alpha_{Cu:Cu:Se:Va:Va} + {}^0G^\alpha_{In:In:Se:Va:Va} - {}^0G^\alpha_{Cu:In:Se:Va:Va}$$

$$^0G^\alpha_{Va:In:Va:Va:Va} = {}^0G^\alpha_{Cu:In:Va:Va:Va} + {}^0G^\alpha_{Va:In:Se:Va:Va} - {}^0G^\alpha_{Cu:In:Se:Va:Va}$$

$$^0G^\alpha_{Va^{-1}:In:Va:Va:Va} = {}^0G^\alpha_{Cu:In:Va:Va:Va} + {}^0G^\alpha_{Va^{-1}:In:Se:Va:Va} - {}^0G^\alpha_{Cu:In:Se:Va:Va}$$

$$^0G^\alpha_{In:In:Va:Va:Va} = {}^0G^\alpha_{Cu:In:Va:Va:Va} + {}^0G^\alpha_{In:In:Se:Va:Va} - {}^0G^\alpha_{Cu:In:Se:Va:Va}$$

$$^0G^\alpha_{Va:In:Va^{+2}:Va:Va} = {}^0G^\alpha_{Cu:In:Va^{+2}:Va:Va} + {}^0G^\alpha_{Va:In:Se:Va:Va} - {}^0G^\alpha_{Cu:In:Se:Va:Va}$$

$$^0G^\alpha_{Va^{-1}:In:Va^{+2}:Va:Va} = {}^0G^\alpha_{Cu:In:Va^{+2}:Va:Va} + {}^0G^\alpha_{Va^{-1}:In:Se:Va:Va} - {}^0G^\alpha_{Cu:In:Se:Va:Va}$$

$${}^0G^\alpha_{In:In:Va^{+2}:Va:Va} = {}^0G^\alpha_{Cu:In:Va^{+2}:Va:Va} + {}^0G^\alpha_{In:In:Se:Va:Va} - {}^0G^\alpha_{Cu:In:Se:Va:Va}$$

$${}^0G^\alpha_{Cu:Cu:Va:Va:Va} = {}^0G^\alpha_{Cu:Cu:Se:Va:Va} + {}^0G^\alpha_{Cu:In:Va:Va:Va} - {}^0G^\alpha_{Cu:In:Se:Va:Va}$$

$${}^0G^\alpha_{Cu:Cu:Va^{+2}:Va:Va} = {}^0G^\alpha_{Cu:Cu:Se:Va:Va} + {}^0G^\alpha_{Cu:In:Va^{+2}:Va:Va} - {}^0G^\alpha_{Cu:In:Se:Va:Va}$$

$$(5.8)$$

- The Gibbs energy of end-members, which have three or more than three defects are simply put to an arbitrarily large value, for example 0 [51].

- The interaction parameter ${}^\alpha L^0$ are assumed to follow relations to reduce the parameters:

$$
\begin{aligned}
{}^\alpha L^0_{Cu,In:*:*:Va:Va} &= {}^\alpha L^0_{Cu,In:In:Se:Va:Va} = {}^\alpha L^0_{Cu,In:Cu:Se:Va:Va} = {}^\alpha L^0_{Cu,In:In:Va:Va:Va} \\
&= {}^\alpha L^0_{Cu,In:Cu:Va:Va:Va} = {}^\alpha L^0_{Cu,In:In:Va^{+2}:Va:Va} = {}^\alpha L^0_{Cu,In:Cu:Va^{+2}:Va:Va} \\[4pt]
{}^\alpha L^0_{Cu,Va:*:*:Va:Va} &= {}^\alpha L^0_{Cu,Va:In:Se:Va:Va} = {}^\alpha L^0_{Cu,Va:Cu:Se:Va:Va} = {}^\alpha L^0_{Cu,Va:In:Va:Va:Va} \\
&= {}^\alpha L^0_{Cu,Va:Cu:Va:Va:Va} = {}^\alpha L^0_{Cu,Va:In:Va^{+2}:Va:Va} = {}^\alpha L^0_{Cu,Va:Cu:Va^{+2}:Va:Va} \\[4pt]
{}^\alpha L^0_{*:Cu,In:*:Va:Va} &= {}^\alpha L^0_{Cu:Cu,In:Se:Va:Va} = {}^\alpha L^0_{In:Cu,In:Se:Va:Va} = {}^\alpha L^0_{In:Cu,In:Va:Va:Va} \\
&= {}^\alpha L^0_{Cu:Cu,In:Va:Va:Va} = {}^\alpha L^0_{Cu:Cu,In:Va^{+2}:Va:Va} = {}^\alpha L^0_{Cu:Cu,In:Va^{+2}:Va:Va} \\
&= {}^\alpha L^0_{Va:Cu,In:Se:Va:Va} = {}^\alpha L^0_{Va:Cu,In:Va:Va:Va} = {}^\alpha L^0_{Va:Cu,In:Va^{+2}:Va:Va} \\[4pt]
{}^\alpha L^0_{*:*:Se,Va:Va:Va} &= {}^\alpha L^0_{Cu:Cu:Se,Va:Va:Va} = {}^\alpha L^0_{In:Cu:Se,Va:Va:Va} = {}^\alpha L^0_{Va:Cu:Se,Va:Va:Va} \\
&= {}^\alpha L^0_{Cu:In:Se,Va:Va:Va} = {}^\alpha L^0_{In:In:Se,Va:Va:Va} = {}^\alpha L^0_{Va:In:Se,Va:Va:Va} \\[4pt]
{}^\alpha L^0_{*:*:Se,Va^{+2}:Va:Va} &= {}^\alpha L^0_{Cu:Cu:Se,Va^{+2}:Va:Va} = {}^\alpha L^0_{In:Cu:Se,Va^{+2}:Va:Va} = {}^\alpha L^0_{Va:Cu:Se,Va^{+2}:Va:Va} \\
&= {}^\alpha L^0_{Cu:In:Se,Va^{+2}:Va:Va} = {}^\alpha L^0_{In:In:Se,Va^{+2}:Va:Va} = {}^\alpha L^0_{Va:In:Se,Va^{+2}:Va:Va}
\end{aligned}
$$

$$(5.9)$$

II. β_R-CIS ($Cu_1In_3Se_5$), γ-CIS($Cu_1In_5Se_8$), and β_H-CIS($Cu_2In_4Se_7$)

Similar to the modeling the non-stoichiometric α-CIS (CuInSe$_2$) phase, a three sublattice model was also used to describe these compounds. Since the electrons and holes are not modeled in these CIS phases, sublattices IV and V are not added.

For β_R-CIS (Cu$_1$In$_3$Se$_5$) phase:

$$(\textbf{Cu, Va, In})^I_1 (\textbf{In, Cu})^{II}_3 (\textbf{Se, Va})^{III}_5$$
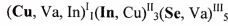
For γ - CIS(Cu$_1$In$_5$Se$_8$) phase: $(\textbf{Cu, Va, In})^I_1 (\textbf{In, Cu})^{II}_5 (\textbf{Se, Va})^{III}_8$

For β_H-CIS(Cu$_2$In$_4$Se$_7$) phase : $(\textbf{Cu, Va, In})^I_2 (\textbf{In, Cu})^{II}_4 (\textbf{Se, Va})^{III}_7$

As mentioned previously, these ODC compounds are formed by repeating periodically m

units of $2V_{Cu}^{-1} + In_{Cu}^{+2}$ for every n unit of α-CIS (CuInSe$_2$) [31-32]. The Gibbs energy for

these compounds can also be expressed in the similar way as α-CIS (CuInSe$_2$). The

value of Gibbs energy of the end-members of one or two defects in these compounds in

relation to the Gibbs energy of the end-members of α-CIS (CuInSe$_2$) can be set by the

following expression:

$$^0G^{\beta_R}_{i\,:\,j\,:\,k\,:\,Va\,:\,Va} = 2.5 \times {}^0G^{\alpha}_{i\,:\,j\,:\,k\,:\,Va\,:\,Va}, \quad {}^0G^{\beta_H}_{i\,:\,j\,:\,k\,:\,Va\,:\,Va} = 3.5 \times {}^0G^{\alpha}_{i\,:\,j\,:\,k\,:\,Va\,:\,Va},$$

$$^0G^{\gamma}_{i\,:\,j\,:\,k\,:\,Va\,:\,Va} = 4 \times {}^0G^{\alpha}_{i\,:\,j\,:\,k\,:\,Va\,:\,Va} \tag{5.10}$$

where i, j, and k represent the various sublattice constituents. For example,

$$^0G^{\beta_R}_{Cu\,:\,Cu\,:\,Se\,:\,Va} = 2.5 \times {}^0G^{\alpha}_{Cu\,:\,Cu\,:\,Se\,:\,Va\,:\,Va}.$$

5.3.2 Calculation of the Carrier Concentration in α-CIS (CuInSe$_2$)

The free electrons and holes concentration can be calculated if they are also

included in the thermodynamic description. They are supposed to be distributed on

different numbers of sites than there are sites in the sublattices [52]. As known from the

Fermi-Dirac distribution function for electrons in the conduction band and holes in the

valence band N_c and N_v stand for the effective density of the conduction and valence

band states, respectively. So, let N_c and N_v be the number of sites that electrons and holes can occupy per formula unit.

According to the above description, the α-CIS phase can be described by the following sublattices.

$$(\mathbf{Cu}, Va, Va^{-1}, In)^I_1 (\mathbf{In}, Cu)^{II}_1 (\mathbf{Se}, Va, Va^{+2})^{III}_2 (\mathbf{Va}, e^{-1})^{IV}_{Nc} (\mathbf{Va}, h^{+1})^V_{Nv}$$
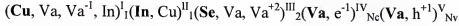
This model can be directly described with the Compound Energy Model (CEM). However, CEM requires N_c and N_v to be constant. Chen *et al.* [51] provided an alternative way to solve this problem and transferred the sublattice description to the following:

$$(\mathbf{Cu}, Va, In)^I_1 (\mathbf{In}, Va, Cu)^{II}_1 (\mathbf{Se}, Va, Va^{+2})^{III}_2 (\mathbf{Va}, e^{-1})^{IV}_1 (\mathbf{Va}, h^{+1})^V_1$$
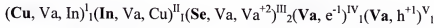
Here is briefly described their transformation methodology by applying it to the α-CIS phase. The effect of adding the IV sublattice for electrons is, instead of having the term, $y^I_* y^{II}_* y^{III}_* G^0_{*,*,*}$, the equation

$$y^I_* y^{II}_* y^{III}_* y^{IV}_{Va} G^0_{*,*,*,Va} + y^I_* y^{II}_* y^{III}_* y^{IV}_{e^{-1}} G^0_{*,*,*,e^{-1}} = y^I_* y^{II}_* y^{III}_* (1 - y^{IV}_{e^{-1}}) G^0_{*,*,*,Va} + y^I_* y^{II}_* y^{III}_* y^{IV}_{e^{-1}} G^0_{*,*,*,e^{-1}}$$
$$= y^I_* y^{II}_* y^{III}_* G^0_{*,*,*,Va} + (G^0_{*,*,*,e^{-1}} - G^0_{*,*,*,Va}) y^I_* y^{II}_* y^{III}_* y^{IV}_{e^{-1}}$$

$$(y^{IV}_{Va} + y^{IV}_{e^{-1}} = 1) \tag{5.11}$$

For simplicity, it is assumed all values $(G^0_{*,*,*,e^{-1}} - G^0_{*,*,*,Va})$ are equal. However, the quantities refer to N_c moles of electron. Denote the electron chemical potential as

$$\Delta G^0_{e^{-1}} \, \text{-} G^{0,ref} \quad = \quad (G^0_{*,*,*,e^{-1}} - G^0_{*,*,*,Va})/ N_c \tag{5.12}$$

The $G^{0,ref}$ can be immediately omitted due to the condition of electroneutrality. It will drop out of the final expression for G if the same reference is used for all charged constituents. Substituting equation (5.12) into equation (5.11) yields

$$N_c = 2(2\pi m_c^* kT / h^2)^{3/2} \bullet (a^2c/8)$$
$$N_v = 2(2\pi m_v^* kT / h^2)^{3/2} \bullet (a^2c/8)$$

(5.16)

$(a^2c/8)$ is the volume per mole of the formula units and is added to get the densities

counted per mole of formula units. m_c^* and m_v^* are the effective masses of electrons at the

conduction band edge and holes at the valence band edge, respectively. k is Boltzman's

constant, and h is Planck's constant. The values of all the parameters are summarized in

Table 5-3 [53-54].

5.3.3 Results and Conclusions

A reasonable agreement for the α-CIS phase was obtained between the model-

calculated values and the phase equilibrium available in the literature as shown in Figure

5-2. The optimized parameters are listed in the Table 5-6. The calculated defect and

carrier concentration data is shown in Figure 5-3.

Further work needs to be done to get better agreement of phase equilibrium for all

the phases.
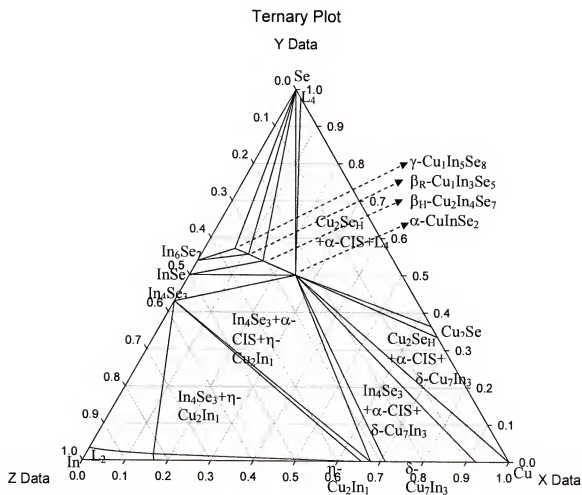
Figure 5-1. Simulation results of defect free Cu-In-Se system.
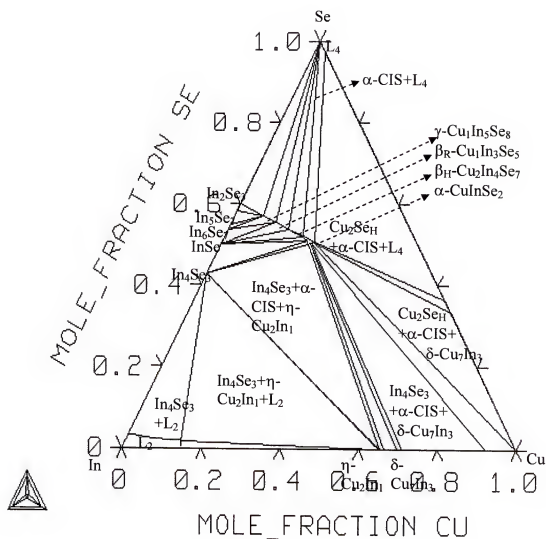
Figure 5-2. Predicted phase diagram of the Cu-In-Se system at 773 K that indicates non stoichiometric CuInSe₂.
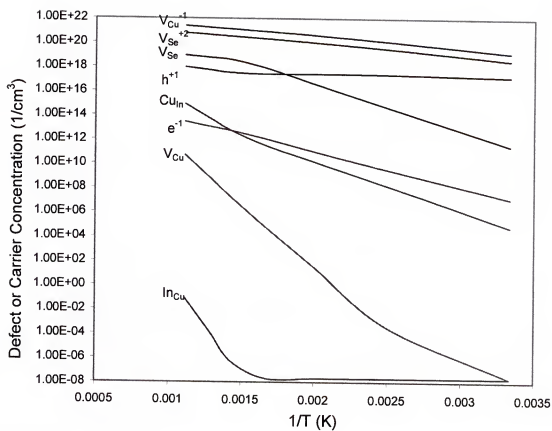
Figure 5-3. Calculated defect and carrier concentration at the α-CIS/β-Cu₂Se phase boundary.

Table 5-1. Experimental compositions in the Cu-In-Se system at 773K [38].

Phases	Composition, at. % Se	Composition, at. % Cu
α-CIS/β_R-CIS/IONIC_LIQ	0.5294/0.553/0.9852	0.1963/0.149/0.00142
IONIC_LIQ/α-CIS	0.5234/0.9904 0.5195/0.9926 0.5141/0.99285	0.2052/0.001896 0.2152/0.001942 0.2250/0.003625
α-CIS /β-Cu$_2$Se /IONIC_LIQ	0.5096/0.3794/0.994	0.2354/0.6157/0.00592
α-CIS /β-Cu$_2$Se /CU_FCC	0.5017/0.33646/0.0054	0.23895/0.6562/0.9061
α-CIS /CU_FCC	0.5003/0/0.00296	0.2371/0.7/0.904
α-CIS /δ (Cu$_7$Se$_3$) /η(Cu$_2$In$_1$)	0.4988/0/0.0064	0.2353/0.7/0.6388
α-CIS / IN$_4$SE$_3$/η(Cu$_2$In$_1$)	0.4983/0.4286/0.001	0.2326/0/0.6225
α-CIS /IN$_1$SE$_1$_A/IN$_4$SE$_3$	0.5012/0.5/0.4286	0.2278/0/0
α-CIS / IN$_1$SE$_1$_A/β_H-CIS	0.5052/0.5/0.5141	0.22156/0/0.1388
α-CIS /β_R-CIS /β_H-CIS	0.5101/0.52795/0.523	0.2123/0.1649/0.161
IONIC_LIQ/γ- In$_2$Se$_3$/γ-CIS	0.961/0.6/0.5942	0/0/0.0332
IONIC_LIQ/γ-CIS /β_R-CIS	0.978/0.5932/0.589	0.02/0.0557/0.095
In6Se7/γ-CIS//β_R-CIS	0.538/0.5675/0.5537	0/0/0.0592/0.088
In6Se7/γ-CIS// In$_9$Se$_{11}$	0.538/0.5720/0.55	0/0.052/0
In$_5$Se$_7$/γ-CIS/ In$_9$Se$_{11}$	0.5933/0.5744/0.55	0/0.0465/0
In$_5$Se$_7$/γ-CIS/β-In$_2$Se$_3$	0.5933/0.5819/0.6	0/0.0368/0

Table 5-2. Summary of the Optimized Parameters

Phases and Functions	Parameters
α-CIS (CuInSe$_2$)	$^0G_C^\alpha{}_{Cu\,:\,In\,:\,Se\,:\,Va}$ = CIS_A
β$_R$-CIS (Cu$_1$In$_3$Se$_5$)	$^0G_C^{\beta_R}{}_{Cu\,:\,In\,:\,Se\,:\,Va}$ = 2.5×CIS_A+V$_1$
β$_H$-CIS (Cu$_2$In$_4$Se$_7$)	$^0G_C^{\beta_H}{}_{Cu\,:\,In\,:\,Se\,:\,Va}$ = 3.5×CIS_A+V$_2$
γ-CIS (Cu$_1$In$_5$Se$_8$)	$^0G_C^\gamma{}_{Cu\,:\,In\,:\,Se\,:\,Va}$ = 4×CIS_A+V$_3$
η (Cu$_2$In$_1$)	In addition to all the parameters from Cu-In binary system [50], the following ternary interaction parameters are added: $^\eta L^0_{Cu,In,Se*}$ =-1029637 $^\eta L^0_{*,Cu,In,Se}$ = -1029637
β-Cu$_2$Se	In addition to all the parameters from Cu-Se binary system [44], the following ternary interaction parameter is added: $^{\beta-Cu_2Se}L^0_{Cu,In,Va:Se:Cu}$ =-20000
δ (Cu$_7$In$_3$)	In addition to all the parameters from Cu-In binary system [50], the following ternary interaction parameters are added $^\delta L^0_{Cu,In,Se}$ =-90000 $^\delta L^0_{*,Cu,In,Se}$ =-90000
Fcc (Cu)	In addition to all the parameters from Cu-In and Cu-Se binary system[44, 50], the following ternary interaction parameter is added $^{CuFcc}L^0_{Cu,In,Se}$=-90000
Ionic_Liq	In addition to all the parameters from Cu-In In-Se and Cu-Se binary[1,2] system, the following ternary interaction parameters are added: $^{Ionic\_Liq}L^0_{Cu^{+1},Cu^{+2},In^{+3}:Se^{-2}}$ =-46015; $^{Ionic\_Liq}L^1_{Cu^{+1},Cu^{+2},In^{+3}:Se^{-2}}$ =9015

Functions	CIS_A=GCUFCC+2×GSE_S+GIN_S-226835
	GCUFCC= -7770.45775+130.485222T-24.11239Tln(T)
	  -.00265684T^2+1.29222833E-07T^3+52477.8T^{-1} (298 ~1368 K)
	  = -13309.7197+183.649837T-31.38TLN(T) (1358~3200)
	GIN_S= -6978.89011+92.3381153T-21.8386Tln(T)
	  -.00572566T^2-2.12032167E-06T^3-22906T^{-1} (298~430 K)
	  = -7032.8091+124.475108T-27.4562Tln(T)+5.4607E-04T^2
	  -8.36698333E-08T^3-211707.5T^{-1} (430~3800 K)
	GSE_S = -6657.653+92.539695T-19.14Tln(T)
	  -.012295T^2+2.6766666E-06T^3 (298~ 494 K)
	  = -6657.653+92.539695T-19.14Tln(T)-
	.012295T^2+2.6766666E-06T^3 (494~760K)
	  = -9059.16586+150.334216T-28.552Tln(T) (760~1500 K)
	V$_1$=44500 V$_2$=42500 V$_3$=99000
	Note: all the units are in J/mol.

Table 5-3. Summary of some of α-CIS property values.

Parameter	Value	Ref
a	5.782 Å	[54]
c	2.0097 a = 11.6201 Å	[54]
E_g	$0.965 - 1.086 \times 10^{-4} \, T^2/(T+97)$ (eV)	[56]
m_c^*	$0.091 \, m_0$	[56]
m_v^*	$0.091 \, m_0$ ($= 9.11 \times 10^{-31}$ kg)	[56]
k	8.617×10^{-5} eV/K	[56]
h	$6.63 \times 10^{-34} \, J \cdot S$	[56]
$N_c \approx N_v$	$6.34 \times 10^{-13} \, T^{3/2}$	[56]

Table 5-4. Summary of the optimized parameters for off-stoichiometry CIS.

Phases and Functions	Parameters
α-CIS ($CuInSe_2$)	$°G^{\alpha}_{Cu:In:Se:Va:Va} = $ CIS_A
	$°G^{\alpha}_{Va:In:Se:Va:Va} = $ VIS_A
	$°G^{\alpha}_{Va^{-1}:In:Se:Va:Va} = $ EIS_A
	$°G^{\alpha}_{In:In:Se:Va:Va} = $ IIS_A
	$°G^{\alpha}_{Cu:Cu:Se:Va:Va} = $ CS_A
	$°G^{\alpha}_{Cu:In:Va:Va:Va} = $ CIV_A
	$°G^{\alpha}_{Cu:In:Va^{+2}:Va:Va} = $ CIH_A
	$°G^{\alpha}_{Va:Cu:Se:Va:Va} = $ CCS_A+VIS_A-CIS_A
	$°G^{\alpha}_{Va^{-1}:Cu:Se:Va:Va} = $ CCS_A+EIS_A-CIS_A
	$°G^{\alpha}_{In:Cu:Se:Va:Va} = $ CCS_A+IIS_A-CIS_A
	$°G^{\alpha}_{Va:In:Va:Va:Va} = $ VIS_A+CIV_A-CIS_A
	$°G^{\alpha}_{Va^{-1}:In:Va:Va:Va} = $ EIS_A+CIV_A-CIS_A
	$°G^{\alpha}_{In:In:Va:Va:Va} = $ IIS_A+CIV_A-CIS_A
	$°G^{\alpha}_{Va:In:Va^{+2}:Va:Va} = $ CIH_A+VIS_A-CIS_A
	$°G^{\alpha}_{Va^{-1}:In:Va^{+2}:Va:Va} = $ CIH_A+EIS_A-CIS_A
	$°G^{\alpha}_{In:In:Va^{+2}:Va:Va} = $ CIH_A+IIS_A-CIS_A
	$°G^{\alpha}_{Cu:Cu:Va:Va:Va} = $ CIV_A+CCS_A-CIS_A
	$°G^{\alpha}_{Cu:Cu:Va^{+2}:Va:Va} = $ CCS_A+CIH_A-CIS_A
	$°G^{\alpha}_{Cu:In:Se^{-1}:Va} = $ CIS_A+TEGN
	$°G^{\alpha}_{Va:In:Se^{-1}:Va} = $ VIS_A+TEGN
	$°G^{\alpha}_{Va^{-1}:In:Se^{-1}:Va} = $ EIS_A+TEGN
	$°G^{\alpha}_{In:In:Se^{-1}:Va} = $ IIS_A+TEGN

	$^0G^\alpha_{Cu:Cu:Se:Va^{-1}:Va}$ = CCS_A+TEGN
	$^0G^\alpha_{Cu:In:Va^{-1}:Va}$ = CIV_A+TEGN
	$^0G^\alpha_{Cu:In:Va^{+3}:Va^{-1}:Va}$ = CIH_A+TEGN
	$^0G^\alpha_{Cu:In:Se:Va^{+1}}$ = CIS_A+TEGH
	$^0G^\alpha_{Va:In:Se:Va^{+1}}$ = VIS_A+TEGH
	$^0G^\alpha_{Va^{-1}:In:Se:Va^{+1}}$ = EIS_A+TEGH
	$^0G^\alpha_{In:In:Se:Va^{+1}}$ = IIS_A+TEGH
	$^0G^\alpha_{Cu:Cu:Se:Va^{+1}}$ = CCS_A+TEGH
	$^0G^\alpha_{Cu:In:Va:Va^{+1}}$ = CIV_A+TEGH
	$^0G^\alpha_{Cu:In:Va^{+2}:Va:Va^{+1}}$ = CIH_A+TEGH
	$^0G^\alpha_{Cu:In:Se:Va^{-1}:Va^{+1}}$ = CIS_A+TEGH+TEGN
	$^\alpha L^0_{Cu,In:*:*:Va:Va}$ = LCI
	$^\alpha L^0_{Cu,Va:*:*:Va:Va}$ = LCV
	$^\alpha L^0_{Cu,Va^{-1}:*:*:Va:Va}$ = LCE
	$^\alpha L^0_{*:Cu,In:*:Va:Va}$ = LIC
	$^\alpha L^0_{*:*:Se,Va:Va:Va}$ = LSV
	$^\alpha L^0_{*:*:Se,Va^{+2}:Va:Va}$ = LSH
β_R-CIS $(Cu_1In_3Se_5)$	$^0G^{\beta_R}_{Cu:In:Se:Va:Va}$ = 2.5×CIS_A+44500
	$^0G^{\beta_R}_{Cu:Cu:Se:Va:Va}$ = 2.5×CCS_A
	$^0G^{\beta_R}_{Va:In:Se:Va:Va}$ = 2.5×VIS_A
	$^0G^{\beta_R}_{In:In:Se:Va:Va}$ = 2.5×IIS_A
	$^0G^{\beta_R}_{Cu:In:Va:Va:Va}$ = 2.5×CIV_A
	$^0G^{\beta_R}_{Va^{-1}:In:Se:Va:Va}$ = 2.5×EIS_A
	$^0G^{\beta_R}_{Cu:In:Va^{+2}:Va:Va}$ = 2.5×CIH_A
	$^0G^{\beta_R}_{Va:Cu:Se:Va:Va}$ = 2.5×CCS_A+2.5×VIS_A-2.5×CIS_A

$${}^{o}G^{\beta_R}_{Va^{-1}\,:\,Cu\,:\,Va\,:\,Va} = 2.5\times CCS\_A + 2.5\times EIS\_A - 2.5\times CIS\_A$$

$${}^{o}G^{\beta_R}_{In\,:\,Cu\,:\,Se\,:\,Va\,:\,Va} = 2.5\times CCS\_A + 2.5\times IIS\_A - 2.5\times CIS\_A$$

$${}^{o}G^{\beta_R}_{Va\,:\,In\,:\,Va\,:\,Va} = 2.5\times VIS\_A + 2.5\times CIV\_A - 2.5\times CIS\_A$$

$${}^{o}G^{\beta_R}_{Va^{-1}\,:\,In\,:\,Va\,:\,Va} = 2.5\times EIS\_A + 2.5\times CIV\_A - 2.5\times CIS\_A$$

$${}^{o}G^{\beta_R}_{In\,:\,Va\,:\,Va\,:\,Va} = 2.5\times IIS\_A + 2.5\times CIV\_A - 2.5\times CIS\_A$$

$${}^{o}G^{\beta_R}_{Va\,:\,In\,:\,Va^{+2}\,:\,Va\,:\,Va} = 2.5\times CIH\_A + 2.5\times VIS\_A - 2.5\times CIS\_A$$

$${}^{o}G^{\beta_R}_{Va^{-1}\,:\,In\,:\,Va^{+2}\,:\,Va\,:\,Va} = 2.5\times CIH\_A + 2.5\times EIS\_A - 2.5\times CIS\_A$$

$${}^{o}G^{\beta_R}_{In\,:\,In\,:\,Va^{+2}\,:\,Va\,:\,Va} = 2.5\times CIH\_A + 2.5\times IIS\_A - 2.5\times CIS\_A$$

$${}^{o}G^{\beta_R}_{Cu\,:\,Cu\,:\,Va\,:\,Va} = 2.5\times CIV\_A + 2.5\times CCS\_A - 2.5\times CIS\_A$$

$${}^{o}G^{\beta_R}_{Cu\,:\,Cu\,:\,Va^{+2}\,:\,Va\,:\,Va} = 2.5\times CCS\_A + 2.5\times CIH\_A - 2.5\times CIS\_A$$

$${}^{o}G^{\beta_R}_{Cu\,:\,In\,:\,Se\,:\,Va^{-1}\,:\,Va} = 2.5\times CIS\_A + TEGN$$

$${}^{o}G^{\beta_R}_{Va\,:\,In\,:\,Se\,:\,Va^{-1}\,:\,Va} = 2.5\times VIS\_A + TEGN$$

$${}^{o}G^{\beta_R}_{Va^{-1}\,:\,In\,:\,Se\,:\,Va^{-1}\,:\,Va} = 2.5\times EIS\_A + TEGN$$

$${}^{o}G^{\beta_R}_{In\,:\,In\,:\,Se\,:\,Va^{-1}\,:\,Va} = 2.5\times IIS\_A + TEGN$$

$${}^{o}G^{\beta_R}_{Cu\,:\,Cu\,:\,Se\,:\,Va^{-1}\,:\,Va} = 2.5\times CCS\_A + TEGN$$

$${}^{o}G^{\beta_R}_{Cu\,:\,In\,:\,Va\,:\,Va^{-1}\,:\,Va} = 2.5\times CIV\_A + TEGN$$

$${}^{o}G^{\beta_R}_{Cu\,:\,In\,:\,Va^{+2}\,:\,Va^{-1}\,:\,Va} = 2.5\times CIH\_A + TEGN$$

$${}^{o}G^{\beta_R}_{Cu\,:\,In\,:\,Se\,:\,Va\,:\,Va^{+1}} = 2.5\times CIS\_A + TEGH$$

$${}^{o}G^{\beta_R}_{Va\,:\,In\,:\,Se\,:\,Va\,:\,Va^{+1}} = 2.5\times VIS\_A + TEGH$$

$${}^{o}G^{\beta_R}_{Va^{-1}\,:\,In\,:\,Se\,:\,Va\,:\,Va^{+1}} = 2.5\times EIS\_A + TEGH$$

$${}^{o}G^{\beta_R}_{In\,:\,In\,:\,Se\,:\,Va\,:\,Va^{+1}} = 2.5\times IIS\_A + TEGH$$

$${}^{o}G^{\beta_R}_{Cu\,:\,Cu\,:\,Se\,:\,Va\,:\,Va^{+1}} = 2.5\times CCS\_A + TEGH$$

$${}^{o}G^{\beta_R}_{Cu\,:\,In\,:\,Va\,:\,Va^{+1}} = 2.5\times CIV\_A + TEGH$$

	$^oG^{\beta_R}_{Cu\,:\,In\,:\,Va^{+2}\,:\,Va^{+1}} = 2.5\times CIH\_A+TEGH$
	$^oG^{\beta_R}_{Cu\,:\,In\,:\,Se\,:\,Va^{-1}\,:\,Va^{+1}} = 2.5\times CIS\_A+TEGH+TEGN$
β_H-CIS ($Cu_2In_4Se_7$)	$^oG^{\beta_H}_{Cu\,:\,In\,:\,Se\,:\,Va\,:\,Va} = 3.5\times CIS\_A+44500$
	$^oG^{\beta_H}_{Cu\,:\,Cu\,:\,Se\,:\,Va\,:\,Va} = 3.5\times CCS\_A$
	$^oG^{\beta_H}_{Va\,:\,In\,:\,Se\,:\,Va\,:\,Va} = 3.5\times VIS\_A$
	$^oG^{\beta_H}_{In\,:\,In\,:\,Se\,:\,Va\,:\,Va} = 3.5\times IIS\_A$
	$^oG^{\beta_H}_{Cu\,:\,In\,:\,Va\,:\,Va\,:\,Va} = 3.5\times CIV\_A$
	$^oG^{\beta_H}_{Va^{-1}\,:\,In\,:\,Se\,:\,Va\,:\,Va} = 3.5\times EIS\_A$
	$^oG^{\beta_H}_{Cu\,:\,In\,:\,Va^{+2}\,:\,Va\,:\,Va} = 3.5\times CIH\_A$
	$^oG^{\beta_H}_{Va\,:\,Cu\,:\,Se\,:\,Va\,:\,Va} = 3.5\times CCS\_A+3.5\times VIS\_A-3.5\times CIS\_A$
	$^oG^{\beta_H}_{Va^{-1}\,:\,Cu\,:\,Se\,:\,Va\,:\,Va} = 3.5\times CCS\_A+3.5\times EIS\_A-3.5\times CIS\_A$
	$^oG^{\beta_H}_{In\,:\,Cu\,:\,Se\,:\,Va\,:\,Va} = 3.5\times CCS\_A+3.5\times IIS\_A-3.5\times CIS\_A$
	$^oG^{\beta_H}_{Va\,:\,In\,:\,Va\,:\,Va\,:\,Va} = 3.5\times VIS\_A+3.5\times CIV\_A-3.5\times CIS\_A$
	$^oG^{\beta_H}_{Va^{-1}\,:\,In\,:\,Va\,:\,Va\,:\,Va} = 3.5\times EIS\_A+3.5\times CIV\_A-3.5\times CIS\_A$
	$^oG^{\beta_H}_{In\,:\,In\,:\,Va\,:\,Va\,:\,Va} = 3.5\times IIS\_A+3.5\times CIV\_A-3.5\times CIS\_A$
	$^oG^{\beta_H}_{Va\,:\,In\,:\,Va^{+2}\,:\,Va\,:\,Va} = 3.5\times CIH\_A+3.5\times VIS\_A-3.5\times CIS\_A$
	$^oG^{\beta_H}_{Va^{-1}\,:\,In\,:\,Va^{+2}\,:\,Va\,:\,Va} = 3.5\times CIH\_A+3.5\times EIS\_A-3.5\times CIS\_A$
	$^oG^{\beta_H}_{In\,:\,In\,:\,Va^{+2}\,:\,Va\,:\,Va} = 3.5\times CIH\_A+3.5\times IIS\_A-3.5\times CIS\_A$
	$^oG^{\beta_H}_{Cu\,:\,Cu\,:\,Va\,:\,Va\,:\,Va} = 3.5\times CIV\_A+3.5\times CCS\_A-3.5\times CIS\_A$
	$^oG^{\beta_H}_{Cu\,:\,Cu\,:\,Va^{+2}\,:\,Va\,:\,Va} = 3.5\times CCS\_A+3.5\times CIH\_A-3.5\times CIS\_A$
	$^oG^{\beta_H}_{Cu\,:\,In\,:\,Se\,:\,Va^{-1}\,:\,Va} = 3.5\times CIS\_A+TEGN$
	$^oG^{\beta_H}_{Va\,:\,In\,:\,Se\,:\,Va^{-1}\,:\,Va} = 3.5\times VIS\_A+TEGN$

	$^oG\beta_H{}_{Va^{-1}:In:Se:Va^{-1}:Va}$ = 3.5×EIS_A+TEGN
	$^oG\beta_H{}_{In:In:Se:Va^{-1}:Va}$ = 3.5×IIS_A+TEGN
	$^oG\beta_H{}_{Cu:Cu:Se:Va^{-1}:Va}$ = 3.5×CCS_A+TEGN
	$^oG\beta_H{}_{Cu:In:Va:Va^{-1}:Va}$ = 3.5×CIV_A+TEGN
	$^oG\beta_H{}_{Cu:In:Va^{+2}:Va^{-1}:Va}$ = 3.5×CIH_A+TEGN
	$^oG\beta_H{}_{Cu:In:Se:Va:Va^{+1}}$ = 3.5×CIS_A+TEGH
	$^oG\beta_H{}_{Va:In:Se:Va:Va^{+1}}$ = 3.5×VIS_A+TEGH
	$^oG\beta_H{}_{Va^{-1}:In:Se:Va:Va^{+1}}$ =3.5×EIS_A+TEGH
	$^oG\beta_H{}_{In:In:Se:Va:Va^{+1}}$ = 3.5×IIS_A+TEGH
	$^oG\beta_H{}_{Cu:Cu:Se:Va:Va^{+1}}$ = 3.5×CCS_A+TEGH
	$^oG\beta_H{}_{Cu:In:Va:Va:Va^{+1}}$ = 3.5×CIV_A+TEGH
	$^oG\beta_H{}_{Cu:In:Va^{+2}:Va:Va^{+1}}$ = 3.5×CIH_A+TEGH
	$^oG\beta_H{}_{Cu:In:Se:Va^{-1}:Va^{+1}}$ = 3.5×CIS_A+TEGH+TEGN
γ-CIS (Cu₁In₅Se₈)	$^oG^\gamma{}_{Cu:In:Se:Va:Va}$ = 4×CIS_A+44500
	$^oG^\gamma{}_{Cu:Cu:Se:Va:Va}$ = 4×CCS_A
	$^oG^\gamma{}_{Va:In:Se:Va:Va}$ = 4×VIS_A
	$^oG^\gamma{}_{In:In:Se:Va:Va}$ = 4×IIS_A
	$^oG^\gamma{}_{Cu:In:Va:Va:Va}$ = 4×CIV_A
	$^oG^\gamma{}_{Va^{-1}:In:Se:Va:Va}$ = 4×EIS_A
	$^oG^\gamma{}_{Cu:In:Va^{+3}:Va:Va}$ = 4×CIH_A
	$^oG^\gamma{}_{Va:Cu:Se:Va:Va}$ = 4×CCS_A+4×VIS_A-4×CIS_A
	$^oG^\gamma{}_{Va^{-1}:Cu:Se:Va:Va}$ = 4×CCS_A+4×EIS_A-4×CIS_A
	$^oG^\gamma{}_{In:Cu:Se:Va:Va}$ = 4×CCS_A+4×IIS_A-4×CIS_A

$${}^{0}G^{\gamma}_{Va\,:\,In\,:\,Va\,:\,Va} = 4\times VIS\_A + 4\times CIV\_A - 4\times CIS\_A$$

$${}^{0}G^{\gamma}_{Va^{-1}\,:\,In\,:\,Va\,:\,Va} = 4\times EIS\_A + 4\times CIV\_A - 4\times CIS\_A$$

$${}^{0}G^{\gamma}_{In\,:\,In\,:\,Va\,:\,Va} = 4\times IIS\_A + 4\times CIV\_A - 4\times CIS\_A$$

$${}^{0}G^{\gamma}_{Va\,:\,In\,:\,Va^{+2}\,:\,Va\,:\,Va} = 4\times CIH\_A + 4\times VIS\_A - 4\times CIS\_A$$

$${}^{0}G^{\gamma}_{Va^{-1}\,:\,In\,:\,Va^{+2}\,:\,Va\,:\,Va} = 4\times CIH\_A + 4\times EIS\_A - 4\times CIS\_A$$

$${}^{0}G^{\gamma}_{In\,:\,In\,:\,Va^{+2}\,:\,Va\,:\,Va} = 4\times CIH\_A + 4\times IIS\_A - 4\times CIS\_A$$

$${}^{0}G^{\gamma}_{Cu\,:\,Cu\,:\,Va\,:\,Va} = 4\times CIV\_A + 4\times CCS\_A - 4\times CIS\_A$$

$${}^{0}G^{\gamma}_{Cu\,:\,Cu\,:\,Va^{+2}\,:\,Va\,:\,Va} = 4\times CCS\_A + 4\times CIH\_A - 4\times CIS\_A$$

$${}^{0}G^{\gamma}_{Cu\,:\,In\,:\,Se\,:\,Va^{-1}\,:\,Va} = 4\times CIS\_A + TEGN$$

$${}^{0}G^{\gamma}_{Va\,:\,In\,:\,Se\,:\,Va^{-1}\,:\,Va} = 4\times VIS\_A + TEGN$$

$${}^{0}G^{\gamma}_{Va^{-1}\,:\,In\,:\,Se\,:\,Va^{-1}\,:\,Va} = 4\times EIS\_A + TEGN$$

$${}^{0}G^{\gamma}_{In\,:\,In\,:\,Se\,:\,Va^{-1}\,:\,Va} = 4\times IIS\_A + TEGN$$

$${}^{0}G^{\gamma}_{Cu\,:\,Cu\,:\,Se\,:\,Va^{-1}\,:\,Va} = 4\times CCS\_A + TEGN$$

$${}^{0}G^{\gamma}_{Cu\,:\,In\,:\,Va\,:\,Va^{-1}\,:\,Va} = 4\times CIV\_A + TEGN$$

$${}^{0}G^{\gamma}_{Cu\,:\,In\,:\,Va^{+2}\,:\,Va^{-1}\,:\,Va} = 4\times CIH\_A + TEGN$$

$${}^{0}G^{\gamma}_{Cu\,:\,In\,:\,Se\,:\,Va^{+1}} = 4\times CIS\_A + TEGH$$

$${}^{0}G^{\gamma}_{Va\,:\,In\,:\,Se\,:\,Va^{+1}} = 4\times VIS\_A + TEGH$$

$${}^{0}G^{\gamma}_{Va^{-1}\,:\,In\,:\,Se\,:\,Va^{+1}} = 4\times EIS\_A + TEGH$$

$${}^{0}G^{\gamma}_{In\,:\,In\,:\,Se\,:\,Va^{+1}} = 4\times IIS\_A + TEGH$$

$${}^{0}G^{\gamma}_{Cu\,:\,Cu\,:\,Se\,:\,Va^{+1}} = 4\times CCS\_A + TEGH$$

$${}^{0}G^{\gamma}_{Cu\,:\,In\,:\,Va\,:\,Va^{+1}} = 4\times CIV\_A + TEGH$$

$${}^{0}G^{\gamma}_{Cu\,:\,In\,:\,Va^{+2}\,:\,Va\,:\,Va^{+1}} = 4\times CIH\_A + TEGH$$

$${}^{0}G^{\gamma}_{Cu\,:\,In\,:\,Se\,:\,Va^{-1}\,:\,Va^{+1}} = 4\times CIS\_A + TEGH + TEGN$$

Functions	CIS_A= GCUFCC+2×GSE_S+GIN_S-226835
	VIS_A= GIN_S+2×GSE_S+20000 (298 ~ 6000 K)
	VIS_B= GIN_S+2×GSE_S-169043
	IIS_A= 2×GIN_S+GSE_S+94873
	CIV_A= GCUFCC+GIN_S+46154.3
	CCS_A= 2×GCUFCC+2×GSE_S-28502
	EIS_A= GIN_S+2×GSE_S-178812
	CIH_A = GCUFCC+GIN_S+43729
	DC_A= 2×GIN_S+2×GSE_S-2×GCUFCC-195049
	LCV = -27468
	LCE = -26218
	LCI = -134189
	LIC = -1039
	LSV = -28861
	LSH= -20000
	TEGN = 46474+233.51T-12.471TLN(T)
	TEGH = 46474+207.55T-12.471TLN(T)
	GCUFCC= -7770.45775+130.485222T-24.11239Tln(T)
	-.00265684T^2+1.29222833E-07T^3+52477.8T^{-1} (298 ~1368 K)
	= -13309.7197+183.649837T-31.38TLN(T) (1358~3200)
	GIN_S= -6978.89011+92.3381153T-21.8386Tln(T)
	-.00572560T^2-2.12032167E-06T^3-22906T^{-1} (298~430 K)
	= -7032.8091+124.475108T-27.4562Tln(T)+5.4607E-04T^2
	-8.36698333E-08T^3-211707.5T^{-1} (430~3800 K)
	GSE_S = -6657.653+92.539695T-19.14Tln(T)
	-.012295T^2+2.6766666E-06T^3 (298~ 494 K)
	= -6657.653+92.539695T-19.14Tln(T)-
	.012295T^2+2.6766666E-06T^3 (494~760K)
	= -9059.16586+150.334216T-28.552Tln(T) (760~1500 K)
	Note : All the units are in J/mol

CHAPTER 6

LITERATURE REVIEW OF TRANSPARENT CONDUCTING OXIDES

The applications of TCO materials are becoming more demanding, such as in flat-panel displays, thin film photovoltaics, and architectural windows. The total area of TCO-coated glass manufactured in the USA each year is greater than 25 square miles. TCOs in PV applications must allow sun light to reach the p-n junction and collect the generated photocurrent. The device performance depends directly on the properties of the TCOs. The quantum efficiency (QE) characterization of NREL and Boeing high efficiency cells shown in Figure 6-1 indicates the large current losses at the short wavelength region due to the window layer [57]. The QE is a very useful and prompt characterization method for determining current losses in CIS devices. It is believed that the decrease of sheet resistance and the reduction of TCO absorption by factor of 2 would improve today's module by 10% [58]. This leaves space to improve the material properties of TCO materials. Both the chemical composition and the deposition method are the factors that must influence the properties of TCOs.

6.1 Material Properties of TCOs

As its name implies, the criteria for a good TCO are low electrical resistivity and high optical transparency. The conductivity can be expressed as

$$\sigma = ne\mu \tag{6.1}$$

where μ is the mobility (cm^2 V^{-1} s^{-1}), n is the concentration of free carriers (cm^{-3}), and e is the electronic charge ($\sim 1.6 \times 10^{-19}$ C). To decrease the resistivity of TCOs, one must

increase either the carrier concentration or mobility.

Increasing the carrier concentration will cause an increase of the visible absorption by free electrons according to the Beer Lambert law, which shows the linear relationship between absorbance and concentration of an absorber of electromagnetic radiation. The general Beer-Lambert law is usually written as

$$A = \alpha_\lambda \times b \times c \qquad (6.2)$$

where A is the measured absorbance, α_λ is a wavelength-dependent absorption coefficient, b is the path length, and c is the analyte concentration. In this case, the analyte refers to the electron concentration.

Increasing mobility, on the other hand, will not have a detrimental consequence on the transmittance. Therefore, the best way to achieve a high quality TCO is to increase mobility. This is the key direction followed by the community of TCO research and development.

Higher electron mobility can only be accomplished by increasing electron relaxation times, such as by either allowing the electrons to travel further between successive randomizing collisions or by using material with lower electron effective masses [59] because the mobility is related to scattering time τ (extrinsic) and effective mass m^* (intrinsic) by

$$\mu = ne\tau / m^* \qquad (6.3)$$

However, the mobility associated charge scattering process mechanism is not understood. Electron scattering is a much more difficult problem to study because many mechanisms may cause electron scattering. There are various modes of vibration of the lattice atoms that may scatter electrons (charge). If the films are extrinsically doped and the impurities

are ionized, then the ions can scatter electrons. If the mean free path is similar to the grain size, then grain boundaries may cause scattering. If the deliberately-added impurities are not ionized, they still perturb the lattice and scatter charge as neutrals. At sufficiently high concentrations of electrons ($>3\times10^{20}$ cm^{-3}), the electrons can scatter each other. Point and extended defects can also scatter charge (e.g. vacancies and dislocations). In the review paper by Coutts *et al.* [60], the grain boundary is believed not to be the scattering center for polycrystalline TCOs because a typical grain size is much larger even than the electron mean free path for heavily degenerate material.

TCOs are wide bandgap semiconductors with E_g~3.5 eV and would not have significant intrinsic conductivity. But they still conduct electricity (ρ~10^{-4} Ω cm). The origin of this conductivity is that they can be extrinsically doped with cations from one group higher in the periodic table (e.g. A^{III} in Zn^{II}O), and oxygen vacancies contribute to conduction. In extrinsically-doped TCOs, not all the impurities are ionized. This often depends on the fabrication conditions. Doping is always uncertain because the size of the impurities and their chemical activity must be considered.

To be qualified as an n-type transparent metal oxide conductor, there are two conditions that the cation metal must meet. First, the metal has to carry multivalency nature to hold high conduction electron concentrations. Second, the metal should have an electronic configuration that can avoid adding electrons to the energetically clustered bands so that the optical transition in the visible spectrum range will not occur. This also means that the conduction band minimum and higher lying bands have to be far apart [61]. Provided that oxygen vacancies is the origin of free carriers, the requirement for the anion site is that anion vacancies should be shallow donor levels instead of deep traps.

Otherwise, absorption bands can exist between the conduction band and the deep traps. The elements that meet these conditions are Cd, In, Sn, Zn and Ga. Their d-bands are all still filled after the element reacts with Oxygen.

For most applications, the most important properties of TCOs are their optical transmittance in the visible. The approach to gain knowledge about the optical properties is to use Maxwell's equations [59]. The Burstein-Moss effect always occurs for high carrier concentrations and it manifests itself as a shift to higher energy of the bandgap as shown in Figure 6-2 [59]. It happens because the states at the bottom of the conduction band are filled and more energy is needed to excite charge from the valence band. The magnitude of the shift is given by

$$\Delta E_{opt} = \left(\frac{3}{\pi} \right)^{2/3} \left(\frac{h^2}{8\,m_{cv}^*} \right) n^{2/3} \tag{6.4}$$

In this equation, m_{cv}^* is the 'reduced effective mass', which is given by

$$\frac{1}{m_{cv}^*} = \frac{1}{m_c^*} + \frac{1}{m_v^*} \tag{6.5}$$

m_c and m_v are the effective masses (i.e. curvature) of the conduction and valence band, respectively. It is these quantities that govern the magnitude of the Burstein-Moss shift. Measurement of the shift in the bandgap can give information about the reduced effective masses.

The critical industrial criteria for TCOs are minimal toxicity problems; readily available, economically stable, materials; amenable to etching/patterning; smooth or rough surfaces, as required; stable interfaces, amenable to very large volume manufacture; capable of being deposited very quickly; and non-critical manufacturing conditions.

The choice of transparent conducting oxides is determined by the application where the TCO is applied. Different applications have certain criteria for material property. The major properties that need to be considered are maximum electrical conductivity, minimum deposition temperature, production costs, toxicity, figure of merit, work function, and etchability. [62].

6.2 Status of Current TCO Materials in Research

There is a need to reduce the sheet resistance by at least two times. This will reduce scribing, series resistance, and current losses in PV modules, benefit power consumption in flat-panel displays and improve switching times in electrochromic windows.

Up to now, the most widely studied binary oxides are SnO_2, In_2O_3, ZnO, and CdO. SnO_2 is currently used as a front electrode on CdTe solar cells. In-doped SnO_2, ITO, is the best TCO material achieved so far. Indium, however, is a very expensive material. ZnO is believed to be a potential candidate to replace ITO due to the low cost and harmless nature of Zn. ZnO also exhibits a continuing downtrend in resistivity with time, while other binary oxides have ceased to improve (Figure 6-3) [61]. To improve the efficiency of solar cells by confining more light, milky transparent electrodes are required. Milky ZnO films have a textured surface and are easier to produce at low temperature compared to SnO_2. Solar cells use soda lime glass as a substrate. Sodium can diffuse into the TCO and decrease its conductivity especially for tin oxide because sodium diffuses rapidly at a high substrate temperature, and the tin oxide deposition temperature is higher than 550 °C. Therefore, ZnO is a technologically important material in $CuInSe_2$ material-based photovoltaic devices where the low temperature

deposition for TCO is required. However, ITO is still preferred for flat-plane displays because ZnO is etched during the wet treatments of present photolithography processes. SnO_2 can be deposited by CVD for large scale spatially uniform films, and this is a competitive advantage over ZnO:Al, which is always prepared by sputtering.

Extremely high electron mobility and a wide range of fundamental optical absorption bandgap energies (E_g) have been achieved in CVD-CdO. CdO may work as an electrode for tandem PV solar cells. It has, however, a fundamental optical bandgap of only 2.3 eV. Because of the toxicity of Cd compounds and narrow band gap of CdO, it has not been widely used as a TCO material. High electron mobility has been achieved and could make CdO a candidate for new TCO applications. Unlike other TCOs, the carrier concentration of CdO increases as the deposition temperature increases. This raises doubt on the usual argument in TCOs that oxygen vacancies are responsible for the carriers because the oxygen vacancy decreases as the deposition temperature increases.

Although the binary compound TCO materials are still the dominant TCO material for most application because it is simpler to control the film chemical composition, there is active research on ternary and multicomponent TCO materials to satisfy more specific applications. The multicomponent oxides are the combinations of binary and ternary oxide compounds. Ternary compounds, such as $Zn_2In_2O_5$, $MgIn_2O_4$, Cd_2SnO_4, Zn_2SnO_4, $CdIn_2O_4$ have been explored recently. Figure 6-4 shows the approach that the NREL is taking as an example of the development of multicomponent oxides films [59]. This is a compositional phase space which must be explored just to optimize n-TCOs created from combinations of well known single-metal n-TCOs. Three popular binary oxides are taken, and a combination is made between them. The solubility of ZnO needs to be

increased to turn the "fat slice" into more of a circular region. A superior TCO is believed to exist somewhere in this diagram.

6.3 Fabrication of TCOs

For the fabrication of a TCO, several methods have been successful. For manufacturing, sputtering and CVD are the most widely used. Spraying, PLD, and evaporation are all research techniques.

6.3.1 Spray Pyrolysis

Spray pyrolysis is a method well known for its simplicity, reproducibility, and possibility to produce cheap large area films. A TCO is obtained by spraying an aqueous solution onto a heated glass substrate. . However, the films prepared by this method, in general, have bad morphology with a high density of pinholes.

6.3.2 Pulsed Laser Deposition (PLD)

The advantages of PLD are its ability to reproduce the target composition under appropriate conditions, an inherently clean process, a significant degree of parameter freedom, and the ability to deposit multilayer of different materials. However, it can only produce small size uniform film. So, it is restricted for research purposes.

6.3.3 Chemical Vapor Deposition (CVD)

For CVD, the reactant gases are introduced into an enclosed reactor with a carrier gas (typically N_2). More than one gas passes over a heated substrate and decomposes into components. There are several modes of operation in CVD: low pressure, plasma enhanced, atmospheric pressure, and organometallic. The coatings obtained are typically hard and durable. CVD has very low capital cost. It is capable of producing mechanically tough films of large area and acceptable electrical and optical properties. ,

For CIS-based substrate solar cell application, however, CVD is not a suitable method due to its high processing temperature.

6.3.4 Sputtering

Sputtering is one of the most commonly used methods with high deposition rate for the deposition of TCOs. Compared to CVD, sputtering is characterized by the advantages of low substrate temperature, very good thickness uniformity, high film density, good process controllability, and long-term process stability. Sputtering techniques are classified as DC glow discharge sputtering, RF sputtering, and ion beam sputtering. Each technique can be sub-divided into magnetron and diode sputtering. Depending on the target, the sputtering can be reactive sputtering and non-reactive sputtering.

DC Glow Discharge, Ion Beam Sputtering and RF Sputtering

DC glow discharge sputtering exhibits good control of the power, voltage or current of the discharge. Compared to RF sputtering and ion beam sputtering, its deposition rate is relatively high. The limitation of DC glow discharge sputtering is that conductive targets are needed, and thus not suitable for reactive sputtering. In contrast, RF sputtering can be applied to any target regardless its conductivity.

Ion beam sputtering is a complicated sputtering technique that provides precise control of deposition. The drawback of ion beam sputtering is that it requires neutralization of the beam so as not to charge the target surface, which may decrease or completely stop sputtering [63].

Magnetron and Diode Sputtering

A planar sputtering target geometry is one of the several possible source geometries. It has two varieties: diode and magnetron. The name diode sputtering

derives from the I-V characteristics of the plasma, which is similar to that of a diode, in that is exhibits more current flows with forward bias versus very little current flow with reverse bias. The purpose of using a magnetic field in a sputtering system is to make more efficient use of the electrons and cause them to produce more ionization.

The basic feature of a magnetron discharge is the confinement of the plasma in front of the target (cathode) by the combination of electric and magnetic fields to reduce ion damage at the substrate surface.

Reactive Sputtering and Non-reactive Sputtering

Reactive sputtering is a method to deposit films that have a different composition from the target by adding a gas to the sputtering system to produce a material by reaction of the gas with the target material.

Sputtering Configuration

Two configurations are employed for sputter deposition of ZnO. One is the substrate perpendicular to a target. This configuration can reduce the bombardment of the film by energetic O⁻ ions and O atoms which are generated in front of the target and fly normally to the target surface, increasing the resistivity of the film. The other one is the normal planar configuration with substrate parallel to target.
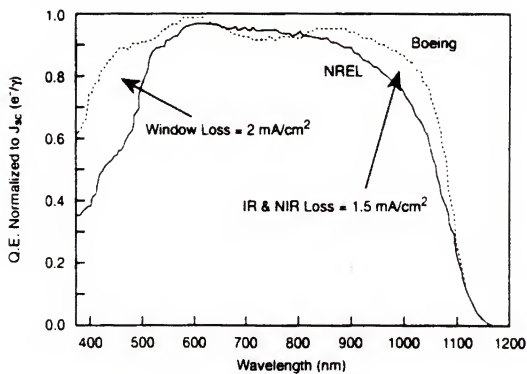
Figure 6-1. Quantum efficiency spectra of NREL and Boeing films [57].
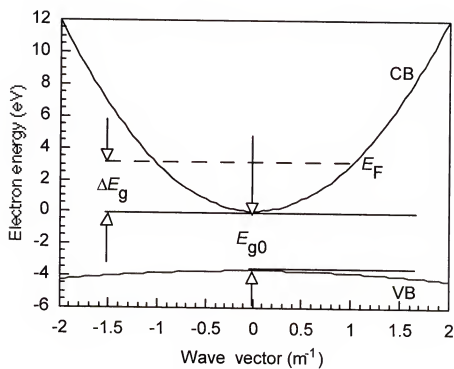
Figure 6-2. Band diagram illustrating the Burstein-Moss Shift [59].
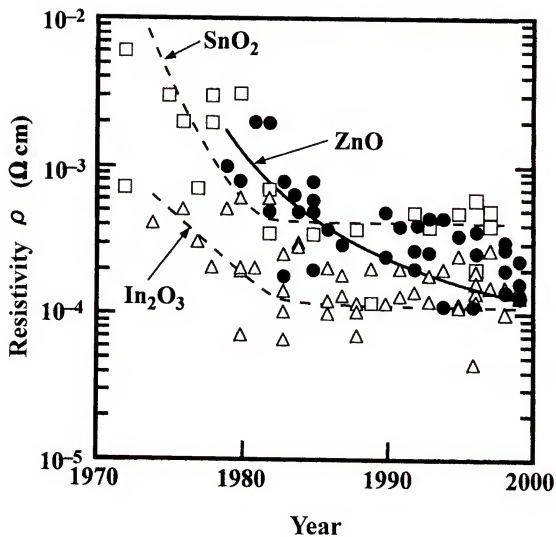
Figure 6-3. Comparison of resistivity trends for binary TCO over the period 1970-2000 [61].
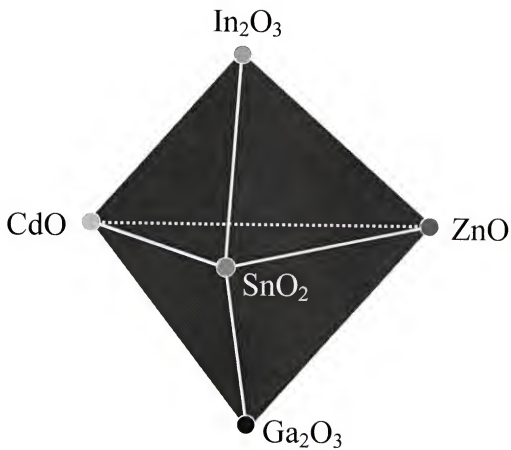
Figure 6-4. n-type TCO phase space region [59].

CHAPTER 7
THERMODYNAMIC MODELING OF F DOPING IN SNO$_2$

Fluorine-doped tin oxide (FTO) films are widely used as a transparent conductor in solar cell applications. This transparent conductive oxide (TCO) material can be prepared by several manufacturing techniques, including sputter deposition, chemical vapor deposition (CVD), and spray pyrolysis deposition. For solar cell applications it is desirable for the TCOs to exhibit both high electrical conductivity and high transparency. It is well known that high fluorine concentrations in the film increase the electrical conductivity, but unfortunately at the same time the film transparency decreases. A method for estimating the solubility of F in SnO$_2$ would therefore be most useful for establishing optimal processing conditions. In this study the Delta Lattice Parameter (DLP) model [66] was used to estimate the interaction energy of the pseudobinary SnF$_2$-SnO$_2$ solid solution. The resulting model then allows a reasonable estimation of the extent of F incorporation in a SnO$_2$ film during CVD, assuming that the film growth is mass transfer limited and that the growth interface is at equilibrium. Experimental observations available in the literature [72-73] are used to determine the components present in the gas phase, yielding a key piece of information needed to populate the database that serves as the basis for a thermodynamic analysis using the Thermo-Calc software package [64]. Thermo-Calc was developed in 1981, and is a powerful and flexible tool for performing various kinds of thermodynamic and phase diagram calculations, including analysis of CVD-grown thin films.

This chapter is organized as follows. Section 7.1 describes the experimental and calculation procedure followed, including a discussion of the relevant thermodynamic models involved, the evaluation of the interaction parameters needed for the models, the calculation of fluorine solubility, and an analysis of the effect of various CVD parameters in solubility. Section 7.2 summarizes the results along with a comprehensive discussion. Finally, section 7.3 offers concluding remarks.

7.1 Experimental and Calculation Procedure

FTO films were deposited on a glass substrate using a gas mixture containing an F precursor, tetramethyltin (TMT), and oxygen, in a low-pressure chemical-vapor deposition (LPCVD) reactor. The three precursors considered were $CBrF_3$, ClF_3, and CF_4. The reactor features an infrared heating lamp that defines five distinct heating zones on the substrate. The gases were introduced into the reaction chamber via two injectors located on the top and bottom of an end-cap flange. Films were grown at selected temperatures, and various partial pressures of precursor gases. The resulting films were characterized via Hall effect measurements using a Bio-Rad HL5500 Hall system to determine the carrier concentration. In addition, SIMS profiles using a CAMECA IMS 5f system were taken to estimate the F content of the deposited films.

7.1.1 Thermodynamic Models

The two phases, namely, gas and FTO solid solution are in equilibrium at growth interface assuming the film growth is a mass transfer limited process. If reactants and products have different rates of mass transfer, then the near surface composition will be different from the bulk gas composition. Modeling CVD deposition conditions by an equilibrium model generally gives reasonable results for intensive variables such as bulk film composition. Thermodynamic models for both phases are needed to construct a

Gibbs energy database to perform equilibrium calculation. The development of a thermodynamic model requires adopting a description of the FTO solid solution. An assessment of the phase equilibrium and thermodynamic properties of the Sn-O system have been performed by Dupin [65], and these results are taken as a starting point. The solid solution formed upon adding F to SnO_2 is modeled as a pseudobinary solid solution of SnF_2 and SnO_2, with a Gibbs energy of mixing obtained from regular-solution theory [64]. The gas phase is assumed as an ideal mixture of all its components.

a)   FTO Solid-Solution Phase

The FTO solid phase is described by a regular solution model whose Gibbs energy can be written as

$$G^{FTO} = {}^{ref}G^{FTO} + {}^{id}G^{FTO} + {}^{ex}G^{FTO} \tag{7.1}$$

with ${}^{ref}G^{FTO} = x_{SnO_2}G^0_{SnO_2} + x_{SnF_2}G^0_{SnF_2}$, ${}^{id}G^{FTO} = RT(x_{SnO_2}\ln x_{SnO_2} + x_{SnF_2}\ln x_{SnF_2})$, and

${}^{ex}G^{FTO}$ is the excess Gibbs energy expressed by the regular solution model

$$^{ex}G^{FTO} = x_{SnO_2}x_{SnF_2}\Omega_{SnO_2-SnF_2} \tag{7.2}$$

where x_{SnO_2} and x_{SnF_2} are the mole fractions of the two end members, respectively SnO_2 and SnF_2, in the FTO solid solution phase. The symbols $G^0_{SnO_2}$ and $G^0_{SnF_2}$ represent respective the standard Gibbs energy of the pure SnO_2 and SnF_2 phases, and $\Omega_{SnO_2-SnF_2}$ is the regular-solution interaction energy parameter and is related to the energies of the bonds between SnO_2 and SnF_2. Positive values of $\Omega_{SnO_2-SnF_2}$ represent repulsive interactions, and negative values are associated with attractive interactions. The value of Ω is evaluated through the Delta Lattice Parameter (DLP) model as described in the next section.

b)   Gas Phase

Ideal mixing is often assumed for a gas mixture at or below atmospheric pressure and at elevated temperature [64]. The Gibbs energy of the gas phase is then given by

$$G^{Gas} = {}^{ref}G^{Gas} + {}^{ideal}G^{Gas}_{mix} \qquad (7.3)$$

with $G^{ref} = \sum_i x_i G_i^0$ and $G^{ideal}_{mix} = RT \sum_i x_i \ln x_i$, and where x_i is the mole fraction of component i and G_i^0 defines the standard Gibbs energy of the pure gas component i. The standard state of a substance is defined as its pure form in internal equilibrium under a pressure of 1 bar and at a given temperature. The number and type of components present in the gas phase are determined by experimental observation [72, 73].

7.1.2 F Solubility in SnO_2

The solubility of F in SnO_2 is limited and similarly the solubility of O in SnF_2 is limited. To estimate the solubility of F in SnO_2 the conditions of equilibrium requires that the chemical potential of SnF_2, μ_{SnF_2}, in SnO_2 equal that in the SnF_2-rich phase. Assuming that the SnF_2-rich phase is essentially pure SnF_2, the equilibrium condition states that the activity a_{SnF_2} in SnO_2 is unity when referenced to pure SnF_2. Further it is assumed that the solid solution between SnO_2-SnF_2 can be described by a regular solution model;

$$\Delta G^{XS}_m = \Delta H^*_m = \Omega_{SnF_2 - SnO_2} x_{SnF_2} \left(1 - x_{SnF_2}\right) \qquad (7.4)$$

With this model the activity coefficient of SnF_2 in SnO_2, γ_{SnF_2}, is

$$RT \ln \gamma_{SnF_2} = (1 - x_{SnF_2})^2 \Omega_{SnF_2 - SnO_2} \qquad (7.5)$$

With the condition that the $a_{SnF_2} = 1$, the solubility of SnF_2 in SnO_2 is given by

$$x_{SnF_2} = \exp(-\Omega_{SnF_2-SnO_2} / RT) \qquad (7.6)$$

To use this equation, a method to estimate the value of $\Omega_{SnF_2-SnO_2}$ is next developed.

7.1.3 Interaction Parameter Evaluation

The value of the interaction energy between SnO_2 and SnF_2 is estimated following an approach inspired by the standard Delta Lattice Parameter (DLP) methodology [66]. The standard DLP model [66] based on the dielectric theory of electronegativity of Philips and Van Vechten [67] suggests that the average band gap energy in compound semiconductor solutions that are primarily covalently bonded varies exponentially as $a_0{}^n$, where a_0 is the lattice constant. The enthalpy of atomization ΔH^{at} of either end member or of solid solution, which is related to bonding energy, is represented through the power law

$$\Delta H^{at} = Ka_0{}^n \qquad (7.7)$$

where K and n are empirical parameters obtained from experimental equilibrium data. The standard DLP model produces the fixed values of $K = 4.8 \times 10^4$ kJ/mol Å$^{-2.5}$ and $n = -2.5$ for cubic covalent systems. The components SnO_2 and SnF_2, however, are more ionic and stable in the tetragonal structure. Thus new values for the power law exponential constant n and proportionality constant K must be estimated for the Group IV tetragonal oxide semiconductors. This can be achieved by making use of available covalent bonding energy and lattice parameter data. The tetragonal oxides SiO_2, GeO_2, SnO_2 and PbO_2 are chosen because they belong to the same space group, namely, $P4_2/mnm$ [68]. The original DLP model considered only one lattice parameter because it was developed for cubic systems. In our approach for tetragonal systems, the lattice constant a is used for estimating the exponential parameter n and proportionality

parameter K. Selecting the a value is supported by the observation that this particular lattice parameter changes significantly in CVD-grown $Sn(O_xF_{1-x})_2$ films, as shown by the data in Table 7-1. The lattice constants reported in the table were measured by XRD for both pure SnO_2 and for fluorine-doped films SnO_2:F with 9 at. % SnF_2. Note that the value of the a parameter changes by 0.62% while the c parameter changes by only 0.09%. As a first step to estimate the interaction energy, the enthalpy of atomization of each compound is needed.

The enthalpy of atomization of a compound is the enthalpy change associated with breaking apart the compound to its gaseous atoms at 298 K and 1 atm. The enthalpy of atomization gives directly the sum of the contributing bond enthalpies for a gaseous compound, but for solids and liquids additional enthalpy terms are included in H^{at}, reflecting intermolecular and interionic interactions. Thus for the general compound AB_2, the atomization process is:

$$AB_2 \rightarrow A(g) + 2B(g) \tag{7.8}$$

The corresponding enthalpy of atomization of a compound is:

$$\Delta H^{at} = -\Delta H_f^0 + H^{at}(A) + 2H^{at}(B_2) \tag{7.9}$$

where ΔH_f^0 is the enthalpy of formation of AB_2 from solid A and B_2 gas, $H^{at}(A)$ and $H^{at}(B_2)$ are respectively the atomization enthalpies for solid A and gaseous B_2. The values of ΔH_f^0 are taken from the JANAF compilation [70]. Values for the latter two enthalpies are available in the literature [69]. Table 7-2 summarizes the calculated values of atomization enthalpies as well as the lattice constants for tetragonal compounds of interest. The left most column lists the four tetragonal oxide compounds and

tetragonal SnF_2. The enthalpy of atomization of the pure covalent bond is listed in the second column. The third column is the enthalpy of atomization when the ionicity of the bond is taken into consideration. The ensuing columns show the lattice constants a_0 and c_0. Note that the lattice constant a_0 reported for SnF_2 in Table 7-2 is for the pure compound.

A regular solution interaction parameter, $\Omega_{SnO_2-SnF_2}$, can now be calculated by assuming that the mixing enthalpy ΔH^M follows the regular solution form

$$\Delta H^M(x) = \Omega_{SnO_2-SnF_2} \; x(1-x) \qquad (7.10)$$

where x is the fractional composition of the end member SnF_2. The composition dependence of ΔH^M is given by the relation

$$\Delta H^M = (1-x)\Delta H^{at}_{SnO_2} + x\Delta H^{at}_{SnF_2} - \Delta H^{at}_{alloy} \qquad (7.11)$$

where $\Delta H^{at}_{SnO_2}$ is the atomization energy of SnO_2, $\Delta H^{at}_{SnF_2}$ is the atomization energy of SnF_2, and ΔH^{at}_{alloy} is the atomization energy for the alloy (solid solution) formed by SnO_2 and SnF_2. Now, after setting $x = 0.5$, equations (7.10) and (7.11) can be combined with equation (7.7) and solved for the interaction parameter to obtain

$$\Omega_{SnO_2-SnF_2} = 4K\left\{-\left(\frac{a_{SnO_2}+a_{SnF_2}}{2}\right)^n + \frac{1}{2}\left(a^n_{SnO_2} + a^n_{SnF_2}\right)\right\} \qquad (7.12)$$

In the following subsection a), an estimate of Ω is developed assuming that the lattice constants appearing in equation (7.12) are interpreted as the corresponding lattice parameter a_0 in the tetragonal sublattice. Details are given below.

a) <u>**Power Law Based on Lattice Constant a_0**</u>

Figure 7-1 shows a plot of the atomization energy for the four tetragonal oxides versus the crystal's lattice constant a_0. The diagonal markers denote the atomization energy values for the oxides reported in Table 7-2 for the case of covalent bonds. The square markers denote the respective oxide energies for the case where the ionicity of the bonds is also taken into account. The continuous curve shown in the figure represents the plot of a least-squares fit of the power law given in equation (7.7) to the covalent bond data, yielding the model

$$\Delta H^{at} = +18.35 \times 10^4 a_0^{-3.23} \text{ kJ/mol} \quad \text{(Covalent)} \tag{7.13}$$

Finally, the dashed line represents the least-squares fit to the data that involves ionic effects through the model

$$\Delta H^{at} = +30.16 \times 10^4 a_0^{-3.38} \text{ kJ/mol} \quad \text{(Covalent+Ionic)} \tag{7.14}$$

Selecting $K = 18.35 \times 10^4$ kJl/mol and $n = -3.23$ from equation (7.13) and substituting these values into equation (7.12) yields the value of the interaction parameter $\Omega = +35.6$ kJ/mol for the case of covalent bonding. Proceeding analogously, adopting the parameters indicated in equation (7.14) yields the valued $\Omega = +48.9$ kJ/mol when taking the ionicity of the bond into consideration

The gas phase is generally at a relatively low pressure and at elevated temperature near the substrate surface. Chemical compositions in equilibrium with the solid solution were calculated using the Thermo-Calc software tool [64], which requires input of the interaction parameter to compile a database of Gibbs energy for each phase involved in the equilibrium.

b) <u>Validation of the Approach</u>

To validate the results obtained via the DLP method, the interaction parameter for $SiO_2 - GeO_2$ was calculated based on the power law relationships (7.12) and (7.10) and compared to the value obtained from the phase diagram [71]. The results are listed in Table 7-3, where it can be seen that the reported values are in good agreement. This closeness of the results suggests that the proposed DLP approach is consistent with phase-diagram data.

All the ensuing calculations in this paper are based on the interaction parameter value $\Omega = 8.52$ kcal/mol. Calculations based on the interaction-parameter values that included ionicity show a similar trend, except for a slight F solubility difference.

7.1.4 CVD Mechanism

The mechanism of the chemical vapor deposition of SnO_2 from tetramethyltin and oxygen is complex. Borman *et al.* [72] studied the gaseous reaction by-products by gas chromatography and mass spectrometry. They found that virtually all the TMT reacted and that only 0.1 mol% of the CF_3Br reacted at the growth conditions 743K, 0.1 mol% TMT, 3.95 mol% CF_3Br, and 20 mol% O_2. The dominant species observed in the reactor effluent were H_2CO, H_2O, HF, CO, CO_2, CH_4, and CH_3Br. In addition to these, HBr, C_2H_6, C_2H_4, CF_3H, C_2H_2, CF_2CH_2 also exists in a ppm scale. Li *et al.* [73] found that the presence of CH_4 can increase the conversion level of $CBrF_3$. Furthermore, the species CHF_3, CH_3Br, $C_2H_2F_2$, C_2H_2, $C_2H_3F_3$, C_2HBrF_2, C_2H_3F, C_2HF_5, C_2F, C_6H_5F, $CHBrF_2$, C_2H_3Br were found to be the main gas by-products [73]. Therefore, the following mechanism for CVD formation of FTO is suggested:

Based on the available evidence, it is possible to propose a mechanism for the CVD formation of FTO. First, TMT is completely decomposed at the substrate surface by the reaction

$$Sn(CH_3)_4 \rightarrow Sn + 4CH_3^{\bullet} \qquad (7.15)$$

and tin is oxidized through the reaction:

$$Sn + O_2 \rightarrow SnO_2 \qquad (7.16)$$

Then, some of the $CH_3^{\bullet}$ material is oxidized to CO_2 and H_2O, and the residual $CH_3^{\bullet}$ participates in enhancing the pyrolysis of $CBrF_3$ and produces the gas by-products mentioned in the previous paragraph.

To better understand the growth chemistry, a chemical equilibrium calculation was performed assuming that the growing vapor-solid interface is at equilibrium. The calculation is carried out within the temperature range of $400 \sim 900$ K because above 900 K a carbonaceous deposit was observed on the surface of the thermocouple sheaths providing evidence of a two-phase film deposition [73]. The results of the calculation are presented in Section 7.2.

7.2 Results and Discussion

7.2.1 Solid Solubility Limit of F in Various TCO Materials

The oxides SnO_2, CdO, ZnO_2, and In_2O_3 are the most commonly used TCO materials. The F doping solubility limit in these materials is estimated by using interaction energies given by the DLP model (see equation (12)), and the results are shown in Figure 7-2. Note that in these oxides, the greatest F solubility is observed in SnO_2, which is consistent with the experimental observation that the F solubility in SnO_2 is higher than that in ZnO [75]. There is great interest in CdO because of its high

electron mobility, and because undoped CdO can produce a carrier concentration up to 1×10^{21} cm^{-3}. The doped CdO materials listed experimentally in [76] show insignificant variations in carrier concentration, indicating that F has a low solubility in CdO, a fact that is consistent with the results of Figure 7-2. The bottom-most curve on Figure 7-2 shows the solubility of fluorine in In$_2$O$_3$ is the lowest of the four oxides considered. Although there are no experimental data to support this prediction, the result suggests that F doping of In$_2$O$_3$ would not be effective. As expected, the solubility of F increases with deposition temperature, as does the concentration of oxygen vacancies for most oxides. Furthermore, an increase in grain size is expected at higher temperature. Thus deposition of high conductivity binary oxides at high temperature is preferable, with the possibility of quenching in the F at higher concentration than the room temperature equilibrium value.

7.2.2 Analysis of FTO Growth via CVD

Figure 7-3 shows the chemical equilibrium conversion level of F precursors in a CVD system for three different precursors as a function of temperature. The conversion level is defined as the ratio of the amount of decomposed precursor to the initial precursor input in the gas phase. The calculation was made by assuming the species of interest were those discussed in section 7.1.4 and then using the Thermo-Calc software package [64]. The data given in the figure show that the extent of decomposition of ClF$_3$ is greater than CBrF$_3$, which in turn decomposes to a greater extent than CF$_4$. Figure 7-4 plots the equilibrium F concentration in the FTO solid-solution phase versus deposition temperature for different precursors. The extent of the equilibrium F concentration in solid phase follows the sequence: ClF$_3$>CBrF$_3$>>CF$_4$ as shown in Figure 7-4. Therefore,

the first two are the preferred precursors. This is consistent with experimental observations that ClF3 is the most efficient precursor in providing F doping in SnO_2 [74].

Figure 7-5 shows the conversion of $CBrF_3$ as a function of initial $CBrF_3$ inlet component at different deposition temperatures. For all temperatures considered, the conversion level is always higher at low initial $CBrF_3$ concentrations. It is relevant to note that the conversion is relatively low at the growth temperature of typically used for the CVD growth (773 K), and nearly independent of the initial $CBrF_3$ mole concentration. More specifically, at 773 K and at initial $CBrF_3$ mole fraction of 0.04 only 0.6% of $CBrF_3$ decomposes according to the calculation, which is on the same order of the experimentally reported decomposition of 0.1 % at 1 atm [72]. Thus increasing temperature or changing precursor would likely be more effective strategies for providing more available F.

Figure 7-6 compares the calculated atomic concentration of F in FTO with the experimentally-measured F secondary ion counts and measured carrier concentration in CVD films grown as part of this study. The results are plotted as a function of $CBrF_3$ partial pressure. The triangle markers are the measured ion F counts measured by SIMS, and the square markers are the experimental carrier concentration data points by Hall measurements. The dashed line without any markers is the F concentration in the FTO film calculated. As can be seen, the calculated and experimental trends are similar, that is, both the F and carrier concentrations increase rapidly as the $CBrF_3$ initial mole fraction increases. Note also that the carrier concentration increases as the F atomic concentration increases, and eventually saturates for large $CBrF_3$ inlet compositions. The F concentration (dashed line) is much larger than carrier concentration (square marker);

this is explained by the fact that the F in the SnO_2 is not totally ionized. At other temperatures, as shown in Figure 7-7, the F concentration follows the same trend as described above except that there is a higher F concentration at higher temperature.

Figure 7-8 shows the F concentration in the FTO film as a function of growth temperature. The top dashed is the calculated solubility limit. The bottom solid line is the calculated F concentration, which increases with temperature since more F precursor decomposition occurs. However, in the actual CVD experiments, the $CBrF_3$ sticking coefficient decreases as the temperature increases; therefore, the experimental F concentration may be observed to decrease at higher temperature.

7.3 Conclusions

A model was developed to estimate the equilibrium fluorine solubility in fluorine-doped tin oxide (FTO) as a function of temperature and of the partial pressure of dopant precursor. The modeling results with $CBrF_3$ precursor show that the F concentration increases with the temperature and eventually, it may reach the solubility limit. The calculated and experimental trends are similar, that is, both the F and carrier concentrations increase rapidly as the $CBrF_3$ amount increases. The incorporated F concentration, however, is much larger than the carrier concentration, supposedly due to incomplete F ionization. The effect of different dopant precursors (CF_4, $CBrF_3$, and ClF_3) on F incorporation has been estimated and compared with experimental results. It is found that $CBrF_3$ is a reactive precursor although not as reactive as ClF_3. The reactivity of CF_4 is much lower than the other two precursors. This is consistent with experimental observation. The F doping solubility in the commonly used SnO_2, CdO, ZnO and In_2O_3 transparent conductive oxides was also compared using Delta Lattice

Parameter model. The result indicates that F doping solubility follows the trend SnO_2 >ZnO>CdO>In_2O_3.
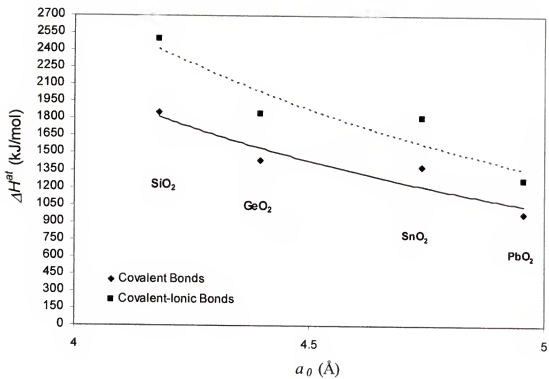
Figure 7-1. Power law relationship relating the heats of atomization and lattice constant a_0 for oxides of interest under the assumptions of covalent-only bonds and covalent plus ionic bonds.
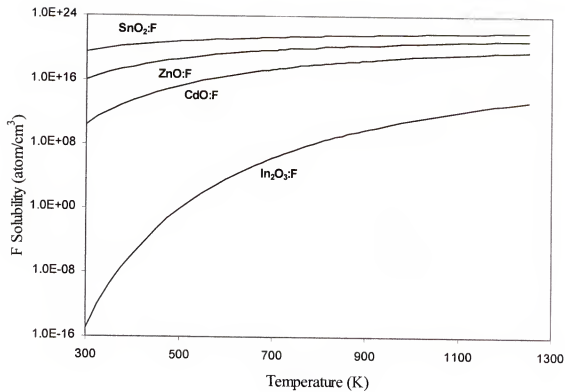
Figure 7-2. Solid solubility limit of fluorine in different TCO materials versus temperature calculated using the DLP model.
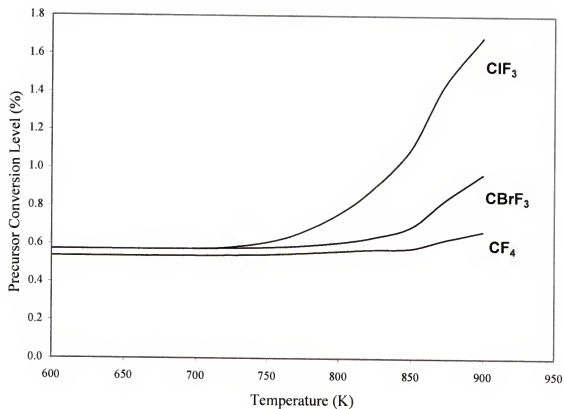
Figure 7-3. Calculated conversion level of three different fluorine-containing precursors as a function temperature. CVD conditions: 18.96 mol% $CBrF_3$, 44.43 mol% O_2, 0.592 mol% TMT, 36.02 mol% N_2 and P=40 Torr.
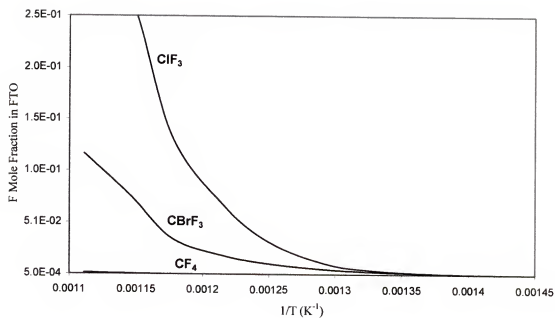
Figure 7-4. Calculated equilibrium fluorine concentration in FTO of three different fluorine-containing precursors as a function temperature. CVD conditions: 18.96 mol% CBrF3, 44.43 mol% O_2, 0.592 mol% TMT, 36.02 mol% N_2 and P= 40 Torr.
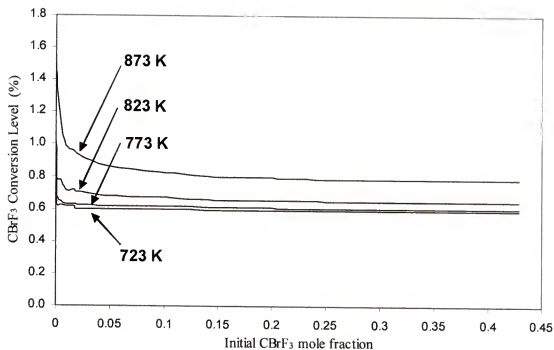
Figure 7-5. Calculated CBrF$_3$ conversion level versus initial CBrF$_3$ mole fraction at different temperature at initial mole concentration. CVD conditions: 44.43 mol% O$_2$, 0.592 mol% TMT and total pressure of 40 Torr.
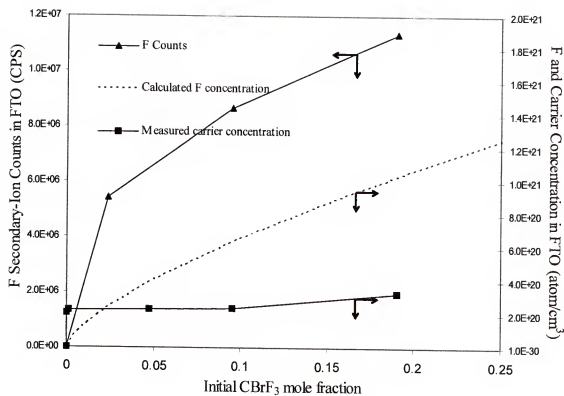
Figure 7-6. Comparison of F concentration in FTO versus initial CBrF$_3$ mole fraction by calculation, Hall measurement and SIMS analysis at fixed T$_s$= 550 °C, 44.43% O$_2$, 0.592% TMT and total pressure 40 Torr.
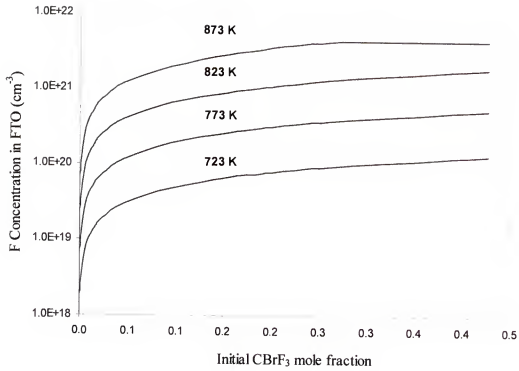
Figure 7-7. Calculated F concentration at different growth temperature as a function of dopant precursor initial concentration. CVD conditions: 44.43 mol% O_2, 0.592 mol% TMT and total pressure of 40 Torr.
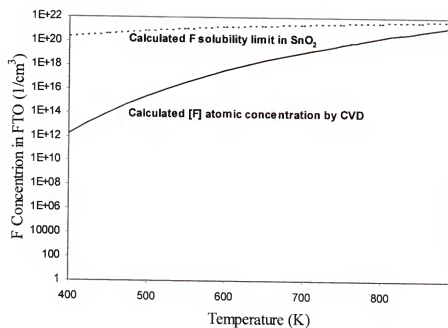
Figure 7-8. Comparison of F Incorporation and solubility limit as a function of temperature. CVD conditions 18.96 mol% CBrF$_3$, 44.43 mol% O$_2$, 0.592 mol% TMT, 36.02 mol% N$_2$ and P=40 Torr.

Table 7-1. Experimental lattice constant values and composition of FTO films grown by CVD.

	a	c
	(Å)	(Å)
SnO_2	4.740	3.177
SnO_2:F	4.772	3.174

Table 7-2. Atomization enthalpy and lattice constants for selected tetragonal compounds.

Material	Enthalpy of Atomization (Covalent Bond) ΔH^{at} (kJ/mol)	Enthalpy of Atomization (Covalent+Ionic Bond) ΔH^{at} (kJ/mol)	Lattice Constant a_0 (Å)	Lattice Constant c_0 (Å)
SiO_2	1855	2495.3	4.179	2.6649
GeO_2	1429.1	1845.5	4.3963	2.8626
SnO_2	1379.8	1814.6	4.738	3.187
PbO_2	975.2	1263.1	4.9564	3.3877
SnF_2	1107.7	1844.6	5.0733	8.491

Table 7-3. Comparison of calculated Ω for SiO_2-GeO_2 based on DLP and experimental Ω obtained from phase diagram data.

	Ω From DLP (kJ/ mol)	Ω From $T_c = \Omega/2R$ (kJ / mol)
$SiO_2 - GeO_2$	a 29.7	27.9 [71]

CHAPTER 8
RF DIODE SPUTTERING DEPOSIITON OF ZNO:AL TCO

In the past few years, transparent conducting oxides such as SnO_2, CdO, ZnO, In_2O_3 have attracted interest because of their high electrical conductivity and optical transmittance in the visible region of the solar spectrum, together with their high reflectance in the IR [77]. Among these materials, ZnO is a technologically important material in $CuInSe_2$ material-based photovoltaic devices because it is much cheaper than other oxides and possesses a very sharp UV cut-off. Its wide optical bandgap energy (3.3 eV) allows the transmittance of most of the useful radiation. It is also used as a window layer for a:Si devices because of its high chemical resistance to hydrogen plasma. RF sputtering is predominantly used for the deposition of zinc oxide films. The key issue is the optimization of the film optical and electrical properties – high optical transparency and low resistivity.

The influence of experimental parameters, such as the base pressure, working gas pressure, and RF power on the growth rate, morphology, optical transmittance, electrical resistivity and crystallinity is studied with the aim of optimizing the process to obtain thin uniform films of a quality necessary for solar cells. The objective is to determine the most suitable deposition conditions to obtain ZnO:Al thin films with a low resistivity and high transmittance and to obtain thin uniform films of a quality necessary for solar cells.

8.1 Experimental Apparatus

Al doped zinc oxide films were prepared using a Perkin Elmer 4400 sputtering RF system. A schematic diagram of this sputtering system is shown in Figure 8-1. The

target is located at the top and is an 8 in plate (currently Mo, undoped ZnO, and doped ZnO:Al targets) handled by an 8 in RF diode source [78-79]. The target is mechanically clamped to a water-cooled Al electrode. Each target can be independently covered by a movable shutter mounted on the chamber wall. The adjustable shutter height was set at approximately 2 cm in front of the target. When it is closed, the shutter does not interfere with the well confined rectangular ring discharge. The substrate to target distance is 9 cm. The sources and the substrate tables are cooled by chilled water. Maintaining a low substrate temperature during deposition of the TCO is a requirement for CIGS substrate solar cell fabrication. An 8 inch diameter RF magnetron is currently added to ZnO:Al$_2$O$_3$ (98 wt%, 2 wt%) target, and termed AZO henceforth. The purpose of using a magnetic field in a sputtering system is to make more efficient use of the electrons in increasing ionization. The basic feature of a magnetron discharge is the confinement of the plasma in front of the target (cathode) by the combination of electric and magnetic fields. The uniformity of the deposition is enhanced by a rotary motor

8.2   Film Characterization

The characterization methods used in this study are surface profilometer for thickness measurement, XRD for structure analysis, four point probe for electrical property measurement, spectrophotometer for transmittance measurement, and AFM for surface morphology and roughness measurement.

Surface Profiler – Thickness (Dek-tek)

Film thickness was measured by an ALFA-Step 500 surface profiler. A step profile is created by wet etching a line on the film.

X-ray Diffraction – XRD Pattern, Strain, Crystallinity

A Phillips APD 3720 powder diffractometer with CuKα radiation (λ=1.54056 Å) was used to record X-ray diffraction patterns of deposited films to evaluate crystalline phase, crystallite orientation, and mechanical (strain level) properties.

Four Point Probe - Resisitivity

The film resistivity ρ was determined by a four-point probe. Four point probe is a very simple, nondestructive way to measure the sheet resistance, as shown schematically in Figure 8-2. The Alessi four point probe used in this study has a very sharp tungsten carbide tip with a point radius of 0.002 in [78]. Tungsten is chosen for its hardness. The distance between the four equally spaced probes is 0.05 in. A known current is applied between the two outer needles, and an open circuit voltage between the two inner needles is read from a nanovolt electrometer. For thin films, the sheet resistance R_S is defined as the resistance of a bar of material of unit length and width, with thickness t. The unit for R_S is ohms/square or $\Omega/\square$. The sheet resistance is related to V/I by a geometrical correction factor k (R_S = k V/I). In this case, the correction factor is 4.53 [95]. The geometry of the sample determines the correction factors that must be used, additionally the position of the probes on the sample and the spacing between the probes. The need for correction factors is caused by the proximity of a boundary which limits the possible current paths in the sample. The expression for resistivity for this study is:

$$\rho = 4.53\, t \cdot \frac{V}{I} \qquad (8.1)$$

The advantage of using four point probe is to avoid the inaccuracy caused by the resistance between the film and the contact. Therefore, an ohmic contact is not necessary for four point probe measurements.

Spectrophotometer - Transmittance

Transmission spectra of films were recorded from 200 to 1500 nm using a Perkin-Elmer spectrophotometer 2000. A blank sample was measured before the real measurement to establish the absorption caused by the sample holder as shown in Figure 8-3.

AFM – Surface Morphology, Roughness

The AFM uses a sharp probe moving over the surface of a sample in a raster scan. The probe is a tip on the end of a cantilever which bends in response to the force between the tip and the sample. Figure 8-4 [80] illustrates how this works. As the cantilever flexes, the light from the laser is reflected onto the split photo-diode. By measuring the difference signal (A-B), changes in the bending of the cantilever can be measured. Since the cantilever obeys Hooke's law for small displacements, the interaction force between the tip and the sample can be found. The way in which image contrast is obtained can be achieved in many ways. The three main classes of interaction are contact mode, tapping mode and non-contact mode. Contact mode was used for all the experiments where the tip and sample remain in close contact as the scanning proceeds. By "contact" it is meant in the repulsive regime of the inter-molecular force curve.

8.3 Influence of Processing Variables

The creation of a flux of condensable species (neutral atoms and ions), transport of the species from source to substrate, and film growth on the substrate are the major three steps for the formation of a thin film by sputter deposition.

For solar cell applications it is desirable for the TCOs to exhibit both a high electrical conductivity and transparency. These two properties, however, vary oppositely. The key issue is the optimization of the film optical and electrical properties – high optical transparency and low resistivity.

The electrical property and its distribution are considerably affected by sputtering conditions such as substrate-target distance, sputter gas pressure, and the amount of plasma excitation power. Lower resistivity is obtained at the substrate location which corresponds to the center of the target, whereas the resistivity is considerably higher at substrate locations which correspond to the erosion area of the target. The electrical property distribution is plotted as the deviation of resistivity from the minimum resistivity as a function of the substrate location. Usually, the film that has a lower resistivity minimum will have better electrical property distribution. It should be noted that the resistivity in this work is derived from the data on the substrate that corresponds to the center of the target.

The optical gap is defined as the minimum energy needed to excite an electron from the valence band to the conduction band. Figure 8-5 [59] shows a typical ZnO absorption spectra measured by a spectrophotometer. At the short wavelength, the photons have energies greater than the bandgap of the materials and are therefore absorbed. This cutting wavelength can be calculated from $\lambda = 1.24/E_g = 500$ nm. At longer wavelengths (> 1200 nm for ZnO), the photons are reflected because of their interaction with the free carriers in the material due to their very low energy. In the central portion, the photons are transmitted relatively freely and across the visible, and the transmittance is generally about 85%. Since the interest in this work is in measuring the absorption edge shift, the absorption edge is simply deduced from the position of the point of maximum slope in the absorption spectrum. The dependence of the absorption edge is related to the carrier concentration, whereas the shape of the absorption tail can be modified by interference effects and various broadening effects. The optical bandgap is

assumed to be roughly equal to the transmittance edge onset as defined by the intersection of lines constructed from the low transmission UV region and the slope approaching the transmission region. Increased conductivity correlates with higher bandgaps [81]. This movement of the absorption edge to a shorter wavelength region is called the Burstein-Moss shift due to the increase of electron concentration n_e as described in Chapter 6. AZO is a direct bandgap material. Its optical absorption coefficient, α and optical bandgap E_g are related by

$$\alpha = (h\nu - E_g)^{1/2} \qquad (8.2)$$

where hν is the incident photon energy. The absorption coefficient can be calculated from the transmittance I/I_0 by the following:

$$I = I_0 e^{-\alpha t} \qquad (8.3)$$

where I is the intensity of transmitted light, I_0 is the intensity of incident light, and t is the thickness of the AZO film. The linear dependence of α^2 on hν also confirms that AZO films are the direct transition-type semiconductor.

Film stress is another important parameter in film quality. The stress influences not only the mechanical stability of thin film structures (adhesion) but also the electrical properties. This is because the energy stored in a film by stress acts as thermodynamic driving force which tends to relax the stress by defects such as vacancy, dislocation, interstitial. The lattice mismatch will affect the band offsets at heterojunction and thus lead to the change of electronic properties [82]. Usually, low mechanical stress leads to better electrical properties.

Film stress can be introduced into a film due to a volume change in the film when the film is tightly bonded to the substrate. The stress in thin films consists of two

components: the thermal stress and intrinsic stress. The thermal stress arises due to the difference in the thermal expansion coefficients of the film and the substrate when the substrate is at a temperature that is different from its temperature during deposition. It is given by [83]

$$S = (\alpha_f - \alpha_s)(T_s - T_a)E_f \tag{8.4}$$

where α_f and α_s are the average coefficients of thermal expansion for the film and substrate, and E_f is Young's modulus, T_s is the substrate temperature during deposition, and T_a is the temperature during measurement. The value of α for glass is 8×10^{-6}/°C, and 8×10^{-6}/°C for ZnO (c-axis) [84]. Note in this study, all the AZO films are deposited on glass. So, the thermal stress is not important. The intrinsic stress is due to the accumulating effect of the crystallographic flaws that are built into the film during deposition. The intrinsic stress is very sensitive to the deposition conditions. In this work, only the influence of deposition parameters on intrinsic stress is studied. The negative value of stress corresponds to a compressive stress and the positive one to a tensile stress. XRD is employed as an ex-situ method for the stress study. The schematic analysis of deformation system is shown in Figure 8-6. This continuum elastic analysis of stress is based on the assumption that the deformation is uniform in the film throughout the entire thickness of the deposited film. For hexagonal crystals, the linear stress components are given by given by [85]:

$$\begin{Bmatrix} \sigma_x \\ \sigma_y \\ \sigma_z \end{Bmatrix} = \begin{bmatrix} C_{11} & C_{12} & C_{13} \\ C_{12} & C_{11} & C_{13} \\ C_{13} & C_{13} & C_{33} \end{bmatrix} \begin{Bmatrix} \varepsilon_{xx} \\ \varepsilon_{yy} \\ \varepsilon_{zz} \end{Bmatrix} \tag{8.5}$$

where C_{ij} are the elastic stiffness constants and E_{ij} is the linear strain in the ith direction. The stress in the z direction, σ_z, is proved to be zero in films except very close to the edges [86]. Therefore,

$$\varepsilon_{xx} + \varepsilon_{yy} = -C_{33}\varepsilon_{zz}/C_{13} \tag{8.6}$$

The stress in the plane of the film is:

$$\begin{aligned}
\sigma &= \sigma_x + \sigma_y + \sigma_z = \sigma_x + \sigma_y \\
&= (C_{11} + C_{12})(\varepsilon_{xx} + \varepsilon_{yy}) + 2C_{13}\varepsilon_{zz} \\
&= [2C_{13}^2 - C_{33}(C_{11} + C_{12})]/C_{13}\varepsilon_{zz}
\end{aligned} \tag{8.7}$$

where ε_{zz} is the strain normal to the substrate and is given by $(c_0 - c)/c_0$. The lattice constant, c, can be obtained from the X-ray diffraction pattern. c_0 corresponds to the bulk lattice constant which for the case of ZnO is 5.205 Å. The values of the stiffness constants for ZnO are $C_{11} = C_{33} = 2.1 \times 10^{11}$ Pa, $C_{12} = 1.2 \times 10^{11}$ Pa, $C_{13} = 1.05 \times 10^{11}$ Pa, and $C_{12} = 0.42 \times 10^{11}$ Pa [85]. The total stress for ZnO:Al film thus can be calculated from ex-situ XRD measurement by the following equation:

$$\begin{aligned}
\sigma &= \{[2C_{13}^2 - C_{33}(C_{11} + C_{12})]/C_{13}\} \times [(c - c_0)/c_0] \\
&= 4.5 \times 10^{11}(c_0 - c)/c_0 \ \text{Pa}
\end{aligned} \tag{8.8}$$

8.3.1 Effect of Base Pressure

ZnO:Al films were grown at the base pressure in the range 1.7×10^{-7} to 6.7×10^{-7} Torr. The purpose for lowering base pressure is to obtain a cleaner process; lower impurities on the substrate surface and inside the deposition chamber.

i. Effect of Base Pressure on Structural Properties

The deposition rate increases with the decreasing base pressure as shown in Figure 8-7 (a). The sputtering rate is determined by the energy of the ions at the sputtering

target [86]. When the base pressure decreases, the impurities amount will be lower inside the chamber and and thus absorbed on the substrate surface. The energy of sputtered atoms arriving on substrate will on average have more energy due to fewer collisions and lead to higher structural quality and thus higher mobility.

The XRD pattern shown in Figure 8-7 (b) indicates that the film has poor crystallinity at the high base pressure of 6.7×10^{-7} Torr, and film crystallinity increases with decrease of base pressure. This can be explained that the surface migration will be limited due to the existence of more impurity atoms (other than the sputtered ones from target) on the substrate at high base pressure.

ii. Base Pressure Effect on Electrical Properties

There is a dramatically resistivity drop when the base pressure decreases from 6.7×10^{-7} to 2.9×10^{-7} Torr, and a gradual drop from 2.9×10^{-7} to 1.7×10^{-7} Torr by a factor of 0.74 (Figure 8-8 (a)). The decrease of resistivity is due to less scattering of free carrier due to the contamination during the growth when decreasing base pressure according to the conduction mechanism. The resistivity distribution becomes worse when increasing the base pressure as seen in Figure 8-8 (b). The higher concentration of impurities will result in lower mobility of sputtered ion migration on the substrate surface.

iii. Base Pressure Effect on Optical Properties

Figure 8-9 (a) shows that the transmittance decreases with decreasing base pressure presumably due to the lower oxygen and impurity content in the chamber and the increase in electron concentration. Since a decrease in base pressure lowers the resistivity, the bandgap should increase via the Burstein-Moss shift. This conclusion is supported by the apparent shift illustrated in Figure 8-9 (b).

iv. Base Pressure Effect on Spatial Mechanical Properties

The residual stress decreases (i.e., becomes more compressive) as the base pressure decreases (Figure 8-10). This result is consistent with an increase in the crystallinity with a decrease in the base pressure.

iv. Conclusion

The base pressure was varied in the range 1.7×10^{-7} to 6.7×10^{-7} Torr while maintaining the other deposition parameters constant (P_{rf}= 250 W, P_{Ar}= 5 mTorr). Characterizatoin results for the film crystallinity, residual stress, transmittance, and resistivity suggest that a lower base pressure is preferred to obtain films with low resisitivity and good transmittance. It is noted that some additional improvement may be possible by further decreasing the pressure or by changing the other deposition parameters.

8.3.2 Working Gas Pressure Effect

The total pressure of the working gas affects sputter deposition in two opposing ways [87]. The first effect (**Effect I**) is that the greater the working gas pressure, the greater the number of particles in the plasma, and the increased number of particles increases the probability of sputtering from the target at a given r.f. power. On the other hand (**Effect II**) the increased number of particles in the gas will also increase the probability of scattering the sputtered particles during transit from the target to the substrate and will have an adverse effect on the deposition rate beyond a given pressure. The total pressure at a given r.f. power also affects the induced bias on the electrodes which in turn influences the deposition rate.

i. Working Gas Pressure Effect on Structural Properties

As shown in Figure 8-11 (a), there is a sharp increase in deposition rate when the Ar gas pressure is increased from 3 to 5 mTorr. The deposition rate appears to saturate above 5 mTorr even though there is a small increase on deposition rate as the Ar pressure increases is indicated in Figure 8-11 (a). When the Ar pressure is below 5 mTorr, **Effect I** is dominant, and the number of particles in the plasma increases and thus the deposition rate increases. As the pressure continues to increase, **Effect II** also becomes important and these effects balance each other. Thus only a small increase in sputtering rate above 5 mTorr is observed. This observation also indicates that for an Ar pressure lower than 5 mTorr, the collisions between sputtering atoms and the gas are not important. However, "Atomic peening" processes may happen when the pressure is below 5 mTorr.

The broad diffraction peak at 3 mTorr in Figure 8-11 (b) is much broader and has lower intensity than the peaks recorded above 5 mTorr pressure. The poor crystallinity at 3 mTorr pressure occurs because the sputtered atoms have high energy, and high energy O^- will have a negative impact on film quality. This 'atomic peening' mechanism can damage the lattice and result in poor crystallinity. The cystallinity increases when the Ar pressure increases to 5 mTorr, presumably due to a reduction of atomic peening by the increased number of scattering gas particles. However, the crystallinity decreases slightly at 7 mTorr as seen in Figure 8-11 (b). The decrease in crystallinity with the increase of gas pressures above 5 mTorr can be explained by the structure zone model. The structure zone model for metal sputter deposition was proposed by Thornton [88]. According to the structure zone model, at higher pressure, adsorbed Ar can accumulate in crevices and prevent the crevices from filling of the sputtered atoms. The microstructure

of the sputter-deposited film will transfer to the structure consisting of tapered crystallites separated by voids as the working gas pressure increases [88].

ii. Working Gas Pressure Effect on Electrical Properties

As the Ar gas pressure is decreased there is a dramatic resistivity drop in the 3 to 5 mTorr samples followed by a slight drop at 7 mTorr due to reduction of atomic peening as shown in Figure 8-12 (a).

The electrical property distribution is plotted in Figure 8-12 (b), as the deviation of resistivity from the minimum resistivity as a function of substrate location. It should be noted that the resistivity plotted in Figure 8-12 (a) is derived from data on the substrate that corresponds to the center of the target. As we can see from Figure 8-12 (b), increasing the Ar pressure improves the distribution due to the decrease of O⁻ bombardment. Films with a lower resistivity minimum have better electrical property distribution.

iii. Working Gas Effect on Optical Properties

The film deposited at 7 mTorr exhibits a dark gray surface. This decrease in transmittance with the increase in Ar pressure as shown in Figure 8-13 (a) is caused by the entrapped Ar at grain boundaries acting as scattering centers and increasing the carrier concentration. The bandgap shift as a function of working gas pressure is in accordance with the Burstein-Moss shift: Increased conductivity correlates with higher bandgaps. This movement of the absorption edge to a shorter wavelength region, as shown in Figure 8-13 (b), is due to the increase of electron concentration n_e.

iv. Working Gas Effect on Mechanical Properties

The compressive stress is believed to be caused by the atomic peening [89]. In this model, the compressive stress is induced by the bombardment of energetic particles emanating from the target, both sputtered atoms and reflected neutral gas atoms. The impact of these particles is thought to cause some rearrangement of the condensing layers, thereby packing them more tightly in the plane of the film. As the Ar pressure increases, less stress will result in the film as shown in Figure 8-14. This behavior of the stress with pressure is attributed to the bombardment of the film by energetic gas atoms resulting from neutralization and reflection of ions at the target surface. As the pressure increases, the mean free path of these atoms decreases and the atomic peening or negative ion bombardment of the films becomes less important. The intrinsic stress in the film and film structure are also affected by the arrival direction of the sputtered atom flux. At sufficiently high pressure, scattering in the gas randomizes the arrival angle. As mentioned in the structure zone model, at higher pressure, the adsorbed argon can accumulate in crevices and prevent it from filling with the sputtered atoms and thus preventing growth. The film structure will transfer to the structure consisting of tapered crystallites separated by voids as the working gas pressure increases, and thus will decrease the film stress.

The roughness as measured by AFM of the film grown at 3 mTorr is much higher than that grown at either 5 or 7 mTorr due to the atomic peening or negative ion bombardment (Figure 8-15). The roughness increases from 5 to 7 mTorr which can be explained by the structure zone model as previously discussed, and this increase in roughness causes the transmittance to drop in the 7 mTorr film.

v. Conclusions

The Ar pressure can dramatically affect deposition rate, resistivity, and transmittance. Increasing processing gas pressure will reduce the atomic peening or negative ion bombardment effect; however, it will also decrease the transmittance of the film due to trapped Ar atoms. A processing gas pressure in the range 5 to 6 mTorr is the optimum deposition range.

8.3.3 RF Power Effect

When the Ar ion sputters the ZnO:Al target, it will generate negative oxygen ions as confirmed by SIMS [90] and time-of-flight analysis [91, 90] measurements. When the O^- is accelerated in the cathode fall, it may be neutralized and become an energetic oxygen atom. The cathode fall is the region where most of the plasma voltage drops, and it is of order a few cm in front of cathode. It was found by Tominaga *et al.* [92] that the bombardment of the film by energetic O atom or O^- ion is responsible for the high resistivity by decreasing both the carrier mobility and the carrier concentration. The less energetic O atom and O^- ions will also induce an increase in the film resistivity as a result of a decrease in carrier concentration. These atoms and ions will increase the probability of atomic peening. The production of energetic O atom and O^- is higher at higher RF power, and thus their impact on the film properties is more obvious at the higher RF power.

i. RF Power Effect on Structural Properties

In the sputtering process, the species for condensation are created by the positive ions of an inert gas bombarding the target and generating atoms/ions of the target material by momentum transfer. So, the sputtering rate depends on the power input to the target and the plasma density in the vicinity of the target surface. The sputtering rate, R, is proportional to the sputtering yield S by the following relation [86]:

$$R = C \cdot S \cdot I \cdot (1 - \gamma) \tag{8.9}$$

where C is a constant, I is the discharge current and γ is the secondary electron emission coefficient. Therefore, the sputtering rate, R, is determined by the energy of the ions at the sputtering target and plasma density, and is proportional to the discharge power. The number of atoms sputtered from the target is nearly proportional to the RF power. Therefore, the sputtering rate is increased as the RF power increases (Figure 8-16 (a)). This is an advantage for controlling a sputter deposition process. The crystallinity of film deposited below 300 watts (Figure 8-16 (b)) has good crystallinity while film deposited at 500 watts has very bad crystallinity. This indicates that excessive power will be no good for growth due to too high energetic negative ion bombardment on the substrate surface.

ii. RF Power Effect on Electrical Properties

The resistivity increases as the RF power increases with a dramatic increase at 500 W as shown in Figure 8-17 (a). This is because the yield of negative ions is increased especially at the RF power of 500 W. Its bombardment on the surface will limit the migration of sputtered ions on the surface. The increase of deposition rate with RF power will induce more negative ion bombardment and therefore increase the oxygen concentration in the film [93].

The bombardment of O⁻ is also the origin of electrical property spatial variation. The high energetic oxygen bombardment at the substrate location corresponds to the target erosion area. The enhancement of oxidation opposite to the erosion area on substrate results from a nonuniform distribution of oxygen reaching the substrate surface [93]. Samples that show a resistivity local minimum always show better resistivity

distribution. Figure 8-17 (b) shows the resistivity distribution as a function of RF power. The increase of deposition rate with RF power will induce more negative ion bombardment and therefore increase the oxygen concentration in the film [93].

iii. RF Power Effect on Optical Properties

Figure 8-18 (a) shows a decrease of transmittance when decreasing the RF power. This result is largely caused by an increase in the carrier concentration when the RF power decreases since less O is incorporated and thus a lower concentration of O vacancy donors. As can be seen from Figure 8-18 (b), the bandgap shifts to a higher value as the RF power decreases.

iv. RF Power Effect on Mechanical Properties

As the RF power increases, the film stress increases due to the negative ion bombardment as shown in Figure 8-19.

v. Conclusions

It is concluded that for the range of operating parameters studied that higher RF power has a negative impact on film growth due increased high energy negative oxygen ion bombardment. However, lower RF power will cause lower transmittance of the film. Thus, the RF power at 200 to 300 W is the preferred RF power range for the diode sputtering of ZnO:Al.

8.4   Conclusions

Sputter deposition and characterization of ZnO thin films for application as a transparent conducting electrode have been studied. The effects of processing conditions on film properties, evolution of structural and electrical properties, and the influence of ion damage on the thin film properties were investigated.   In all the deposited films, only the (002) peak is observed at 34.2˚. This indicates that the AZO films prepared by RF

diode sputtering in this work have good c-axis orientation. The c-axis orientation in AZO films can be understood by the "grain boundary movement" model proposed by Lodder *et al.* [94]. According to this model, at the very first stage of film growth, certain grains with particular orientation start to grow. By thermodynamic coalescence of crystallites during film growth, orientational growth (c-axis orientation for ZnO film) is achieved. In addition to the c-axis orientation, a small shift of the peak position of the (002) plane is observed with the variation of sputtering condition that is attributed mechanical stress in the film. The mechanical stress observed in this work is compressive stress and no transition from compressive to tensile stress was observed. Film stress is decreased as the working gas pressure increases. This agrees with the results from Maniv *et al.* investigation [85]. Increasing R.F. power, lowering base pressure, and increasing Ar pressure will increase the sputtering rate. However, excessive RF power will be deleterious to the film properties, and too high Ar pressure will result in a dark film, and too low base pressure will cause the change to the target composition. Therefore, a base pressure in the range 2 to 3×10^{-7} Torr, an Ar pressure in the range 5 to 6 mTorr, an RF power in the range 200 to 300 W are the appropriate conditions for the R.F. diode sputtering of ZnO:Al film. The lowest resistivity achieved is 2.7×10^{-3} $\Omega\cdot$cm with a transmittance above 85% and bandgap E_g about 3.35 eV at RF power 250 W, 5 mTorr Ar pressure, and 3×10^{-7} Torr base pressure. ZnO:Al properties with these values are acceptable for application as a transparent conducting electrode. Further decrease in resistivity to the order of 10^{-4} without the decrease of transmittance will need to be done to fabricate higher efficient solar cell. The proposed future work on the sputtered deposition of ZnO:Al will be discussed in detail in Chapter 9. The compressive stress is

believed to be caused by the atomic peening process when the energetic ions and atoms bombard the growing film.
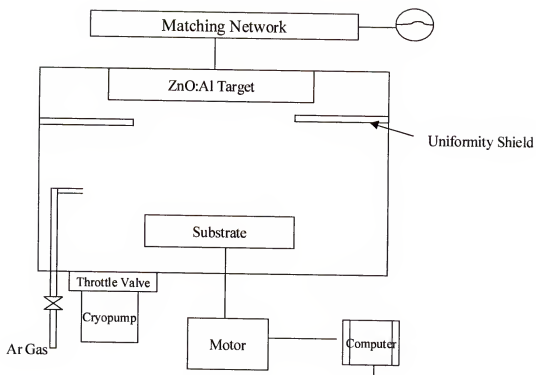
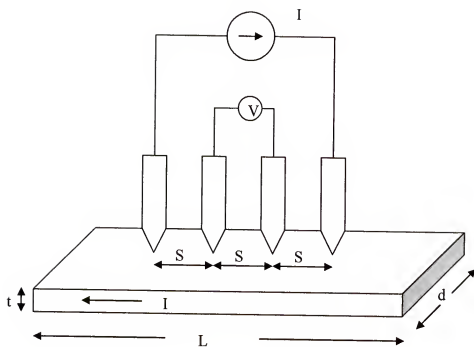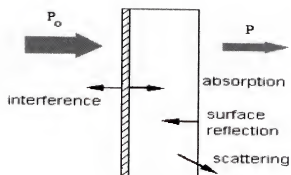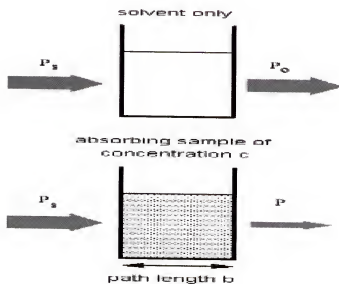Figure 8-1. Schematic diagram of sputter-down target sputtering system.

Figure 8-2. Schematic of four point probe measurement system.

(a)

(b)

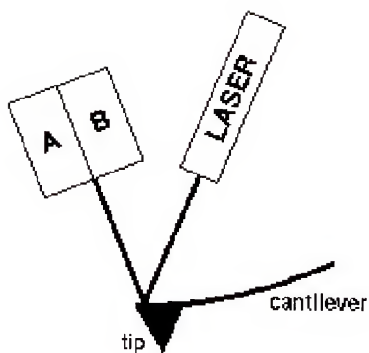Figure 8-3. (a) Spectrophotometer (b)two-step measurement to subtract sample
holder effects.
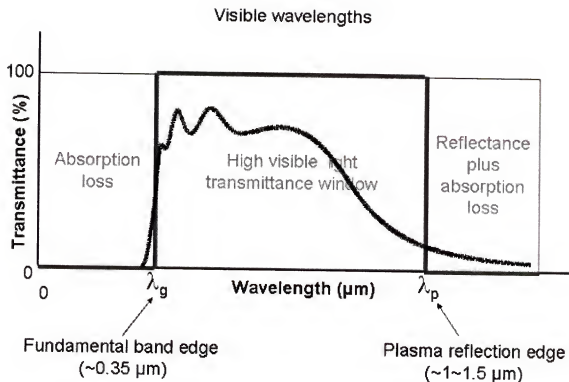
Figure 8-4. Schematic of AFM method [80].

Figure 8-5. Typical transmittance spectra for ZnO [59].
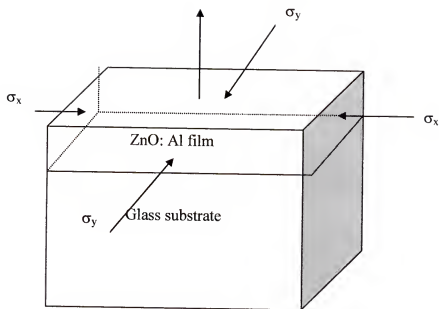
Figure 8-6. Schematic representation of a coherently strained ZnO:Al/Glass film/substrate system. Stresses in the film and the substrate are indicated by σ_x, σ_y, σ_z, respectively.
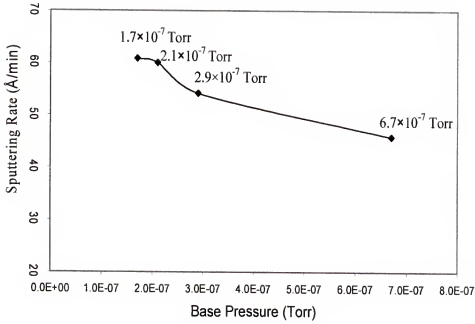
(a)
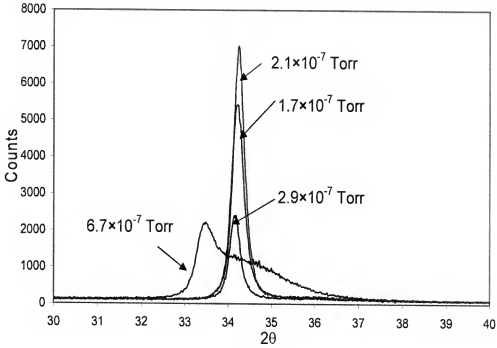
(b)

Figure 8-7. Structural properties of ZnO:Al films as a function of base pressure at P_{rf} = 250 W, P_{Ar} = 5 mTorr. (a) sputtering rate (b) XRD pattern.

P_{rf}: RF power; P_{Ar}: Ar gas pressure; and P_{Base}: Base pressure.

(a)

(b)

Figure 8-8. Electrical properties of ZnO:Al films as a function of base pressure at P_{rf} = 250 W, P_{Ar}= 5 mTorr. (a) resistivity (b) resistivity distribution.
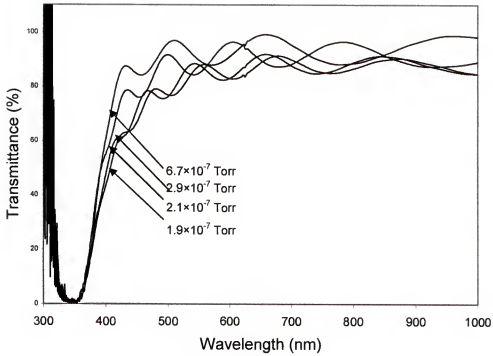
(a)
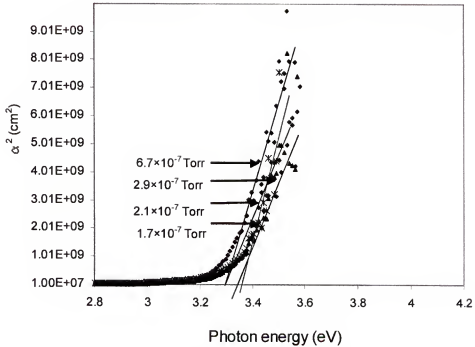
(b)

Figure 8-9.   Optical properties of ZnO:Al films as a function of base pressure at
$P_{rf} = 250$ W, $P_{Ar} = 5$ mTorr (a) transmittance spectrum (b)) α^2-hν plot.
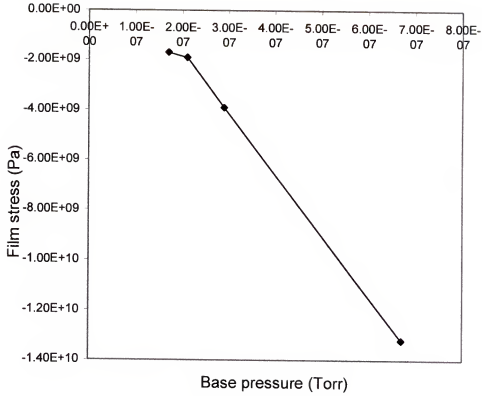
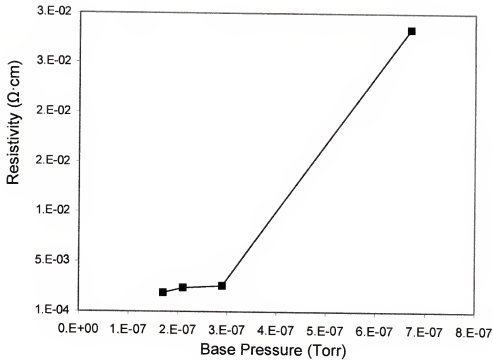Figure 8-10. Film stress of ZnO:Al films as a function of base pressure at $P_{rf} =$ 250 W, $P_{Ar} = 5$ mTorr.
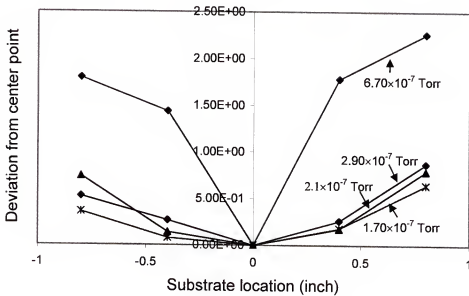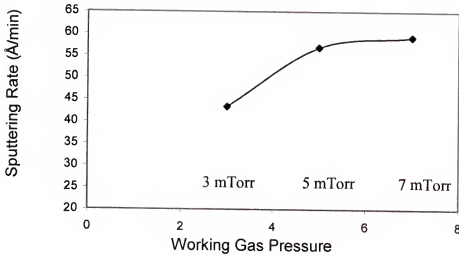
(a)
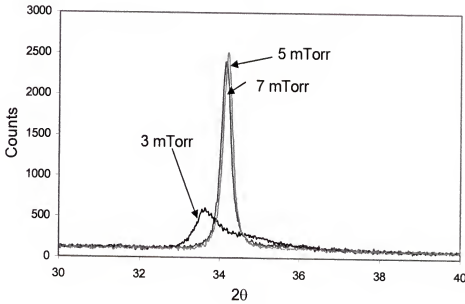
(b)

Figure 8-11. Structural properties of ZnO:Al films as a function of Ar pressure pressure at P_{rf} = 250 W, P_{Base}= 2.9×10⁻⁷ Torr (a) sputtering rate (b) XRD pattern

*P_{rf}: r.f power; P_{Ar}: Working gas pressure; P_B: Base pressure.
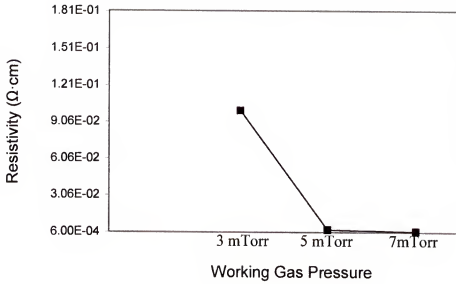
(a)
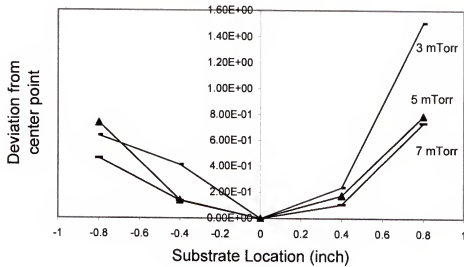
(b)

Figure 8-12. Electrical properties of ZnO:Al films as a function of Ar pressure at $P_{rf} =$ 250 W, $P_{Base} = 2.9 \times 10^{-7}$ Torr (a) resistivity (b) resititivity distribution.

(a)

(b)
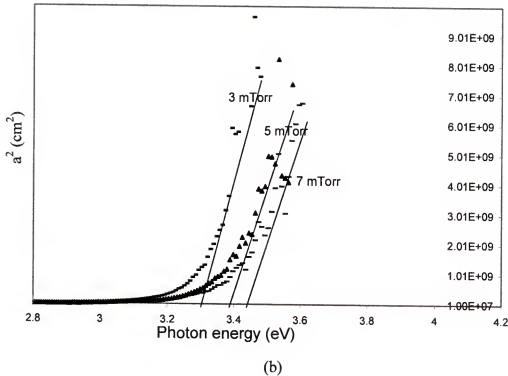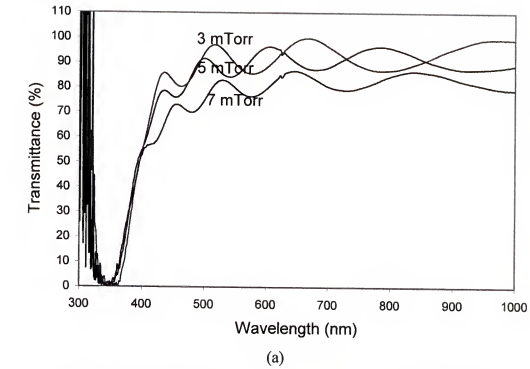
Figure 8-13. Optical properties of of ZnO:Al films as a function of Ar pressure at P_{rf} = 250 W, P_B = 2.9×10^{-7} Torr (a) transmittance spectrum (b) α^2-hv plot.

Figure 8-14.   Film stress of ZnO:Al films as a function of Ar pressure at P_{rf} = 250 W, P_B= 2.9×10^{-7} Torr.
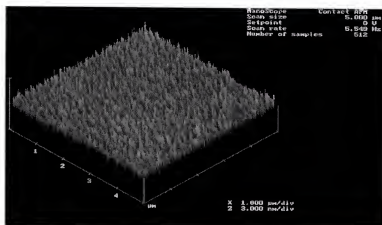
3 mTorr – RMS 8.556 nm
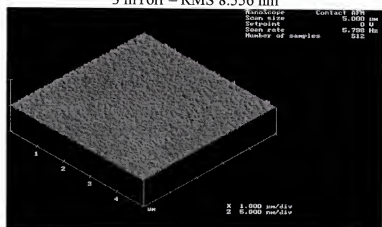
5 mTorr – RMS 4.446 nm
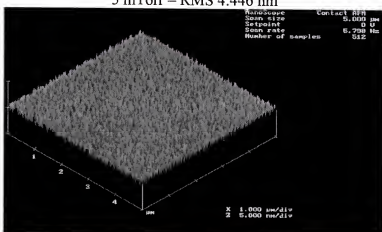
7 mTorr – RMS 5.4957 nm

Figure 8-15. AFM images of the film surface at 3, 5 and 7 mTorr Ar pressure, P_{rf} = 250 W, and P_{Base}= 2.9×10^{-7} Torr.
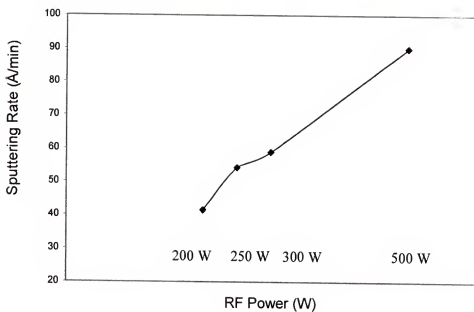
(a)
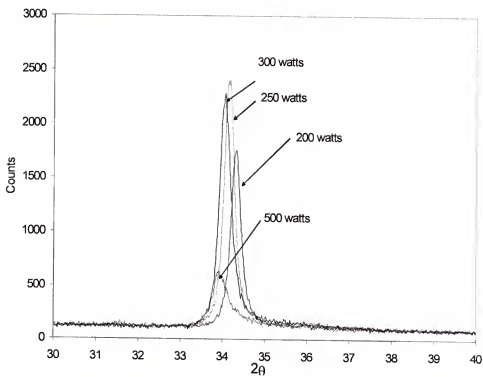
(b)

Figure 8-16. Structural properties of ZnO:Al films as a function of RF power at $P_{Ar} = 5$ mTorr, $P_{Base} = 2.9 \times 10^{-7}$ Torr (a) sputtering rate (b) XRD pattern.

(a)

(b)
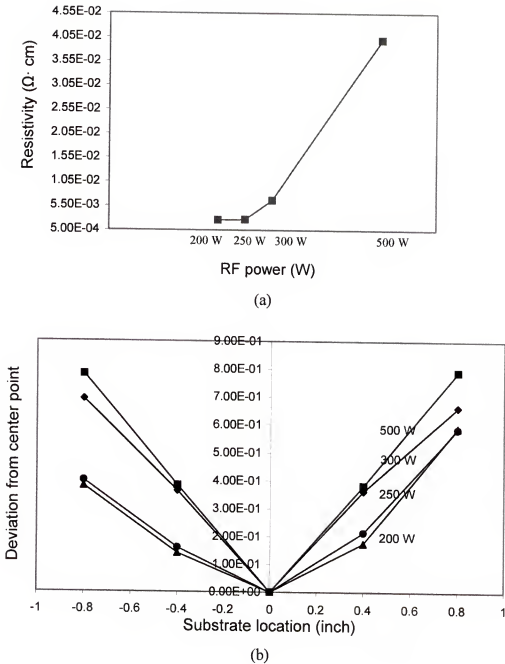
Figure 8-17. Electrical properties of ZnO:Al films as a function of RF power at $P_{Ar} =$ 5 mTorr, $P_{Base} =$ 2.9×10⁻⁷ Torr (a) resistivity (b) resistivity distribution.
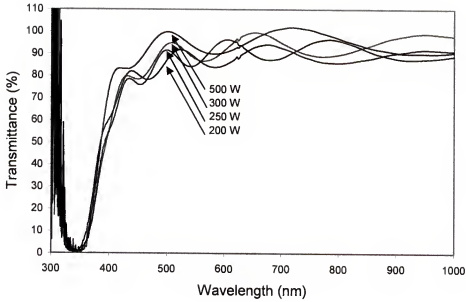
(a)
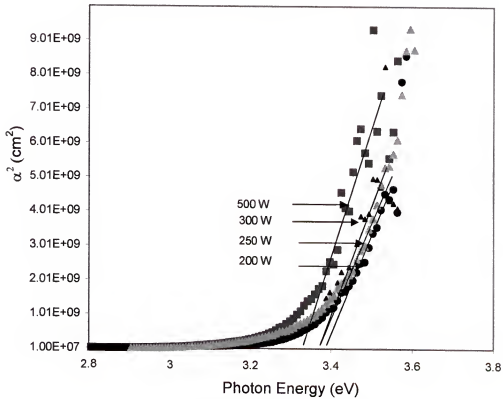
(b)

Figure 8-18. Optical properties of of ZnO:Al films as a function of RF power at P_{Ar} = 5 mTorr, P_{Base} = 2.9×10⁻⁷ Torr. (a) transmittance spectrum (b) α^2-hν.

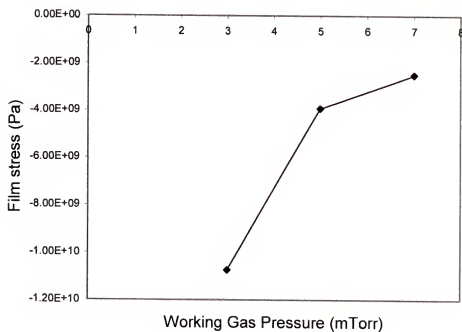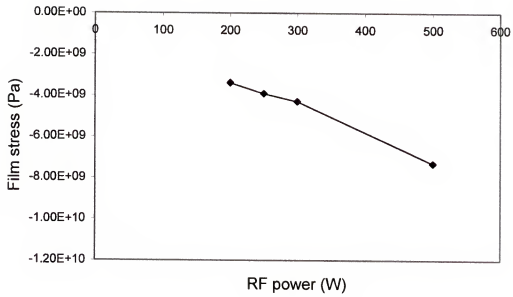Figure 8-19. Film stress of ZnO:Al films as a function of RF power at $P_{Ar} = 5$ mTorr, $P_{Base} = 2.9 \times 10^{-7}$ Torr.

CHAPTER 9
CONCLUSIONS AND FUTURE DIRECTIONS

9.1 Absorber

9.1.1 Conclusions

In this research, the existence of a low temperature $L+\alpha$-CuInSe$_2$ two phase field was successfully predicted by thermodynamic modeling of the Cu-In-Se composition isothermal diagram at 773 K using the CALPHAD approach. In this approach, the gas phase is modeled as an ideal mixture of all the gaseous species; the composition-dependence of the Gibbs energy of non-stoichiometric compounds are described by a sublattice model; and the liquid phase is described by the ionic model. The CuInSe$_2$ phase is modeled by a defect model that incorporates neutral and ionized defects as well as electron-holes into the sublattice model. A reasonable agreement for the α-CIS phase was obtained between the model-calculated values and the phase equilibrium available in the literature.

An alternative low temperature route to CuInSe$_2$ formation was demonstrated using RTP on the stacked precursor structure Cu-Se/In-Se/Mo/glass based on the suggestion by the phase diagram. The influence of various ambient compositions on phase transformations after rapid thermal processing was determined. A short time annealing of 60 s at 480 ˚C in a Se ambient generated by volatilization of a thin Se layer on the sample cover, followed by a second anneal using a clear cover, was able to produce a single-phase α-CuInSe$_2$ with relatively large grain boundary size. High melting temperature

secondary phase, $Cu_{2-x}Se(s)$ does not react with InSe without Se overpressure. Based on these results, a 5.08% device with $V_{oc} = 0.296$ V, $J_{sc} = 34.65$ mA/cm^2 and fill factor = 49.54% is achieved by using the absorber that is obtained by RTP on the CuSe/InSe/Mo/Glass precursor under Se control in a PVD system. It is worth noting that this 5.08% cell is achieved without full optimization of the process. Therefore, the RTP on binary bilayer process is very promising.

A preliminary study of samples with the In-Se binary layer on the top of the Cu-Se layer (precursor structure InSe/CuSe/Mo/glass) was undertaken. Adding a thin seed layer of InSe to the film to give the precursor structure InSe(1 µm)/ CuSe(1 µm)/ InSe(500 Å)/ Mo/ Glass showed improved surface morphology.

The performance of photovoltaic devices is significantly affected by the presence of native defects. Deep-level transient spectroscopy (DLTS) is used in this work to address the current lack of fundamental understanding of absorber-defect properties, yielding relevant information about defect types, their capture cross-sections, and energy levels and densities. Three solar cells developed using different absorber growth technologies were analyzed using DLTS, capacitance-voltage, and capacitance-temperature techniques. It was found that the 5.08% cell produced at the University of Florida exhibits a middle-gap defect that may explain the cell's low fill factor and open-circuit voltage values observed. A highly efficient cell produced by the National Renewable Energy Laboratory was found to contain three minority carrier traps; however, high cell performance is nevertheless retained because these traps act as ineffective recombination centers. The approach followed using the DLTS technique serves as a paradigm for revealing the presence of significant defect levels in absorber

materials, and may be used to support the identification of remedial processing operations.

9.1.2 Future Work

Further work needs to be done on the thermodynamic modeling of the Cu-In-Se system to get better agreement of phase equilibrium for all the phases such as β_R-CIS (Cu1In$_3$Se$_5$), γ-CIS (Cu1In$_5$Se$_8$), and β_H –CIS (Cu$_2$In$_4$Se$_7$). It is important to understand mechanisms present in the formation of absorber layer on the interface of binary compound couple. The impacts of the process parameters (such as ramp rate, soak time and temperature), the modification of precursor composition (such as how much Se excess) and the design of precursor configuration are the key issues to optimize the process. This process occurs very fast. CIS is formed at the interface of the two binary compound phases (CuSe and InSe) first, and the reaction is continued by the species going through each interface such as the interfaces CuSe/CIS and CIS/InSe. Therefore, the behavior of diffusion plays an important role in this process. The simulation of the whole process and the prediction of the phase and concentration profile under various process conditions can be conducted by using the software DICTRA, a multicomponent diffusion code with the assessed, thermodynamic and kinetic descriptions. To perform simulations using DICTRA, both thermodynamic and kinetic descriptions are needed. The diffusion coefficients, which are used in the simulations, can then be obtained as a product of a thermodynamic and a kinetic factor. The thermodynamic factor is essentially the second derivatives of the molar Gibbs energy with respect to the concentrations, and is known if the system has been assessed thermodynamically. The kinetic factor contains the atomic mobilities, which are stored in the kinetic database. The

analysis and simulation can provide insight into optimizing the processing conditions and compositions to avoid the formation of other phases at the interfaces.

The middle gap Cu_{In} is identified in the absorber film produced by the rapid thermal processing on the precursor with structure CuSe/InSe/Mo/Glass. To further improve the cell performance, this defect concentration must be reduced. One method is intentionally doping the film with sodium. The doped sodium will enter the indium site and substitute copper to form Na_{In} defects and therefore reduce the grain boundary energy barrier and remove the midgap states. Another method is incorporating gallium into the precursor and obtaining the final film with $CuIn_{1-x}Ga_xSe_2$ composition. The Ga will segregate at the back surface of the absorber and create the band grading.

For RTP study on the reversed precursor structure on the InSe/CuSe/InSe (seed)/Mo, the structure and process conditions need to be optimized to produce the device quality film.

9.2 Transparent Conducting Oxides

9.2.1 Conclusions

In this work, a model is developed to estimate the equilibrium fluorine solubility in fluorine-doped tin oxide (FTO) as a function of temperature and of the partial pressure of dopant precursor. The modeling results with $CBrF_3$ precursor show that the F concentration increases with the temperature and eventually, it reaches the solubility limit. The calculated and experimental trends are similar, that is, both the F and carrier concentrations increase rapidly as the $CBrF_3$ amount increases. The F concentration is much larger than the carrier concentration. The hypothesis to explain this is that the F is not totally ionized. The effect of different dopant precursors (CF_4, $CBrF_3$, and ClF_3) on F incorporation has been estimated and compared with experimental results. It was found

that $CBrF_3$ is a reactive precursor although not as reactive as CIF_3. The reactivity of CF_4 is much lower than the other two precursors. This is consistent with experimental observation. The F doping solubility was also compared in the commonly used SnO_2, CdO, ZnO and In_2O_3 transparent conductive oxides by using Delta Lattice Parameter model. The results indicate that the F solubility follows the trend SnO_2 $>ZnO>CdO>In_2O_3$.

The research presented in this thesis also investigated the relationships between the properties of ZnO:Al thin films and the RF diode sputter deposition process used to deposit them. This investigation was performed by depositing ZnO:Al followed by characterization of their structural, electrical, and optical properties. It was found that the negative ion bombardment and atomic peening play very important roles in film growth and their properties. In all the deposited films, only the (002) peak is observed at 34.2˚. This indicates that the AZO films prepared by RF diode sputtering have good c-axis orientation. In addition to the c-axis orientation, a small shift of the peak position of the (002) plane is observed with the variation of sputtering condition which introduces mechanical stress into the film. The mechanical stress observed in this work is compressive and no transition from compressive to tensile stress evident. The film stress decreased as the working gas pressure increases. Increasing R.F. power, lowering base pressure, and increasing Ar pressure increased the sputtering rate. However, excessive RF power was deleterious to the film properties, and too high an Ar pressure resulted in a dark film, and too low of a base pressure caused a composition change in the target. Therefore, a base pressure in the range 2 to 3×10^{-7} Torr, an Ar pressure in the range 5 to 6 mTorr, an RF power in the range 200 to 300 W are the appropriate conditions for the R.F.

diode sputtering of ZnO:Al film. The lowest resistivity achieved was 2.7×10^{-3} $\Omega \cdot$cm with a transmittance above 85% and bandgap Eg about 3.35 eV at RF power 250 W, 5 mTorr Ar pressure and 3×10^{-7} Torr base pressure. The compressive stress is believed to be caused by the atomic peening process when the energetic ions and atoms bombard the growing film or by the acceleration of negative ion in the cathode fall.

9.2.2 Future Work

There is a growing need to understand TCO materials. It is essential to find either superior materials (intrinsic) or better ways of making existing materials (extrinsic). The emphasis must be on increased carrier mobility. New approaches are needed for low-temperature deposition (process compatibility, plastic substrates) An investigation has been conducted on the phase-field defined by the three binary oxides, ZnO, CdO, and SnO_2 using chemical vapor deposition. However, little progress has been made. The exploration of novel p-type material TCOs will expand the application of the TCO material. Compounds such as ZnO:N, $CuInO_2$ and $SrCu_2O_2$, will be the very interesting candidate materials for p-type TCOs. Future work is anticipated to include the development of both n and p-type TCO materials with the aim to increase the carrier mobility.

The thermodynamic modeling exploring on the compositional phase space using the CALPHAD approach will provide insightful fundamental understanding of the material to optimize n-TCOs created from combinations of well known single-metal n-TCOs. The CALPHAD (Computer Coupling of Phase Diagrams and Thermochemistry) aims to promote computational thermodynamics through the development of models to represent thermodynamic properties for various phases.

Adding a magnetron source can dramatically improve the sputtering process of ZnO:Al. The magnetic field confines electrons in front of the target. The electrons are significantly influenced by magnetic field while the ions are not. The electrons perform cycloidal orbits in the crossed electric and magnetic field, leading to high ionization efficiency and therefore increaseing the sputtering rate. Higher sputtering rate will limit the exposure time of the growing film to the vacuum ambient and therefore decreasing the incorporation of gas phase contamination and ion damage. Future work should investigate the use of RF magnetron sputter deposition and characterization of ZnO thin films for application as a transparent conducting electrode. Installation of Residue Gas Analyzer (RGA) would be a very helpful technique in optimization of the process.

LIST OF REFERENCES

[1]   M. A. Contreras, H. Wiesner, D. Niles, K. Ramanathan, R. Maston, J. Tuttle, J. Keane, and R. Noufi, *the 25th IEEE Photovoltaic Specialist Conference*, Washington, D.C. 1996.

[2]   A. L. Fahrenbruch, and R. H. Bube, *Fundamentals of Solar Cells,* Academic Press, New York-London, 1983.

[3]   C-H Huang, *Alternative buffer layers, device modeling and characterization of copper-indium-diselenide-based thin-film solar cells*, Ph.D. dissertation, University of Florida, 2003.

[4]   R.D. Wieting, *the 29th IEEE Photovoltaic Specialist Conference*, 2002.

[5]   D.X. Liao, A. Rockett, *Applied Physics Letters,* Vol. 82, No. 17, pp. 2829-2831, 2003.

[6]   S-H Wei, S.B. Zhang and A. Zunger, *Journal of Applied Physics,* Vol. 85, pp. 7214-7218 ,1999.

[7]   F. Hasson and R. Noufi, National Renewable Energy Lab, private communication.

[8]   A. M. Gabor, J. R. Tuttle, M. H. Bode, A. Franz, A. L. Tennant, M. A. Contreras, R. Noufi, D.G. Jensen, and A. M. Hermann, *Solar Energy Materials and Solar Cells*, No. 41-42, Vol. 247-260, 1996.

[9]   D.S.Albin, Y.Yan and M.M.Al-Jassim, *Progress in Photovoltaics: Research and Application,* pp. 426-436. 2002,

[10]   J.L. Gray, R. J. Schwartz and Y-J. Lee, *the 13th NREL Photovoltaics Program Review Meeting*, Lakewood, Colorado, 1995.

[11]   I. M. Dharmadasa, A. P. Samantilleke, N.B. Chaure and J. Young, *Semiconductor Science and Technology*, Vol. 17, pp 1238-1248, 2002.

[12]   Available at http://www.appliefilms.com/Precision2/11_photovoltaic/Photovoltaic_02htm

[13]   H. W. Schock and R. Noufi, *Progress in Photovoltaics: Research and Application,* Vol. 8, pp. 151-160, 2000.

[14] J.U. Ruhle and R.D. Wieting, *28th IEEE Photovoltaic Specialist Conference*, 2000.

[15] A. Catalano, *Solar Energy Materials and Solar Cells*, No. 41-42, Vol. 205-217, 1996.

[16] B. M. Keyes, P. Dippo, W. Metzger, J. AbuShama, and R. Noufi, *the 29th IEEE Photovoltaic Specialist Conference,* New Orleans, LA, 2002.

[17] S.S. Li, *Semiconductor Physical Electronics*, Plenum Press, New York and London, 1993.

[18] G. Zahan, and P. Paufler, *Crystal Research and Technology*, Vol. 23, No. 4, pp.499-507, 1988.

[19] C.J. Kiely, R.C. Pound, G. Kenshole, and A. Rockett , *Philosophical Magazine A*, Vol. 63, No. 6 pp. 1249-1273, 1991.

[20] G. Dagan, T. F. Ciszek, and D. Cahen, *J. Phys. Chem.* Vol. 96, pp. 11009, 1992.

[21] V. Nadazdy, M. Yakushev, E. H. Djebbar, A. E. Hill, and R. D. Tomlinson, *Journal of Applied Physics*, Vol. 84, No. 8, 1998.

[22] S. Niki, H. Shibata, S. Ishibashi, T. Ohdaira, P. J. Fons, A. Yamada, H. Oyanagi, N. Sakai, H. Yokokawa, *Proceedings of the Second World Conference and Exhibition on Photovoltaic Solar Energy Conversion*, Wien, Austria, 6-10 July, 1998, in press

[23] R. Suzuki, T. Ohdaira, S. Ishibashi, A. Uedono, S. Niki, P.J. Fons, A. Yamada, T. Mikado, T. Yamazaki, S. Tanigawa, *Inst. Phys. Conf. Ser.* No. 152, pp. 757, 1998.

[24] A. Polity, R. Krause-Rehberg, and T. E. M. Staab, M. J. Puska, J. Klais, H.J. Moller, and B. K. Meyer, *Journal of Applied Physics,* Vol. 83, No. 1 pp. 71-78, 1998.

[25] J. Klais, H. J. Moller, R. K. Rehberg, D. Cahen and V. Lyakhovitskay, *Ternary and Multinary Compounds-Institute of Physics Conference Series,* Vol. 152, pp. 741-744, 2000.

[26] G. A. Medvekin and M. A. Magomedov, *Journal of Applied Physics,* Vol. 82, No. 8, pp. 4013-4019, 1997.

[27] D.J. Schroeder, J.L. Hernandez, G.D. Berry and A.A. Rockett, *Journal of Applied Physics,* Vol. 83, No.3, pp.1519-1526, 1998.

[28] S. B. Stanbery, *Heteroepitaxy and nucleation control for the growth of metal chaclogenide using activated reactant sources*, Ph.D. Dissertation, University of Florida, 2001.

[29]   J. Giber, F. Beleznay, I.C.Szĕp, and J. László, *Proceedings of the international School held in Hungary*, September, 1982.

[30]   B. Henderson, and A.E. Hughes, *Defects and Their Structure in Nonmetallic Solids*, Plenum Press, New York and London, 1975.

[31]   S. B. Zhang, Su-Huai Wei, and Alex Zunger, *Physical Review B*, Vol. 57, No. 16 pp9642 –9656, 1998.

[32]   S. B. Zhang, Su-Huai Wei, and Alex Zunger, *Physical Review Letters*, Vol. 78, No. 21 pp4059 – 4062, 1997.

[33]   J.H. Schon and E. Bucher, *Solar Energy Materials & Solar Cells*, Vol. 57, pp. 229-237, 1999.

[34]   A. Zunger, S.B. Zhang and S.H. Wei, *26th IEEE Photovoltaic Specialist Conference, Andheim, CA*, pp. 313-318, 1997.

[35]   S.B. Zhang, S.H. Wei and A. Zunger, *Phys. Rev. B*, Vol. 57, pp.9642-9651, 1998.

[36]   Neumann and R.D. Tomlinson, *Solar Cells*, Vol. 28, pp.301-307, 1990

[37]   G. Kühn, W. Möller and W. Engel, *Thermochimica Acta*, Vol. 78, No. 1-3, pp. 129-134, 1984.

[38]   T. Gödecke, T. Haalboom, and F. Ernst , *Zeitschrift für Metallkunde*, Vol. 91, No. 8 pp.622-662, 2000.

[39]   M. Ider, *Thermochemistry and Phase Diagram Studies in The Cu-In-Ga-Se System*, Ph.D. dissertation, University of Florida, 2002.

[40]   I. Dirnstorfer, D.M. Hofmann, D. Meister, B.K. Meyer, *Journal of Applied Physics*, Vol. 85, No.3, pp. 1423-1428, 1999.

[41]   K. Yoshino. H. Yokoyama,K. Maeda, T. Ikari, A. Fukuyama, P.J. Fons, A. Yamada, S. Niki, *Journal of Applied Physics*, Vol. 86, No.8, pp.4354-4359, 1996.

[42]   G. Masse and E. Redjai, *Journal of Applied Physics*, Vol. 56, No.4, pp. 1154-1159, 1984.

[43]   B.J. Stanbery, C.-H. Chang, S. Kim, S. Kincal, G. Lippold, S.P. Ahrenkiel, L. L. Kerr, T.J. Anderson, M.M. Al-Jassim, *Self Organized Processes in Semiconductor Alloys*, MRS Symposium Proceedings, Vol. 583, 195-200, 2000.

[44]   C-H Chang, *Processing and Characterization of Copper Indium Selenide for Photovoltaic Applications*, Ph.D. Dissertation, University of Florida, 2000.

[45] R. Friedfeld, R.P. Raffaelle, and J.G. Mantovani, *Solar Energy Materials and Solar Cells*, Vol. 58, pp. 375-385, 1999.

[46] I. Forbes, F.O. Adurodija and M.J. Carter, *Proceedings of the 6th International PVSEC, New Delhi*, pp.1965-1968, 1996.

[47] N. Orbey, H. Hichri, R.W. Birkmire and TWF Russell, *25th IEEE Photovoltaic Specialist Conference*, May 13-17, Washington, D.C. pp. 981-982, 1996.

[48] D.V. Liang, *J. Appl. Phys*, Vol. 45, pp.3014, 1974.

[49] T. Minemoto, *Solar Energy Materials & Solar Cells*, Vol. 67, pp. 83-88, 2001.

[50] P.R. Subramanian and D.E. Laughlin. *Bulletin of Alloy Phase Diagrams* 10, p. 554, 1989

[51] Q. Chen, M. Hillert, B. Sundman, W.A. Oates, S. G. Fries, and R. Schmid-Fetzer, *Journal of Electronic Materials*, Vol. 27, No. 3 pp.961-971, 1998.

[52] T. J. Anderson, *CALPHAD*, Vol. 21, No. 2, pp. 266-282, 1997.

[53] John B. Mooney and Robert H. Lamoreaux, *Solar Cells*, Vol. 16. pp. 211-220, 1986.

[54] O. Madelung, *Numerical Data and Functional Relationships in Science and Technology Semiconductors: Physics of III-V Compounds*, Berlin, New York : Springer-Verlag, 1991.

[55] W. Zhuang, C-H Chang, J. Sheng, and T.J. Anderson, *CALPHAD*, 2002.

[56] J.C. Mikkelsen, *Journal of Electronic Materials*, Vol. 10, pp. 541, 1981.

[57] J.R. Tuttle, J.R. Sites, A. Delahoy, W. Shafarman, B. Basol, S. Fonash, J. Gray, R. Menner, J. Phillips, A. Rockett, J. Scofield, F.R. Shapiro, P. Singh, V. Suntharalingam, D. Tarrant, T. Walter, S. Wiedeman, and T. M. Peterson, *Progress in Photovoltaics Research and Application,* Vol. 3, pp.89-104, 1995.

[58] S.S. Hegedus, S. Albright, F. Jeffrey, T.J. McMahon, and S. Wiedeman, *Thin Film Photovoltaic Symposium Workshop Report*, 2000.

[59] T. J. Coutts, *Transparent Conductive Oxides and its Application*, AVS short course notes, Denver, CO, 2002.

[60] T. J. Coutts, T. O. Mason, J. D. Perkins, and D.S. Ginley, *Electrochemical Society Proceedings*, Vol. 99-11, pp. 274-288.

[61] T. Minami, Review Paper , *MRS Bulletin*, pp. 38-44, 2000.

[62] R.G. Gordon, *MRS Bulletin*, pp. 52-57, 2000.

[63]   D. A. Glocker, S. Ismat Shah, *Handbook of Thin Film Process Technology*, Bristol, UK ; Philadelphia : Institute of Physics Pub., 1995.

[64]   N. Saunders and A.P. Miodownir, *CALPHAD – Calculation of Phase Diagram*, Oxford, New York, Pergamon, 1998.

[65]   N. Dupin, and I Ansara, available at http://www.inpg.fr/ltpcm/base/zircobase, unpublished, 2003.

[66]   G.B. Stringfellow, *Orgnaometallic Vapor-Phase Epitaxy*, Academic Press Inc. 1989.

[67]   J.A. Van Vechten, *Physical Review*, Vol. 187, No.3, pp.1007-1020, 1969.

[68]   P.Villars and L.D. Calvert, Pearson's Handbook of Crystallographic Data for Intermetallic Phases, Metals Park, OH, American Society for Metals, 1985.

[69]   *Handbook of the Physicochemical Properties of the Elements*, Plenum: New York, 1968.

[70]   *JANAF Thermochemical Tables*, Washington, D.C.: American Chemical Society, New York: American Institute of Physics for the National Bureau of Standards, 1986.

[71]   G. Baret, R. Madar, and C. Bernard, *Journal of Electrochemical Society,* Vol. 138, No. 9 pp. 2831-2835, 1991.

[72]   C.G. Borman, and R. Gordon, *Journal of Electrochemical Society,*, Vol. 136, No. 12 pp. 3820-3828, 1989.

[73]   K. Li, E. M. Kennedy, and B.Z. Dlugogorski, *Chemical Engineering Science*, Vol. 55, pp 4067-4078, 2000.

[74]   R. Gordon, *United States Patent* 4146657 Mar 27, 1979.

[75]   J. Hu and R. Gordon, *American Institute of Physics*, pp. 381-387, 1992.

[76]   X. Li, T. Barnes, C. DeHart, D. King, S. Asher, M. Young, T.A. Gessert, and T.J. Coutts, *Mat. Res. Soc. Symp. Proc.* Vol. 666, pp. F3.18.1-F3.18.6, 2001.

[77]   A. Sanchez-Juarez, A. Tiburcio-Silver, and A. Ortiz, *Solar Energy Materials and Solar Cells*, Vol 52, pp. 301-311, 1998.

[78]   L.W. Reith, *Sputter Deposition of ZnO Thin Films*, Ph.D. dissertation, 2001.

[79]   Manual of Perkin-Elmer 4100 Sputtering System

[80]   Manual of Digital Instruments Nanoscope III SPM
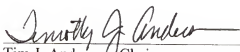
[81]   E. Burstein, *Physical Review.* Vol 93, pp 632-633, 195.

[82]   D.M. Mattox, *J. Vac. Sci. Technol. A*, Vol. 7, No. 3, pp. 1105-1114, 1989.

[83]   L. Eckertová, *Vacuum,* Vol. 36, pp. 561- 569, 1986.

[84]   *CRC handbook of chemistry and physics*, Cleveland, Ohio, CRC Press, 1995-1996.

[85]   S. Maniv, W.D. Westwood, and E. Colombini, *J. Vac. Sci. Technol.* Vol 20, No 2. pp 162-170, 1982.

[86]   Klaus Ellmer, *J. Phys. D: Appl Phys.* Vol. 33, pp R17-32, 2000.

[87]   S. A. Bashar, *Study of Indium Tin Oxide (ITO) for Novel Optoelectronic Devices*, Ph.D. Dissertation, University of London, 1998.

[88]   H.A. Thornton, *J. of Vac. Sci. Technol.* Vol. 11 No. 4, 1974.

[89]   F. M. D'Heurle, and J. M. E. Harper, *Thin Solid Films*, Vol.171, No.1, pp.81-92, 1989.

[90]   J.J. Cuomo, R. J. Gambino, J. M. E. Harper, and J.D. Kuptsis, *J. Vac. Sci. Technol.* Vol 15, No.2 pp. 281-287, 1978.

[91]   Manual for AG Heatpulse 4300 Rapid Thermal Processing system.

[92]   K. Tominaga, T. Yuasa, M. Kume, and O. Tada, *Japaness Journal of Applied Physics, Part I* Vol. 24 pp944-949, 1985.

[93]   R. Cebulla, R. Wendt, and K. Ellmer, *Journal of Applied Physics,* Vol. 83, No. 2, pp. 1087-1095, 1998.

[94]   J.C. Lodder, T. Wielinga, J. Worst, *Thin Solid Films*, Vol. 101 pp. 61. 1983.

[95]   J. Clark, available at http://four-point-probes.com/correct.html.

BIOGRAPHICAL SKETCH

The author, Lei Li Kerr, was born in Linchuan, Jiangxi province, China, in 1975. She graduated from the First High School in Linchuan in 1993. Under the influence of her father, who is a researcher in mechanical engineering in a large automobile manufacturing company in China, she went to the Wuhan Institute of Chemical Technology in 1993 and graduated with a B.S. in chemical engineering in 1997. In August 1998, she came to the United States to begin her Ph.D. program under the supervision of Dr. Tim J. Anderson in the Department of Chemical Engineering at the University of Florida.

I certify that I have read this study and that in my opinion it conforms to acceptable standards of scholarly presentation and is fully adequate, in scope and quality, as a dissertation for the degree of Doctor of Philosophy.

Tim J. Anderson, Chairman
Professor of Chemical Engineering

I certify that I have read this study and that in my opinion it conforms to acceptable standards of scholarly presentation and is fully adequate, in scope and quality, as a dissertation for the degree of Doctor of Philosophy.

Oscar D. Crisalle
Associate Professor of Chemical
    Engineering

I certify that I have read this study and that in my opinion it conforms to acceptable standards of scholarly presentation and is fully adequate, in scope and quality, as a dissertation for the degree of Doctor of Philosophy.

Fan Ren
Professor of Chemical Engineering

I certify that I have read this study and that in my opinion it conforms to acceptable standards of scholarly presentation and is fully adequate, in scope and quality, as a dissertation for the degree of Doctor of Philosophy.

Sheng S. Li
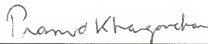Professor of Electrical and Computer
    Engineering

I certify that I have read this study and that in my opinion it conforms to acceptable standards of scholarly presentation and is fully adequate, in scope and quality, as a dissertation for the degree of Doctor of Philosophy.

Paul H. Holloway
Professor of Materials Science and
    Engineering

This dissertation was submitted to the Graduate Faculty of the College of Engineering and to the Graduate School and was accepted as partial fulfillment of the requirements for the degree of Doctor of Philosophy.

May, 2004

Pramod P. Khargonekar
Dean, College of Engineering

Winfred M. Phillips
Dean, Graduate School